

UC Berkeley

UC Berkeley Electronic Theses and Dissertations

Title

Investigating the Anisotropic Scintillation Response in Organic Crystal Scintillator Detectors

Permalink

<https://escholarship.org/uc/item/81z4t4xs>

Author

Schuster, Patricia Frances

Publication Date

2016

Peer reviewed|Thesis/dissertation

**Investigating the Anisotropic Scintillation Response in Organic Crystal
Scintillator Detectors**

by

Patricia Frances Schuster

A dissertation submitted in partial satisfaction of the

requirements for the degree of

Doctor of Philosophy

in

Engineering - Nuclear Engineering

in the

Graduate Division

of the

University of California, Berkeley

Committee in charge:

Professor Karl van Bibber, Chair
Professor Kai Vetter
Associate Professor Naomi Ginsberg
Dr. Erik Brubaker

Summer 2016

**Investigating the Anisotropic Scintillation Response in Organic Crystal
Scintillator Detectors**

Copyright 2016
by
Patricia Frances Schuster

Abstract

Investigating the Anisotropic Scintillation Response in Organic Crystal Scintillator Detectors

by

Patricia Frances Schuster

Doctor of Philosophy in Engineering - Nuclear Engineering

University of California, Berkeley

Professor Karl van Bibber, Chair

Organic scintillator materials have long been used as radiation detectors. They offer simultaneous detection of fast neutrons and gamma rays for applications in nuclear nonproliferation, international safeguards, and national security. The recent development of high quality stilbene crystals with excellent neutron-gamma pulse shape discrimination (PSD) has generated renewed interest in using crystalline materials. However, crystal organic scintillators are subject to a directional dependence in their response to heavy charged particle interactions, degrading their energy resolution for neutron measurements and worsening their PSD performance.

This dissertation presents several studies that experimentally characterize the scintillation anisotropy in organic crystal scintillators. These include measurements of neutron, gamma-ray and cosmic muon interactions in anthracene, a historical benchmark among organic scintillator materials, to confirm and extend measurements previously available in the literature. The gamma-ray and muon measurements provide new experimental confirmation that no scintillation anisotropy is present in their interactions. Observations from these measurements have updated the hypothesis for the physical mechanism that is responsible for the scintillation anisotropy concluding that a relatively high dE/dx is required in order to produce a scintillation anisotropy.

The directional dependence of the scintillation output in liquid and plastic materials was measured to experimentally confirm that no scintillation anisotropy correlated to detector orientation exists in amorphous materials. These observations confirm that the scintillation anisotropy is not due to an external effect on the measurement system, and that a fixed, repeating structure is required for a scintillation anisotropy.

The directional dependence of the scintillation output in response to neutron interactions was measured in four stilbene crystals of various sizes and growth-methods. The scintillation anisotropy in these materials was approximately uniform, indicating that the crystal size, geometry, and growth method do not significantly impact the effect. Measurements of three additional pure crystals and two mixed crystals were made. These measurements showed

that 1) the magnitude of the effect varies with energy and material, 2) the relationship between the light output and pulse shape anisotropy varies across materials, and 3) the effect in mixed materials is very complex. These measurements have informed the hypothesis of the mechanism that produces the directional dependence. By comparing the various relationships between the light output and pulse shape anisotropy across materials, these measurements indicate that the preferred directions of singlet and triplet excitation transport may be the same in some materials and different in other materials.

The measurements performed in this work serve as a resource to groups who aim to correct for the scintillation anisotropy or employ it as a directional detection modality. Additionally, this work has advanced the understanding of what physical processes and properties dictate the magnitude and behavior of the scintillation anisotropy in a given material. It has added new information to the body of knowledge surrounding the scintillation mechanism in organic crystal scintillator materials. This information may be used to construct models to predict the scintillation anisotropy effect in materials that have not been experimentally characterized. Such work can contribute to work in producing a new generation of organic scintillator materials, advancing many applications in nuclear science and security.

In loving memory of
Stanley G. Prussin.

Contents

Contents	ii
List of Figures	v
List of Tables	x
1 The Scintillation Anisotropy	1
1.1 History of the Problem	2
1.1.1 Early Studies with α Particles	2
1.1.2 Characterization of the Scintillation Anisotropy for Neutron Interactions	2
1.1.3 Hypothesis for the Mechanism that Produces the Scintillation Anisotropy	5
1.2 Motivation	6
1.2.1 Informing the Hypothesis	6
1.2.2 Applying the Scintillation Anisotropy	7
2 Theory	9
2.1 Radiation Interactions with Organic Scintillators	10
2.1.1 Neutrons	10
2.1.2 Gamma Rays	11
2.1.3 Muons	13
2.2 Physical Chemistry of Organic Scintillator Materials	13
2.2.1 Molecular Orbital Structure of Organic Scintillators	14
2.2.2 Excitations and Light Emission	15
2.2.3 Theory of Neutron-Gamma Ray Pulse Shape Differences	19
2.2.4 Theory of Anisotropy	20
3 Methods	23
3.1 Expressing Proton Recoil Direction in Spherical and Polar Coordinates	23
3.2 Equipment and Data Acquisition	25
3.2.1 Crystal Preparation and Coupling	25
3.2.2 Rotational Stage	26
3.2.3 Electronics Rack and Neutron Source	29

3.3	Calculating Light Output and Quantifying Pulse Shape	29
3.3.1	Raw Pulse Processing	29
3.3.2	Calculating Light Output	30
3.3.3	Calibrating Light Output	31
3.3.4	Quantifying Pulse Shape	32
4	Investigating the Scintillation Anisotropy for Various Particle Types in Crystalline Anthracene	37
4.1	Neutron Measurements in Anthracene	38
4.1.1	Experimental Setup	38
4.1.2	Data Analysis	39
4.1.3	Measurement Results	39
4.1.4	Handling Statistical Error	43
4.1.5	Inferring Anthracene Crystal Axes Directions	45
4.2	Gamma-Ray Measurements in Anthracene	45
4.2.1	Experimental Setup	45
4.2.2	Data Analysis	46
4.2.3	Temperature Dependence	46
4.2.4	Measurement Results	49
4.2.5	Measurement Variability	49
4.3	Muon Measurements in Anthracene	50
4.3.1	Experimental Setup	51
4.3.2	Data Analysis	52
4.3.3	Measurement Results	53
4.4	Interpretation of Anthracene Results and Update to Hypothesis	54
5	Validation of Isotropic Response in Amorphous Scintillator Materials	57
5.1	Materials and Measurement Technique	57
5.2	First Observation of Temperature Dependence	58
5.3	Measurement Results and Analysis	59
5.4	Discussion	61
6	Investigation of Anisotropy Effect in Other Pure and Mixed Crystals	63
6.1	Investigating the Effect for Stilbene Detectors of Different Size and Quality	63
6.1.1	Samples Measured	64
6.1.2	Measurement Results	65
6.1.3	Assessment of Variability	72
6.2	Comparison of Effect Across Five Pure Materials	73
6.2.1	Materials Measured	73
6.2.2	Data Analysis Challenges	75
6.2.3	Measurement Results	75
6.2.4	Qualitative Analysis	80

6.2.5	Quantitative Analysis	81
6.2.6	Interpretation of Pure Materials Measurement Results and Update to Hypothesis	81
6.2.6.1	Different Directions of Preferred Transport for Singlets, Triplets in Two Dimensions	82
6.2.6.2	Different Directions of Preferred Transport for Singlets, Triplets in Three Dimensions	83
6.3	Measurements of Mixed Crystals	84
6.3.1	Materials Measured	84
6.3.2	Measurement Results and Analysis for BB:Stil	85
6.3.3	Measurements and Preliminary Results with DPAC:Stilbene	90
6.3.4	Interpretation of Mixed Material Results and Update to Hypothesis	92
6.3.5	Further Analysis	93
7	Conclusions	94
7.1	Summary of Anisotropy Observations	94
7.2	Current State of Scintillation Anisotropy Hypothesis	97
7.3	Future Work	99
A	MCNP5 Simulation of ^{137}Cs on Anthracene	101
A.1	Calculating Energy Deposited with MCNP5	101
A.2	Incorporating Detector Resolution	103
A.3	Aligning Simulated and Measured Light Output Distributions	106
	Bibliography	108

List of Figures

1.1	A schematic representation of the crystal axes of anthracene from Tsukada and Kikuchi [9]. The directions of maximum and minimum light output are along the c' - and b -axes, respectively. The saddle point in the scintillation distribution is located in the ac plane about 30° from the a -axis.	3
1.2	Ratio of maximum to minimum scintillation produced in anthracene by proton recoils traveling at different directions in the crystal as measured by previous groups [10, 8, 7].	4
2.1	Cartoon of a neutron-nucleus scatter interaction.	11
2.2	Cartoon of a Compton scatter interaction.	11
2.3	Shape of energy distribution for an electron recoil produced by a Compton scatter interaction. Figure from [2, p. 310].	12
2.4	Sketch of before and after configurations for <i>trigonal</i> or sp^2 hybridization, in which three equivalent hybrid orbitals are produced in the xy plane 120° from each other, and the p_z orbital is unchanged.	14
2.5	Diagram of molecular orbitals within anthracene. Shaded circles are s orbitals of hydrogen, shaded ovals are sp^2 hybrid orbitals of carbon, and open ovals are p_z orbitals of carbon. Bonds between two sp^2 orbitals or between an sp^2 orbital and a hydrogen s orbital are σ bonds. Delocalized bonds between p_z orbitals are π bonds and are indicated by the gray hexagonal network between p_z orbitals.	15
2.6	Jablonski diagram from [29, p. 3].	16
2.7	Time distribution of light emitted by organic scintillators from several prominent kinetic processes.	18
2.8	Impact on the time distribution of light emitted when the density of singlet and triplet excited states increases.	19
2.9	Common shape of two-dimensional histogram of fraction of delayed light vs. light output as measured in a PSD-capable organic scintillator.	20
2.10	Difference in excitation distribution after transport for heavy charged particle interactions at different directions.	22
3.1	2D and 3D visualization of directions in spherical coordinates.	24
3.2	Wrapping stilbene 316A sample.	25

3.3	PMT with plastic positioning guard and external sleeve.	26
3.4	Photos showing the procedure for mounting and wrapping detectors on the rotational stage.	26
3.5	Photo of anthracene detector on rotational stage used in neutron and gamma-ray measurements showing the two motor-driven axes of rotation around 1) the vertical axis and 2) the arm axis.	27
3.6	Cartoon representation of equipment indicating relevant directions used to calculate the direction of the proton recoil within the arbitrary crystal axes coordinate system.	28
3.7	Raw and baseline-subtracted pulses from an event recorded from the mixed field produced by a DT neutron generator incident on an anthracene detector.	30
3.8	Distribution of smoothed counts and differential of smoothed counts as a function of light output for a measurement of ^{137}Cs on anthracene. Key features used by the fit function for performing the light output energy calibration are indicated.	32
3.9	Baseline-subtracted pulse measured from a DT neutron event incident on anthracene. Samples i_1 , i_2 , i_3 , and i_P define regions relevant to calculating S	33
3.10	Raw events from the mixed field produced by a DT neutron generator measured by an anthracene detector. Calculating the maximum index of the smoothed pulse rather than the raw pulse provides a method for consistently locating i_p with respect to the rise time.	34
3.11	PSD distributions measured from the mixed field produced by a DT neutron generator on anthracene.	35
3.12	Screenshot of <i>FOM</i> comparison in Microsoft Excel for S distributions calculated on anthracene for various values of Δ_1 (rows) and Δ_2 (columns).	36
4.1	Density plot of L vs. S for the mixed radiation field produced by a DT neutron generator incident on anthracene at $(\theta, \phi) = (8.3^\circ, 131.7^\circ)$. The lines are drawn to show the cutoff point for selecting neutron events above 3000 keVee.	40
4.2	Light output spectrum for neutron events above 3000 keVee produced by a DT neutron generator incident on anthracene at $(\theta, \phi) = (8.3^\circ, 131.7^\circ)$. Points are experimental data, the line is the applied fit function, and the light output range $\hat{L} \pm \sigma$ in which interactions are selected as full energy interactions is indicated.	40
4.3	S distribution for neutron events with L within $\hat{L} \pm \sigma$ produced by a DT neutron generator incident on anthracene at $(\theta, \phi) = (8.3^\circ, 131.7^\circ)$. Points are experimental data, the line is the applied Gaussian fit function.	41
4.4	Response of anthracene crystal at various recoil directions to 14.1 MeV protons. Points indicate measurements and the gradients represent a smooth interpolation between measurements. Length of vertical bar on colorbar indicates average $\pm\sigma$ statistical error. The 2D distribution represents a hemisphere worth of 3D directions in spherical coordinates with ϕ increasing counter-clockwise and θ increasing radially outward as $r = \sqrt{1 - \cos\theta}$	41
4.5	Response of anthracene crystal at various recoil directions to 2.5 MeV protons.	42

4.6	Magnitude of change in light output produced by proton recoil events in anthracene as a function of proton energy [7, 8, 10].	43
4.7	Light output spectrum for ^{137}Cs gamma-ray events incident on anthracene at $(\theta, \phi) = (50^\circ, 178^\circ)$. The solid curve, upper and right axes correspond to an MCNP5 simulation. The data points, lower and left axes correspond to a measurement. Dashed lines indicate N_{478} and N_{CE} as found in the fit function, which produce a final \hat{L} value for the light output in summed digitizer channel units of a 478 keV electron recoil event.	47
4.8	Distribution of S values for events with light output in the range $\hat{L} \pm \sigma$ produced by ^{137}Cs gamma rays incident on anthracene at $(\theta, \phi) = (50^\circ, 178^\circ)$. Points are experimental data and the curve is the applied Gaussian fit function.	47
4.9	\hat{L} produced by a ^{137}Cs source at a fixed position at temperatures 22-28°C relative to that at 25°C.	48
4.10	\hat{S} produced by a ^{137}Cs source at a fixed position at temperatures 22-28°C relative to that at 25°C.	48
4.11	Response of anthracene crystal at various recoil directions for 478 keV electron recoils. See Fig. 4.4 caption for a detailed explanation of the anisotropy plots.	49
4.12	Cartoon of experimental setup for muon measurements with anthracene detector (not to scale).	52
4.13	Analysis of light output spectra in muon measurements.	53
4.14	Distribution of S values for events with light output in the range $\hat{L} \pm \sigma$ produced by cosmic muons in anthracene at paths 1 and 2. Points represent measurements, and overlying curves are the Gaussian fits applied. The vertical lines indicate the locations of the expected pulse shape parameters \hat{S}	54
5.1	Response of PSD-capable plastic scintillator at various recoil directions to 14.1 MeV protons for preliminary measurement without temperature characterization. See Fig. 4.4 caption for a detailed explanation of the anisotropy plots.	58
5.2	Response of PSD-capable plastic scintillator vs. time of measurement for preliminary measurement without temperature characterization.	59
5.3	Response of EJ309 liquid scintillator at various recoil directions to 14.1 MeV protons.	60
5.4	(a-b) Response of PSD-capable plastic scintillator at various recoil directions to 14.1 MeV protons and (c) approximate room temperature during measurements. See Fig. 4.4 caption for a detailed explanation of the anisotropy plots.	60
6.1	Photos of solution-grown and melt-grown stilbene samples.	65
6.2	(a-b) Response of solution-grown cubic stilbene crystal 316B to 14.1 MeV proton recoil events at various proton recoil directions and (c) approximate room temperature during measurements. See Fig. 4.4 caption for a detailed explanation of the anisotropy plots.	66

6.3	(a-b) Response of solution-grown cubic stilbene crystal 316B to 2.5 MeV proton recoil events at various proton recoil directions and (c) approximate room temperature during measurements. See Fig. 4.4 caption for a detailed explanation of the anisotropy plots.	67
6.4	Response of solution-grown cubic stilbene crystal 316A to 14.1 MeV proton recoil events at various proton recoil directions. See Fig. 4.4 caption for a detailed explanation of the anisotropy plots.	68
6.5	Response of solution-grown cubic stilbene crystal 314 to 14.1 MeV proton recoil events at various proton recoil directions. See Fig. 4.4 caption for a detailed explanation of the anisotropy plots.	68
6.6	(a-b) Response of melt-grown stilbene crystal at various recoil directions to 14.1 MeV protons and (c) approximate room temperature during measurements. See Fig. 4.4 caption for a detailed explanation of the anisotropy plots.	69
6.7	(a-b) Response of melt-grown stilbene crystal at various recoil directions to 2.5 MeV protons and (c) approximate room temperature during measurements. See Fig. 4.4 caption for a detailed explanation of the anisotropy plots.	70
6.8	Light output spectrum fit as measured for DT and DD neutrons incident on the cubic solution-grown stilbene sample B.	71
6.9	Magnitude of change in light output for proton recoil events at energies from 2.5-22 MeV in melt grown stilbene detectors as reported by Tsukada and Kikuchi [9], Brooks and Jones [7], and in this work. * A_L reported in [9] is for a polycrystalline sample, so it is likely lower than the true value.	72
6.10	Visualization of the crystal structure for anthracene, p-terphenyl, bibenzyl (BB), stilbene, and diphenylacetylene (DPAC).	76
6.11	Comparison of light output spectrum produced by 14.1 MeV neutron events incident on stilbene and DPAC. The solid vertical line indicates the position of the edge, and the dotted vertical lines indicate the width of the uncertainty around the position of the edge as found by the fit function.	77
6.12	Response of five pure crystals at various recoil directions to 14.1 MeV protons. See Fig. 4.4 caption for a detailed explanation of the anisotropy plots.	79
6.13	Illustration of excitation transport over time when singlet and triplet excitations have different directions of preferred transport.	83
6.14	Photos of samples measured in the mixed crystal study.	85
6.15	Visualization of the crystal structure for bibenzyl (BB), stilbene, and diphenylacetylene (DPAC).	86
6.16	Light output response and approximate room temperature during measurement of bibenzyl with dilute stilbene crystal at various recoil directions to 14.1 MeV protons. See Fig. 4.4 caption for a detailed explanation of the anisotropy plots.	87
6.17	Expected light output \hat{L} vs. measurement temperature for measurements of 14.1 MeV neutrons incident on the bibenzyl with dilute stilbene detector.	88
6.18	Response of stilbene and bibenzyl crystals at various recoil directions to 14.1 MeV protons. See Fig. 4.4 caption for a detailed explanation of the anisotropy plots.	89

6.19 (a-b, d-e, g-h) Response of stilbene and DPAC crystals at various recoil directions to 14.1 MeV protons and (c, f, i) approximate room temperature during measurements. See Fig. 4.4 caption for a detailed explanation of the anisotropy plots.	91
A.1 Visualization of MCNP5 simulation in VisEd. The yellow box is the aluminum shelf, the blue box is the wooden shelf, the right square on the right is the anthracene detector, and the red star indicates the location of the ^{137}Cs source.	103
A.2 F8 tally with 10 keV bins from MCNP5 simulation of ^{137}Cs incident on anthracene. Vertical dashed lines indicate the incident gamma-ray energy, $E_\gamma = 662$ keV, and the Compton edge energy, $E_{\text{CE}} = 478$ keV. The statistical errors produced by the simulation are smaller than the marker size in the plot.	104
A.3 Gaussian shape indicating full width at half maximum, FWHM, and peak centroid energy, E_0 . This plot corresponds to the detector response for a measurement of a monoenergetic source that deposits $E_0 = 478$ keV in a detector with resolution $R = \text{FWHM}/E_0 = 0.16 = 16\%$. Adapted from [2, ch. 4].	104
A.4 Gaussian resolution function $G(E)$ for centroid energies E_0 from 200 keV to 900 keV deposited in a detector with resolution $R = 16\%$	105
A.5 Light output spectrum for ^{137}Cs gamma-ray events incident on anthracene. The solid curve, upper and right axes correspond to an MCNP5 simulation. The data points, lower and left axes correspond to a background-subtracted measurement. Lines indicate the positions of N_{peak} , N_{478} and L_{478}	107

List of Tables

2.1	Stopping powers and ranges for proton and electron recoils traveling through stilbene of density $\rho = 0.97 \text{ g/cm}^3$	13
3.1	Δ_1 and Δ_2 values as used for calculating S for all PSD-capable materials measured in this work.	36
4.1	Magnitude of Anisotropy Measured in Expected Light Output \hat{L} and Pulse Shape Parameter \hat{S} Produced by Proton Recoil Events in Anthracene	42
4.2	Variability in pulse shape and light output in proton recoil events in anthracene.	44
4.3	Variability in Pulse Shape and Light Output in Electron Recoil Events in Anthracene.	50
4.4	Summary of Measurements Made on Anthracene Sample for Interactions at Directions 1 and 2.	55
4.5	Comparison of excitation dynamics for proton recoil events along the b and c' axis. Dynamics for proton recoil events along the a axis are hypothesized to be in between those along the b - and c' -axes.	56
5.1	Variability in directional measurements of liquid and plastic scintillators.	61
6.1	Characteristics of stilbene materials measured, including steps used in calculating S in the pulse shape analysis.	64
6.2	Magnitude of change in \hat{L} and \hat{S} values measured for stilbene detectors. *Indicates only maximum and minimum angles from DT measurements were measured at DD energies.	71
6.3	Normalized variability, σ_{anis}/μ , introduced by the anisotropy in directional measurements of stilbene samples.	73
6.4	Summary of pure crystal materials characterized with their optimal pulse shape parameter Δ_1 and Δ_2 values.	74
6.5	Crystal structure unit cell length for pure crystal materials [40].	75
6.6	List of which feature in the \hat{S} distribution corresponds to which feature in the \hat{L} distribution for the five pure materials measured.	80
6.7	Magnitude of change in \hat{L} and \hat{S} values measured for 14.1 MeV proton recoil events in various pure crystal detectors (using stilbene 316B from Sec. 6.1.2).	81

6.8	Summary of optimal pulse shape parameter Δ_1 and Δ_2 values for PSD-capable mixed crystal materials.	85
6.9	Magnitude of change in \hat{L} and \hat{S} values measured for 14.1 MeV proton recoil events in pure stilbene (using stilbene 316B from Sec. 6.1.2), pure bibenzyl, and a (50:50) BB:Stil mixed detector.	90
6.10	Magnitude of change in \hat{S} values measured for 14.1 MeV proton recoil events in pure stilbene (using stilbene 316B from Sec. 6.1.2), pure DPAC, and an (80:20) DPAC:Stil mixed detector.	92

Acknowledgments

This work would not have been possible without the guidance and support of many people. First and foremost, I want to thank my late adviser Stanley Prussin. Stan was the most influential person in my time at Berkeley, and although he was not able to read this dissertation, he shaped every word of it. From Stan I learned to think critically, to question all assumptions, and to love my work. He taught me the value in chatting over a cup of coffee or taking a walk around campus. Most importantly, he supported me wholeheartedly with constant encouragement and enthusiasm.

Secondly I would like to thank Dr. Erik Brubaker for his mentorship on this work. Many things happened by chance during my time at Berkeley, but the luckiest was finding this dissertation project under Erik's mentorship. I have learned so much from his vast knowledge of experimental physics, and his creativity and attention to detail will remain with me in my future work.

I would like to thank Professor Karl van Bibber, Professor Kai Vetter, and Professor Naomi Ginsberg for serving on my committee and providing me technical and professional advice over the years. I would also like to thank Professor Michael Nacht for challenging me to think outside of the technical box, and Professor Lee Bernstein for sharing his love of teaching with me.

To my group members, I could not have asked for better folks to see every week. Araina Hansen, I loved sharing an office with you and seeing you every day. Laurence Lewis, you brought energy and enthusiasm to our group meetings. David Weisz, you helped us navigate the many challenges we faced. Eva Uribe, my chemistry counterpart, I am so glad to know you and I am proud of our work together.

I was very lucky to have worked with many talented individuals at Sandia National Laboratories. Thank you to my group members for welcoming me, starting with Scott Kiff who recruited me to Sandia during my undergraduate days at the University of Michigan. Thank you to my fellow students Aaron Nowack, Mateusz Monterial, Kyle Weinfurther, David Goodman, and many more for your camaraderie. Everyone in my group helped me in some way over the years with valuable technical and professional insights. Notably, John Steele provided me with continual help in building and troubleshooting my experimental setup, and Jacquie Reardon solved the many logistical challenges of lab work. Patrick Feng helped me interpret my results from the perspective of a physical chemist. Lorraine Sadler provided me with critical career advice and mentorship, and Craig Tewell helped me understand the importance of my work on a larger scale.

Thank you to everyone who was on this journey with me. Cameron Bates, you are a great friend and talented scientist, and I'm glad to have had you by my side the past nine years. Madicken Munk, you continue to amaze me, and I could ask for no one better to chair my advisory committee. Lakshana Huddar, your positive energy always lifts my spirits. Zack Beauvais, Micah Folsom, Anagha Iyengar, Alejandra Jolodosky, Sasha Asghari, Tomi Akindele, and Matt Proveaux, thank you for all the fun we had. To my many role models

who showed me the ropes, thank you for setting the bar high. Katy Huff, Rachel Slaybaugh, Melinda Sweany, Denia Djokic, and Christina Leggett, you all inspire me.

Thank you to Natalia Zaitseva, Andy Glenn, and their colleagues at LLNL for many long conversations interpreting my problem and my results, and for providing me numerous samples to measure.

Finally, I would like to thank my family and friends for their moral support throughout this process and especially my husband, Charlie, for his constant love and understanding.

This material is based upon work supported by the National Science Foundation Graduate Research Fellowship Program under Grant No. DGE 1106400. This material is further based upon work supported by the Department of Energy National Nuclear Security Administration under Award Number DE-NA0000979 through the Nuclear Science and Security Consortium.

Chapter 1

The Scintillation Anisotropy

Organic scintillator materials have long been used for radiation detection. They are particularly useful because of their ability to detect both neutrons and gamma rays and distinguish between them using a technique known as pulse shape discrimination (PSD). Organic scintillators exist in plastic, liquid, and crystal forms. In contrast to liquids, the solid plastic and crystal scintillators are non-toxic and subject to minimal thermal expansion, making them more robust for field applications. Crystal scintillators, such as anthracene and stilbene, generally outperform liquid and plastic scintillators in PSD [1], however, crystal scintillators are fragile, limited in size, and exhibit a directional variation [2, p. 223]. For these reasons, many users opt to use liquid and plastic materials.

There is renewed interest in organic crystal scintillators following the development of a new growing method that produces large crystals with excellent light output and neutron-gamma PSD [3, 4, 5]. The directional variation remains an interesting and largely not understood effect in crystalline materials. In the 1950s through the 1970s, several groups measured the directional dependence of the scintillation produced by α particles [6] and by proton recoils from neutron interactions [7, 8, 9, 10]. These measurements demonstrated that both the amount of light emitted and the time distribution of the light emitted vary as a function of heavy charged particle direction within the crystal axes. The mechanism that is responsible for the directional dependence in heavy charged particle interactions is not fully understood, but it has been hypothesized to result partly from preferred directions of molecular excitation transport in the crystal [7]. The hypotheses that ion channel effects or directional variations in stopping power dE/dx are responsible for the effect have been explored and found to not be responsible for the observed scintillation anisotropy [7, 10].

The directional dependence degrades the energy resolution and widens the distribution of pulse shapes produced in these materials when heavy charged particles (e.g. nuclear recoils from neutron interactions) interact at many angles in the crystal axes. For some applications, this serves as an obstacle, and these materials would serve better if one could correct for the directional dependence or synthesize new materials that eliminate it. Other applications exist in which the directional dependence could be exploited for a compact directional detection system. In this case, it may be preferred to use materials with a large directional dependence,

or synthesize new materials with an enhanced directional dependence. For either application, a greater understanding of the magnitude and behavior of the effect and the mechanism that produces it is important to correct for, exploit, enhance, or eliminate the effect.

1.1 History of the Problem

1.1.1 Early Studies with α Particles

Much of the early work that revealed the scintillation anisotropy in organic crystal scintillators was performed in the 1950s and 60s in Göttingen, Germany. This work primarily focused on α particle interactions on anthracene, but the effect was measured on other crystals as well. Observations included:

- The scintillation response of bulk crystalline anthracene depends on the direction of incident α particles with respect to the crystal axes. The α particles that interact perpendicular to the main cleavage plane ab , or along the c' -axis, produce maximum scintillation, and the α particles that interact in the direction parallel to the b -axis produce minimum scintillation [6, 11]. It should be noted that in his work, Heckmann states that the minimum scintillation was produced along the a -axis, but his crystal axes were defined differently. The minimum scintillation was produced along the shortest crystal axis that is generally named the b -axis in modern work.
- The ratio of maximum to minimum scintillation produced for 5.3 MeV alpha particles in anthracene is approximately 1.55. The ratio increases as the α particle energy decreases [6, 11].
- The scintillation anisotropy is also present in thin anthracene and *trans*-stilbene samples. In thin films of anthracene, the direction of maximum light output varied slightly with sample thickness [12].
- The scintillation anisotropy in *trans*-stilbene has a different dependence on the crystal axes than in anthracene. The minimum scintillation in *trans*-stilbene is produced along the c' -axis [12].
- This effect was also measured in 11 additional organic crystal scintillators, and appeared to be a common feature in monoclinic organic scintillators [13].
- The magnitude of the scintillation anisotropy decreases with decreasing temperature. For 6.05 and 8.79 MeV α particles incident on an anthracene crystal, ratios of the maximum to the minimum scintillation yield are 1.55-1.45 at room temperature and 1.2 at 20 K. [14].

1.1.2 Characterization of the Scintillation Anisotropy for Neutron Interactions

Measurements of the scintillation anisotropy for neutron interactions in many crystal scintillators have been reported in the literature [7, 8, 9, 10, 15]. Anthracene has been the most

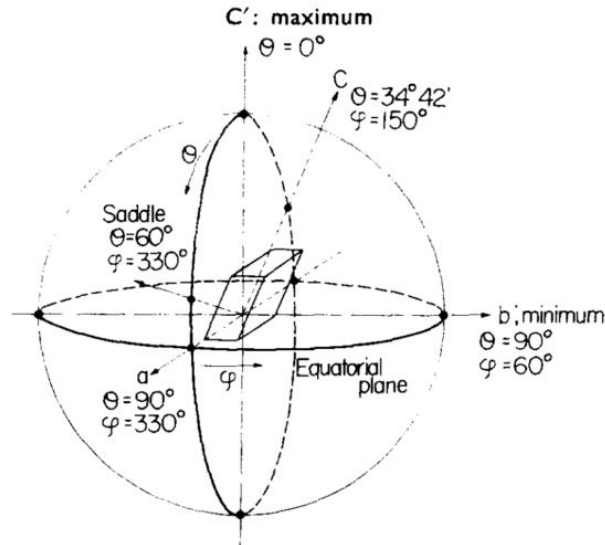


Figure 1.1: A schematic representation of the crystal axes of anthracene from Tsukada and Kikuchi [9]. The directions of maximum and minimum light output are along the c' - and b -axes, respectively. The saddle point in the scintillation distribution is located in the ac plane about 30° from the a -axis.

extensively characterized organic crystal scintillator. It was found that for proton recoils, the maximum scintillation light is produced along the c' -axis, and the minimum scintillation light is produced along the b -axis [8, 9]. This agrees with the result for α particle interactions [6, 11]. Tsukada and Kikuchi went further to show that the saddle point in the scintillation light distribution occurs in the ac plane, 30° off of the a -axis [9]. These directions are shown on a schematic of the anthracene crystal axes in Fig. 1.1.

The scintillation anisotropy produced by proton recoil events in anthracene was measured at many proton recoil energies. Figure 1.2 shows the magnitude of the effect as a function of energy as measured by previous authors. All measurements are consistent with the trend that the magnitude of the effect decreases for increasing proton recoil energy. Because these authors used analog electronics and their data analysis methods are ambiguous, there is uncertainty as to whether the data provided by each author is directly comparable. It appears that Tsukada *et al.* calculated the ratio of the maximum to minimum pulse height, while the other authors calculated the ratio of the maximum to minimum total scintillation produced.

The anisotropy in the pulse shape was first noted by Tsukada and Kikuchi who demonstrated that the anisotropy of the fast and slow decay components were different. For 3.7 MeV proton recoils in anthracene, the anisotropy of the fast decay component was more significant than that of the slow component [9]. This was confirmed and investigated further by Brooks and Jones who measured the light output L vs. pulse shape S distribution for 1 – 22 MeV proton recoils in anthracene as a function of direction [7]. Brooks and Jones

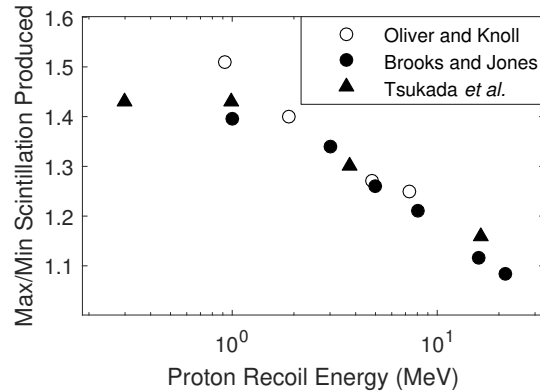


Figure 1.2: Ratio of maximum to minimum scintillation produced in anthracene by proton recoils traveling at different directions in the crystal as measured by previous groups [10, 8, 7].

demonstrated a number of things including:

- The range of S values produced for a given particle type in a given L range is larger at one direction than another.
- The magnitude of change in the pulse shape increases as the proton recoil energy increases.
- The pulse shape anisotropy is large enough for proton recoils of energy 5 MeV and greater to distinguish between proton recoils traveling along the maximum and minimum directions.

Other organic crystal materials were measured including *trans*-stilbene [7, 9, 15], p-terphenyl [7, 10, 15], naphthalene [7], quaterphenyl [7], diphenylanthracene (DPA) [15], and tetraphenyl butadiene (TPB) [15]. The scintillation anisotropy was shown to be approximately the same across materials for a given proton recoil energy, but the pulse shape anisotropy varies greatly across materials [7, 15].

The relationship between the light output and pulse shape produced by proton recoils at different directions was shown to differ across materials. In *trans*-stilbene and p-terphenyl, the amplitude and pulse shape anisotropies had the same dependence on proton recoil direction; in anthracene the two had the same shape but different signs. In TPB, the maxima and minima of the light output and pulse shape anisotropies did not line up [15]. This shows that the effect is complex in magnitude and behavior across materials, and much remains to be understood.

Lastly, previous work noted that no anisotropy is observed with electron excitation from gamma-ray interactions, though no quantitative measurements were provided [6, 7].

1.1.3 Hypothesis for the Mechanism that Produces the Scintillation Anisotropy

Several physical mechanisms have been hypothesized to be responsible for producing the scintillation anisotropy. The leading hypothesis is that there are directional variations in the amount of quenching within the crystal. Quenching is a general term for any process that reduces the light emission. Tsukada *et al.* hypothesized that the effect was caused by directional variations of the quenching term $B \cdot dE/dx$ in the following formula for the relationship between specific scintillation dS/dx and the energy loss dE/dx :

$$\frac{dS}{dx} = \frac{A \cdot dE/dx}{1 + B \cdot dE/dx},$$

where dS/dx is the specific scintillation, dE/dx is the stopping power, A is a constant related to the scintillation efficiency, and B is the quenching factor [16]. This formula was proposed by Birks as a semi-empirical relationship based on experimental observations.

Tsukada *et al.* calculated that a change of 40% in $B \cdot dE/dx$ as a function of direction in the quenching term would explain the directional variation in the scintillation [10]. Several quenching processes are bi-molecular, so it follows naturally that the geometrical arrangement and electronic structure of molecules in a crystal could produce directionally dependent quenching factors. However, further work by Kratochwill demonstrated through measurements of α -particles of variable energy demonstrated that the scintillation anisotropy in anthracene cannot be explained by assuming the quenching parameter B alone is direction-dependent [17]. Thus, the problem is more complicated than a single directionally-dependent component.

The equation proposed by Birks is limited in its simplicity. The evolution of excitations within these organic scintillator materials is quite complicated and much remains to be understood. By considering the behavior of excitations on an individual basis, one can consider additional scenarios that the equation does not account for. Such excitations in organic scintillators are often referred to as excitons, and considered as localized quasiparticles that move about and interact with one another in the material.

Brooks and Jones hypothesized that the anisotropy effect may be due to anisotropy in exciton transport. As of the start of this dissertation, this stood as the leading hypothesis. This hypothesis will be explained and illustrated in Sec. 2.2.4. The scintillation light output and pulse shape both depend on the exciton density as a function of time and may be thought of as a competition between kinetic processes including transport, quenching, light emission and many others. The scintillation anisotropy in anthracene is consistent with a model in which excitations travel preferentially within the *ab*-plane [7]. This dissertation will update the hypothesis to account for the varied magnitude and behavior of the scintillation anisotropy in different materials.

Channelling was also considered as a potential mechanism responsible for the anisotropy effect. In crystalline materials, there may be paths or “channels” that a recoil particle can travel through the crystal and experience a much lower stopping power than in other

directions. Channelling was ruled out as a cause of the anisotropy because the light output and pulse shape anisotropies do not experience sharp features, as would be expected for an effect that results from channelling [7]. Instead, there are broad features in the light output and pulse shape that are more likely to be caused by effects related to the crystal or molecular structure.

The lack of anisotropy in electron recoil events was hypothesized by Brooks and Jones to be attributed to the multiple large-angle scattering events that electrons undergo as they slow down [7]. This scattering makes it such that electron recoils do not maintain a unique direction. Alternately, the lack of anisotropy in electron recoil events may be due to the low stopping power dE/dx . This will be investigated in Sec. 4.3.

1.2 Motivation

1.2.1 Informing the Hypothesis

The hypothesis presented in Sec. 1.1.3 lays the ground work for explaining the scintillation anisotropy, but it is incomplete. This dissertation aims to contribute to the body of knowledge surrounding these materials through new measurements and analysis across a variety of organic crystal scintillators. Many interesting questions remain, including the following that will be considered in this dissertation:

- What physical mechanisms are responsible for producing the anisotropy?
- Why does the magnitude of the scintillation anisotropy vary with heavy charged particle energy?
- How does the anisotropy impact the performance of an organic crystal scintillator?
- Why is no anisotropy observed for electron recoil events generated by gamma-ray interactions?
- Does the anisotropy vary between like materials of different size and shape?
- Why does the scintillation anisotropy vary in magnitude and behavior in different scintillators?
- Does a scintillation anisotropy exist in mixed crystals?

The scintillation anisotropy presents an interesting effect through which one can learn more about the internal energy transfer processes in these materials. Beyond explaining the directional dependence, this work may contribute to the broader theoretical understanding of how excited states evolve in these materials. During its lifetime, an excitation may undergo a number of kinetic processes that change its state. These include but are not limited to transport to a neighboring molecule, conversion into a different type of excitation, or de-excitation by light emission or another non-luminescent pathway. While some, such as light emission, are well characterized and supported by a robust theoretical understanding, many are merely hypothesized to explain experimental observations. The scintillation anisotropy indicates that the relative likelihood of each process varies based on the local arrangement

of molecules. By studying the light emission generated from different spatial distributions of excitations, it may be possible to determine what is the more favorable arrangement of molecules for producing desired light emission properties. This information would assist chemists and material scientists who are working to develop the next generation of organic scintillator materials with superior performance.

A major gap of knowledge is the incomplete understanding of how energy is lost to non-luminescent processes, which are broadly referred to as quenching. If it is true that the scintillation anisotropy is partly due to directionally-dependent rates of quenching, studying the effect would provide information on what crystal and molecular properties minimize quenching. This problem is closely related to inefficient charge collection or recombination in organic photovoltaics (PVs) and organic light-emitting diodes (OLEDs), respectively. A more complete understanding of the specific factors that control these processes is therefore expected to lead to advances in each of these contemporary applications.

A major goal in improving the next generation of organic scintillator detectors is minimizing cost. Crystal growth is a complex art, and these crystals must be grown in relatively large sizes in order to increase the interaction rate. If the quality of the signal from a single radiation interaction is increased by improving the material's energy resolution or neutron-gamma PSD performance, smaller detectors could be used to achieve the same confidence level as current detectors, thereby decreasing the required size and cost of the system.

1.2.2 Applying the Scintillation Anisotropy

Beyond updating the base of knowledge surrounding these materials, a detailed characterization of the scintillation anisotropy may serve useful in a number of applications. A simple consideration for using a crystal whose scintillation anisotropy has been characterized is to place the crystal with respect to the radiation source in the orientation that produces a favorable light output distribution. Birks notes in his book that organic crystal scintillator detectors were traditionally mounted with the *ab* cleavage plane on the face of the photomultiplier tube, so that radiations generally interact in the direction of the *c'*-axis [18, p. 261]. In anthracene, this is a favorable direction because it produces the maximum scintillation response to heavy particles. For *trans*-stilbene, however, this direction produces the minimum scintillation response. Birks estimates that an improvement of up to 26% in the response to α -particles and neutrons (recoil protons) can be obtained if the source-detector configuration is adjusted so that radiation is incident in the direction of the *b*-axis in *trans*-stilbene.

Another opportunity is to employ the directional dependence as a tool for measuring nuclear properties. As a companion study to the scintillation anisotropy characterization that Brooks and Jones performed [7], Brooks and Jones used the anisotropic scintillation response in anthracene in order to study the polarization in neutron-proton scattering [19]. In this work, Brooks and Jones used polarized neutron beams obtained from the $^3\text{H}(d,n)$ reaction, scattering the beams in monocrystalline anthracene and observing the asymmetry of the associated recoil protons. They utilized the directional dependence to determine the left-right asymmetry of the proton recoils within the crystal. This technique offered

experimental simplicity and improved statistical accuracy compared to the usual double scattering technique.

A rather sophisticated application of the scintillation anisotropy would be to employ the effect as a directional neutron detection modality. One example of an application that could use a directional neutron detector based on the scintillation anisotropy would be a search scenario in which an inspector or emergency responder is walking through a storage facility or shipyard with restricted access where they believe a threat source, such as a significant quantity of plutonium behind high-Z shielding [20], is located. In this case, directional information about neutron interactions would provide assistance in discriminating against background events. An excess of counts in a given direction would indicate that a threat source may be in that direction. Brooks and Jones first suggested this application [7], and Brubaker and Steele explored the idea in greater detail through Monte Carlo studies [15]. Brubaker and Steele showed that it is possible to reconstruct the source distribution using the scintillation anisotropy and a model of neutron elastic scattering. Though experimental resolution effects were not fully included, producing an optimistic model, their work serves as a proof of principle. They emphasize that such a reconstruction is not trivial and requires sophisticated imaging techniques. Additionally, the scintillation anisotropy would need to be measured at lower proton recoil energies in order to be relevant to applications in which fission-energy neutrons are measured.

A third potential application for the scintillation anisotropy is in dark matter searches. Dark matter is a hypothetical type of matter that does not emit or interact with electromagnetic radiation, making it invisible to the entire electromagnetic spectrum. The observed gravitational dynamics in the universe are not explained by matter observed, so it is hypothesized that unobserved dark matter exists in galactic halos consisting of weakly interacting massive particles (WIMPs). Dark matter particles can be detected by observing their elastic scattering interactions with the nuclei of detectors on earth. Such measurements must be able to measure 10 keV nuclear recoils and discriminate between nuclear recoils and gamma-rays to reject background. Since the WIMPs originate in a dark matter halo, they travel in a fixed direction toward the earth, so the direction of the recoil nucleus offers a signature for WIMPs [21]. In fact, the most convincing signature of WIMPs appears in the directions of nuclear recoils [22]. The anisotropic scintillation response in organic scintillators has been considered as a candidate for observing the directions of nuclear recoils produced by WIMPs [22, 23, 24, 25]. While it appears a feasible approach, there are many remaining technical challenges [24].

Each of these applications would benefit from a more thorough study of the effect. A comprehensive comparison of the effect across materials is important for any user selecting which crystalline material to use. This dissertation presents studies to characterize the effect as a function of radiation type, crystal size and quality, and crystal material. Still, further opportunities exist to learn more about these materials, and much work remains before they can be used as directional detectors.

Chapter 2

Theory

There are many stages between radiation entering a detector and an electronic pulse being measured. The following is a brief discussion of those stages. Additional information about general functionality of scintillation detectors is available in [2, ch. 8].

Radiation enters the detector and deposits energy in the organic scintillator by the processes described in Sec. 2.1. A fraction of the energy deposited produces electronic excitations within the material's molecular π -orbitals, whose structure will be described in Sec. 2.2.1. A fraction of those excitations will de-excite via light emission, as described in Sec. 2.2.2. This light may enter the photomultiplier tube and be converted into an electronic pulse, which is then digitized and recorded as a signal. The digital processing technique used on these pulses is described in Sec. 3.3.1.

From start to finish, there are many opportunities for signal loss. For example, not all of the energy deposited creates excitations of the π -orbitals, not all of those excitations de-excite via light emission, and not all of the light is collected and converted into a pulse by the PMT. The final digitized pulse represents a time distribution of the light emitted by the organic scintillator modified by the light collection and electronics of the PMT. For all of the measurements in this work, the light collection and PMT properties are fixed, and any variability in the signal introduced by those stages is minimized.

Thus, the scintillation anisotropy that is measured in this work characterizes anisotropy within the stages from the radiation interaction to the light emission. The scintillation anisotropy is not from an anisotropy in the light collection or electronics, as will be demonstrated in Chap. 5. In order to focus on topics relevant to the physical mechanisms that produce the scintillation anisotropy, this section will discuss the detection process from the radiation interaction to the light emission and will not discuss the light collection or digitization.

2.1 Radiation Interactions with Organic Scintillators

Organic scintillator materials are made of carbon and hydrogen, and have densities on the order of 1 g/cm³. The interactions observed for neutron, gamma rays, and muons are generally similar across all organic scintillators and may be summarized by the radiation interactions described in the following sections.

2.1.1 Neutrons

A dominant interaction between a neutron and an organic scintillator that produces measurable signal is an elastic scatter of a neutron on a hydrogen or carbon nucleus, producing a nuclear recoil in the material. Figure 2.1 shows a simple cartoon of this interaction. After the interaction, the nuclear recoil departs the interaction with the following energy:

$$E_{\text{recoil}} = 4E_0 \cos^2 \alpha \left(\frac{A}{(1+A)^2} \right),$$

where E_0 is the incoming neutron energy, α is the angle between the initial direction of the neutron and the nuclear recoil direction, and A is the atomic number of the nucleus. For interactions with hydrogen or carbon nuclei, this becomes:

$$E_{\text{recoil}}(\text{H}) = 4E_0 \cos^2 \alpha \left(\frac{1}{(1+1)^2} \right)^2 = \left(\frac{A \cdot 1}{A} \right) E_0 \cos^2 \alpha = E_0 \cos^2 \alpha, \text{ and}$$

$$E_{\text{recoil}}(\text{C}) = 4E_0 \cos^2 \alpha \left(\frac{12}{(1+12)^2} \right)^2 = \left(\frac{4 \cdot 12}{169} \right) E_0 \cos^2 \alpha \approx 0.284 E_0 \cos^2 \alpha.$$

While in many cases the cross section for neutron interactions with hydrogen and carbon are comparable, the energy deposited to a carbon nucleus target is much less than to a hydrogen nucleus target. For this reason, hydrogen produces a greater light output signal and makes an important target nucleus. Interactions with hydrogen nuclei will be used in this work to characterize the response to neutron interactions.

The hydrogen nucleus, or proton recoil, travels with energy $E_{\text{recoil}} = E_n \cos^2 \alpha$, where α is the angle between the initial direction of the neutron and the proton recoil path. A proton that is scattered in the forward direction will travel with the full energy $E_{\text{recoil}} = E_n$. This is the only proton recoil energy that corresponds to a unique direction, as a proton recoil that travels at a non-zero angle may be anywhere on the surface of a cone defined by the half-angle α about the incident neutron direction.

As the proton recoil travels through the anthracene crystal, it deposits its energy via inelastic collisions with electrons in the medium. Because the proton is so much more massive than the electrons, the proton does not lose much of its energy or change its direction by much per interaction, so it travels in a quasi-straight path. Also, the larger mass of a proton recoil means that it will travel with a much lower velocity than an electron recoil or muon of the same energy, so the proton recoil deposits a relatively large dE/dx .

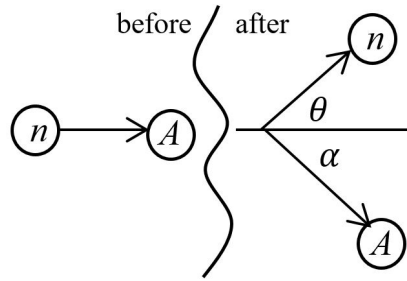


Figure 2.1: Cartoon of a neutron-nucleus scatter interaction.

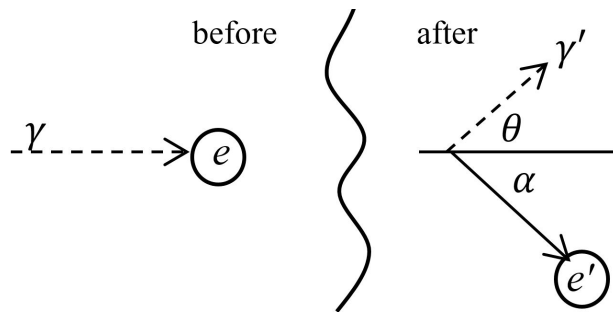


Figure 2.2: Cartoon of a Compton scatter interaction.

2.1.2 Gamma Rays

Gamma rays of energies typical of radioactive sources interact primarily via Compton scattering in organic scintillator materials. In a Compton scatter event, an incoming gamma ray interacts with a loosely bound, nearly free atomic electron. Part of the gamma-ray's initial energy is given to the electron, which is released from the atom. The gamma ray departs the interaction scattered at angle θ and a recoil electron is produced traveling at angle α , as shown in Fig. 2.2.

The kinetic energy of the recoil electron is given as:

$$E_2 = E_0 \left(\frac{\frac{E_0}{m_e c^2} (1 - \cos \theta)}{1 + \frac{E_0}{m_e c^2} (1 - \cos \theta)} \right), \quad (2.1)$$

where E_0 is the incident gamma-ray energy, $m_e c^2$ is the rest mass of an electron, and θ is the angle at which the gamma ray departs the interaction.

For an incident gamma ray of energy E_γ , the highest energy electron recoil that can be produced occurs in the head-on collision in which the gamma ray scatters at angle $\theta = \pi$ from its initial direction and the recoil electron departs the interaction in the forward direction $\alpha = 0$. The maximum recoil electron energy is then:

$$E_2 = E_0 \left(\frac{2 \frac{E_0}{m_e c^2}}{1 + 2 \frac{E_0}{m_e c^2}} \right). \quad (2.2)$$

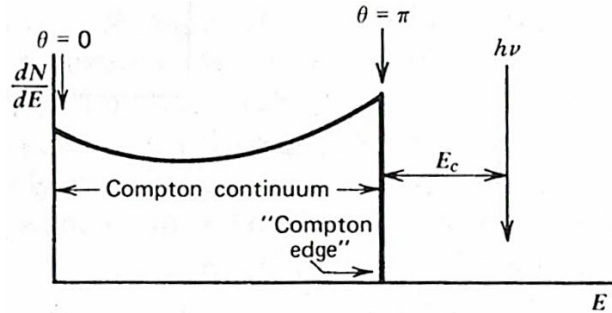


Figure 2.3: Shape of energy distribution for an electron recoil produced by a Compton scatter interaction. Figure from [2, p. 310].

In most circumstances, all scattering angles will occur in the detector, producing a continuum of electron recoil energies ranging from 0 up to the maximum from Eq. (2.2). The shape of the energy distribution of Compton recoil electrons is predicted by the Klein-Nishina cross section [2, p. 51] and shown in Fig. 2.3. The maximum electron recoil energy at $\theta = \pi$ is called the Compton edge, as it makes a sharp edge on the recoil electron energy distribution.

The recoil electron may deposit its energy on other electrons in the medium through collisions with electrons, causing a cascade of electrons in the material. Although the initial direction of the electron recoil is fixed for a Compton edge event, the electron undergoes wide angle scattering as it interacts with other electrons of the same mass, so the electron does not travel in a straight path as it deposits its energy.

The dE/dx deposited by the electron recoil at a given energy is less than that by a proton. A detailed explanation of this is provided in [26]. Briefly, the dE/dx deposited by a charged particle depends only on its velocity and ionic charge as:

$$dE/dx \propto \frac{Z^2}{v^2}.$$

For a proton and an electron traveling at the same kinetic energy, the proton will have a much lower velocity due to its higher mass. Thus, the stopping power dE/dx of the proton will be higher than that of the electron, and the range of the proton will be lower. For reference, Table 2.1 shows the stopping power and ranges for proton and electron recoils at energies from 0.1 MeV-10 MeV. This table shows that a proton's stopping power at a given energy is approximately two orders of magnitude higher than that of an electron at the same energy, and a proton's range is approximately two orders of magnitudes less than that of an electron. It should be noted that the stopping powers in this table are for protons or electrons at each energy, and a proton that deposits 10 MeV in a material will start with the stopping power listed in the table at 10 MeV, and as it slows down its stopping power will increase.

Table 2.1: Stopping powers and ranges for proton and electron recoils traveling through stilbene of density $\rho = 0.97 \text{ g/cm}^3$.

		Proton		Electron	
Energy (MeV)	dE/dx (MeV/cm)	Range (cm)	dE/dx (MeV/cm)	Range (cm)	
0.1	8.78E+02	1.31E-04	3.89E+00	1.51E-02	
0.5	3.96E+02	8.57E-04	1.92E+00	1.87E-01	
1	2.49E+02	2.52E-03	1.74E+00	4.65E-01	
5	7.54E+01	3.79E-02	1.84E+00	2.73E+00	
10	4.34E+01	1.29E-01	1.99E+00	5.34E+00	

2.1.3 Muons

Muons are elementary particles that like electrons have electric charge of $-1e$ and spin of $1/2$, but mass about 207 times that of the electron. Muons at cosmic ray energies are minimally ionizing particles, as they interact very little with matter except by ionization and deposit energy proportional to the amount of matter they pass.

Cosmic muons are produced via cosmic ray interactions with matter in the upper atmosphere. These “cosmic muons” are born with approximately 6 GeV energy and reach sea level with about 4 GeV energy. The muon flux at sea level is approximately 1 muon per square centimeter per minute. Since muons that travel toward the earth at non-vertical angles have traveled a longer path length, the flux of muons depends on their angle with respect to earth. The observed muon flux distribution is proportional to $\cos^2(\theta)$, where θ is the angle from the vertical [27].

Since the muon is essentially a massive electron, the muon interacts in an organic scintillator similarly to an electron, depositing energy to electrons in the medium with low dE/dx relative to a proton recoil. Because a muon’s mass is so much greater than an electron’s mass, a muon experiences minimal changes in its direction as it interacts with electrons in the medium, producing a quasi-straight path. The energy deposited by a muon interacting in an organic scintillator is proportional to the path length that it travels in the detector, so the deposited energy distribution will be equal to the path length distribution multiplied by a conversion factor.

2.2 Physical Chemistry of Organic Scintillator Materials

In order to understand the physical mechanism that produces the scintillation anisotropy in organic crystal scintillators, one should consider the basic physical chemistry and material structure. These topics can provide a foundation for identifying properties that may explain why the anisotropy differs across materials. A short discussion follows.

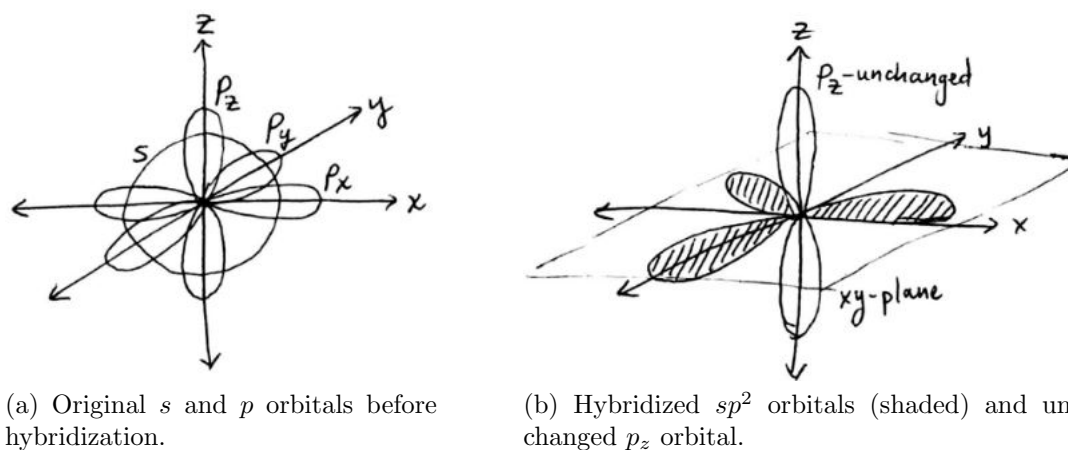


Figure 2.4: Sketch of before and after configurations for *trigonal* or sp^2 hybridization, in which three equivalent hybrid orbitals are produced in the xy plane 120° from each other, and the p_z orbital is unchanged.

2.2.1 Molecular Orbital Structure of Organic Scintillators

Organic scintillators are all built on the structure of the benzene ring, C_6H_6 . The electronic configuration of the ground state of carbon ($Z = 6$) is $1s^2 2s^2 2p^2$. In forming the benzene ring, one of the $2s$ electrons can be considered to be excited into a $2p$ state, making the electronic configuration $1s^2 2s 2p^3$ [18, ch. 3]. In the benzene ring, the $2s$ and two of the $2p$ atomic orbitals are hybridized to sp^2 hybrid orbitals as shown in Fig. 2.4. The sp^2 hybrid orbitals lay within the xy plane and the unchanged p_z orbital extends above and below the xy plane [28, ch. 1].

In molecules such as anthracene that contain benzene rings in their structure, the sp^2 hybrid orbitals of neighboring carbon atoms bond with each other to produce localized σ bonds in a planar ring structure. Carbon atoms on the outside of the molecule also form σ bonds with the $1s$ orbitals of hydrogen atoms. These bonds are shown as the bonds between shaded orbitals on a schematic of the anthracene molecular structure in Fig. 2.5.

The p_z atomic orbitals of each carbon atom, which extend above and below the plane of the ring structure, bond with the other p_z orbitals to produce delocalized π molecular orbitals. These bonds are shown as the network between the unshaded orbitals in Fig. 2.5. The π bonds contribute additional stabilization to the molecule and reduce the C-C bond length [28, ch. 1]. The motion of the π electrons can be described independently of the σ electrons. The π electrons move freely throughout the π network of the system as if the π network were one-dimensional in a line or ring. It is the excited states of these π -electron systems that are responsible for the luminescence in these materials.

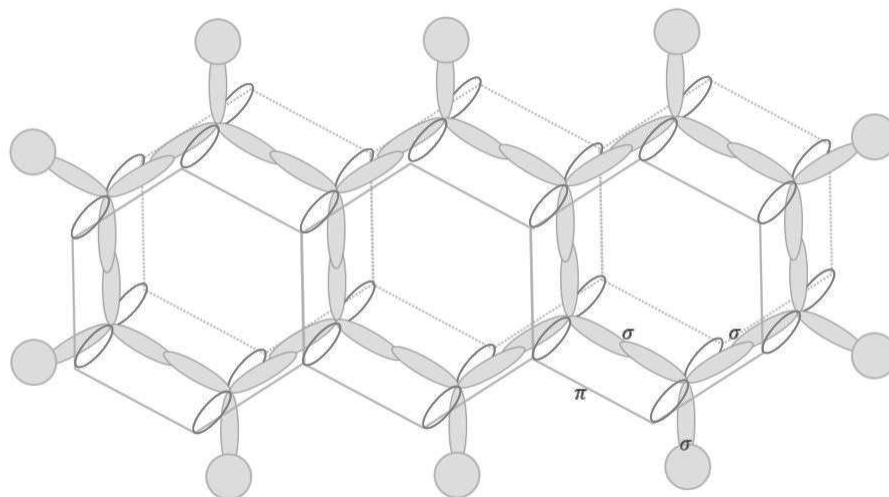


Figure 2.5: Diagram of molecular orbitals within anthracene. Shaded circles are s orbitals of hydrogen, shaded ovals are sp^2 hybrid orbitals of carbon, and open ovals are p_z orbitals of carbon. Bonds between two sp^2 orbitals or between an sp^2 orbital and a hydrogen s orbital are σ bonds. Delocalized bonds between p_z orbitals are π bonds and are indicated by the gray hexagonal network between p_z orbitals.

2.2.2 Excitations and Light Emission

After radiation interacts in an organic scintillator, a fraction of the energy deposited into the system produces excitations of the molecular π -electrons. Figure 2.6 shows a *Jablonski diagram*, a schematic representation of the energy levels for the π -electrons. Excitations may be populated by valence electrons being promoted directly to excited states or by ions recombining with ionized molecules into excited configurations. Excitations may be in singlet configurations, which are in the left column of Fig. 2.6 and have valence electrons with opposite spin, or triplet configurations which are in the right column of Fig. 2.6 and have valence electrons with parallel spin.

In the case of a direct excitation from ground state into an excited state, the electron is almost always promoted to an excited singlet state because a transition to a triplet excited state is spin forbidden. Ion recombination may produce singlet or triplet excited states, and based purely on statistical grounds, triplet states are produced about 75% of the time [18, ch. 3].

The Franck-Condon principle states that because an electronic transition occurs so quickly, there is little or no initial geometry change in the molecular system, even though populating a higher energy orbital will ultimately induce the nuclei to reconfigure. Thus, a transition between electronic levels will often produce an excited vibrational state of the final electronic level in order to preserve the molecular geometry. These states appear in Fig. 2.6 as the intermediate thinner-lined levels between electronic states. The excited vibrational state

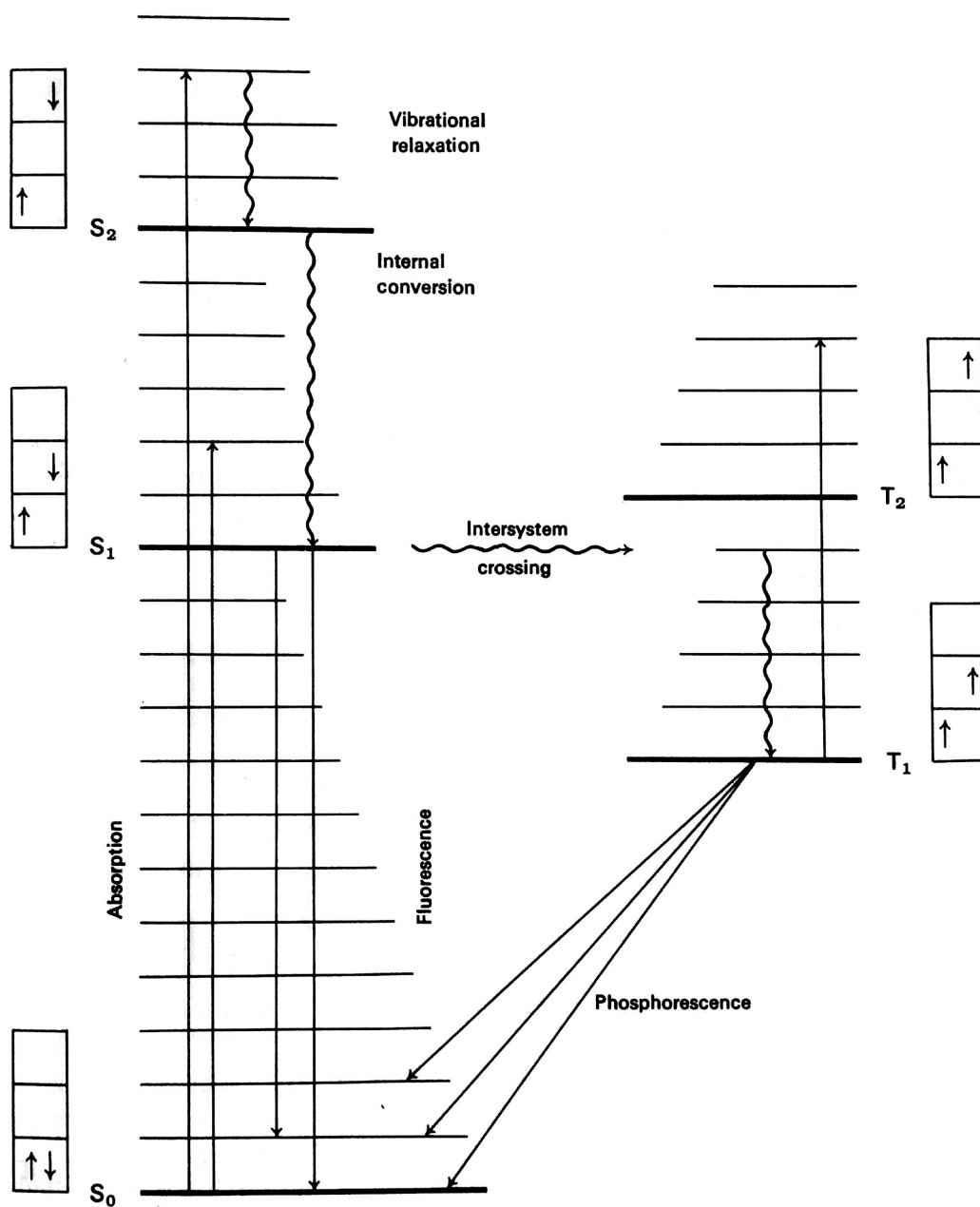


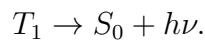
Figure 2.6: Jablonski diagram from [29, p. 3].

quickly relaxes to the zeroth-vibrational state within that electronic level. The electronic excited states may undergo numerous kinetic processes including de-excitation by light emission. Some of these processes are drawn in Fig. 2.6. A short discussion follows on prominent kinetic process that excitations undergo.

Fluorescence: A de-excitation from the lowest singlet excited state S_1 to the ground state S_0 via light emission is known as fluorescence and occurs on the ns time scale. The energy of the excited state is emitted as an optical photon with energy $h\nu$, where h is Planck's constant and ν is the photon's frequency. This transition may be expressed as:

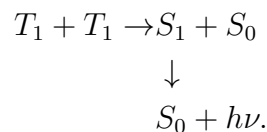


Phosphorescence: A de-excitation from the lowest triplet excited state T_1 to the ground state S_0 via light emission is known as phosphorescence. Because phosphorescence is spin-forbidden, it occurs slower than fluorescence, generally on the μs -ms time scale. Phosphorescence may be expressed as:



If fluorescence and phosphorescence were the only transitions available to the system, the light output distribution would look like that shown in Fig. 2.7a. The solid red line illustrates the light emission from fluorescence of the singlet excitations. This emission occurs rapidly over a short time scale. The solid blue line illustrates the light emission from phosphorescence of the triplet excitations. This emission occurs over a much longer time scale, so the relative amplitude of the phosphorescence emission to the fluorescence emission is much less. In fact, the phosphorescence occurs slowly enough that it is essentially unobserved by the measurement system used in this dissertation, and the contribution from phosphorescence can be removed from the distribution of light emitted.

Triplet-triplet annihilation: Triplet energy may be observed on a shorter time scale through another kinetic process known as triplet-triplet annihilation [30]. In this process, two triplet states in close proximity interact and annihilate into one singlet excited state and one singlet ground state. The singlet excited state may then de-excite by fluorescence on the ns time scale. Triplet-triplet annihilation may be expressed as:



This emission is known as delayed fluorescence, as the time of the light emission is determined by the time required for the two triplet states to travel through the material and annihilate. Because the rate of triplet-triplet annihilation increases as triplets interact more, the amount of delayed fluorescence produced by triplet-triplet annihilation will depend on the density of triplet excitations in the material and their mobilities. Figure 2.7b shows the light output distribution with delayed fluorescence contributed by triplet-triplet annihilation as a dashed line.

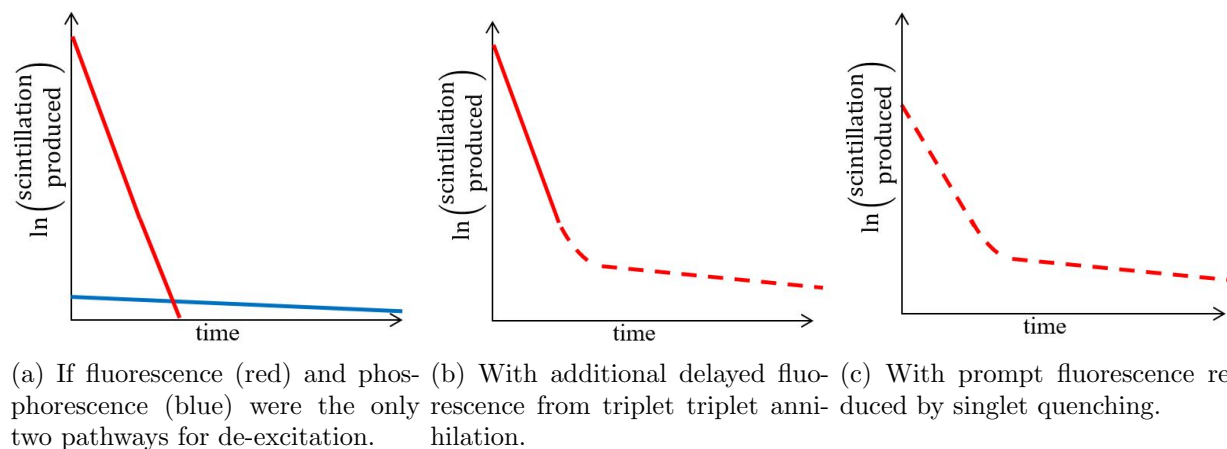
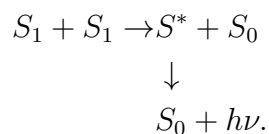


Figure 2.7: Time distribution of light emitted by organic scintillators from several prominent kinetic processes.

Singlet quenching: Another interactive process that affects the amount of light produced is singlet quenching. In this process, two singlet states interact and push one into a super-excited state, leaving the other in ground state. The super-excited singlet state may relax and later de-excite via fluorescence, but the total amount of fluorescence has been decreased from two possible photons to one. Thus, the amount of prompt light produced by singlet fluorescence from the initial singlet population is reduced. Figure 2.7c shows how the prompt light, now also in dashed red, has been reduced by singlet quenching. The degree to which the prompt light is reduced depends on the density of singlet excitations. Singlet quenching may be expressed as:



Excitation transport: Excitations may move to neighboring molecules in the material, changing the spatial distribution of excitations over time. Singlet excitation transport proceeds via Forster energy transfer, a near-field dipole-dipole interaction [31]. Thus, the preferred direction of singlet transport depends on the direction of the transition dipole moment of the molecule. Triplet excitation transport occurs via Dexter energy transfer whose rate depends on the spatial and energetic overlap of the two molecular waveforms [31]. Thus, the rate of triplet transport will be greater in directions with strong π -orbital overlap between molecules, which depends on the molecular and crystal structure.

There are many other kinetic processes available to these excitations that play a less prominent role in shaping the distribution of light emitted in organic scintillators from radiation interactions. A few, such as intersystem crossing and internal conversion, are shown in Fig. 2.6. Others may be discussed in additional references including [18, 28, 29].

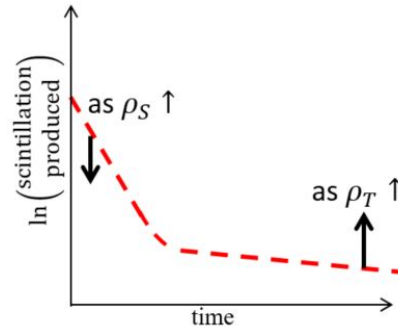


Figure 2.8: Impact on the time distribution of light emitted when the density of singlet and triplet excited states increases.

2.2.3 Theory of Neutron-Gamma Ray Pulse Shape Differences

Because the likelihoods of the interactive processes described in Sec. 2.2.2 depend on the spatial distribution of excitations, the relative rate of each process will change depending on the density of excited states, and radiation types that deposit energy with different dE/dx will lead to different light emission properties. Both the total amount of light emitted and the time distribution of the light emitted may vary. Pulse shape discrimination (PSD) is applied to analyze the characteristics of the pulse produced to determine what type of radiation interacted.

In applications using organic scintillator materials, pulse shape discrimination (PSD) is often aimed at identifying whether an event was produced by a neutron or gamma-ray event. As discussed in Sec. 2.1, neutron interactions produce nuclear recoils in the material, which deposit their energy with higher dE/dx than the electron recoils produced by gamma-ray interactions. The higher dE/dx produces higher excitation densities, leading to more triplet-triplet annihilation and singlet quenching. Figure 2.8 shows the impact on the time distribution of light emitted as changed by a higher excitation density. In the earlier time region, a higher density of singlet excitations acts to reduce the amount of prompt light emitted. In the later time region, a higher density of triplet excitations acts to increase the amount of delayed light emitted.

Since neutron events produce a higher density of excited states, the prompt light emission is less than that produced by a gamma-ray event. Also, the delayed light emission is more than that produced by a gamma-ray event. Thus, when the entire light distribution is evaluated, there is more delayed light relative to the total amount of light emitted in the signal produced by neutron interactions. Additionally, the total amount of light emitted per energy deposited is less for neutron events than for gamma-ray events. This is because the decrease in light output due to singlet quenching is generally more than the increase in light output from triplet-triplet annihilation.

The differences in the scintillation produced by neutrons and gamma rays types can be measured in the shape of the electronic pulses measured. Many quantitative techniques exist

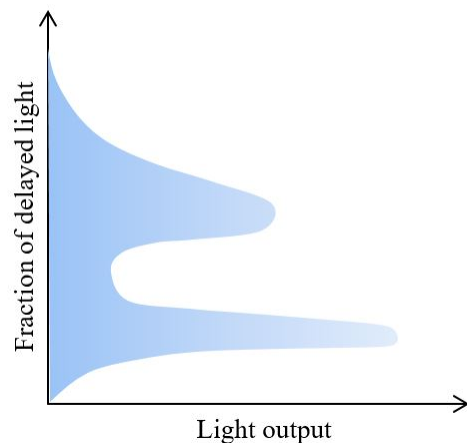


Figure 2.9: Common shape of two-dimensional histogram of fraction of delayed light vs. light output as measured in a PSD-capable organic scintillator.

for implementing neutron-gamma pulse shape discrimination (PSD) [32]. A simple method often referred to as the “tail-to-total” method or “charge integration” method is described in detail in Sec. 3.3.4. Briefly, the pulse shape is quantified in a one-dimensional parameter by calculating the fraction of light in a delayed time region of the pulse. Figure 2.9 shows an illustration of the common shape of a “PSD plot,” a two-dimensional histogram of the pulse shape parameter vs. light output. The upper band is populated by neutron events that produce a higher fraction of delayed light, and the lower band is populated by gamma-ray events. Based on the pulse shape parameter and light output for a given event, the event can be attributed to a neutron or gamma-ray event.

The illustration in Fig. 2.9 shows that the discrimination between neutron and gamma-ray events is better at higher energies because the two regions are easier to distinguish. At lower energies, the neutron and gamma-ray distributions overlap and events in the overlapping region can not be assigned a particle type. This makes for an energy threshold below which pulse shape discrimination can not be performed or is limited.

The shape of the PSD plot varies between materials in how well the neutron and gamma-ray bands are resolved. For instance, anthracene has much wider bands than does stilbene, so the resolution between the bands at a given energy is better in stilbene, decreasing the PSD energy threshold and making it a better material for performing PSD.

2.2.4 Theory of Anisotropy

In many crystal organic scintillators, the light output and pulse shape produced by heavy charged particles vary depending on the direction of the charged particle with respect to the crystal axes. This has been measured in numerous materials for alpha particles and nuclear recoils produced by neutron interactions. A summary of previous work is provided in Sec. 1.1. The history of the hypothesis for explaining the directional dependence is provided

in Sec. 1.1.3, and will be illustrated here. This hypothesis will be revisited in Sec. 4.4, Sec. 6.2.6, and Sec. 6.3.4 to account for new findings from this dissertation.

The leading hypothesis is that there are directional variations in the relative rates of kinetic processes available to molecular excitations in the material, partly due to preferred directions of excitation transport. It has been demonstrated through measurements that excitons do in fact travel at different rates at different directions in organic crystal scintillator materials. For example, Akselrod *et al.* measured the rates of triplet diffusion along the a , b , and c -axes in tetracene and found that transport is seven times more rapid in the b -direction than in the c -direction [31].

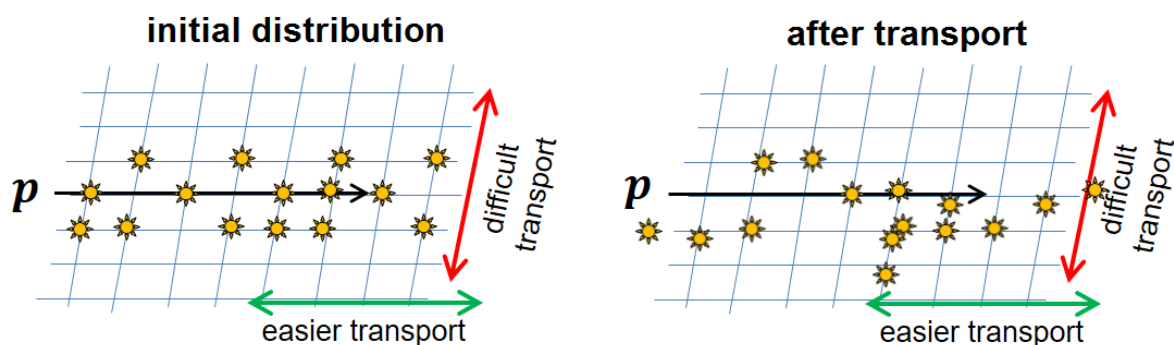
Differences in the scintillation produced by neutron interactions at different angles can be considered a more subtle version of differences in the scintillation produced by neutron and gamma-ray interactions. As discussed in Sec. 2.2.3, the difference in signal produced by neutron and gamma-ray events is largely due to their different stopping powers dE/dx and, in turn, the different excitation densities that each produces in organic scintillator materials. Figure 2.8 illustrated how the prompt light emission is reduced and the delayed light emission is increased when the density of singlet and triplet excitations increases. The difference in excitation densities produced by neutron and gamma-ray events may be considered a gross effect compared to very small differences in the excitation density that results from proton recoil events produced by neutron interactions at different directions and subject to preferred directions of excitation transport.

A basic illustration of this in two dimensions is shown in Fig. 2.10. In Fig. 2.10a, the proton recoil, indicated by the p to the left of the cartoon, interacts horizontally, producing a roughly horizontal spatial distribution of excitations. Those excitations then move over time in all directions, but more rapidly along the horizontal axis. Although transport is possible in the vertical direction, it is less likely. Thus, excitations move more easily within their distribution and the density of excitations remains high even after much transport has occurred.

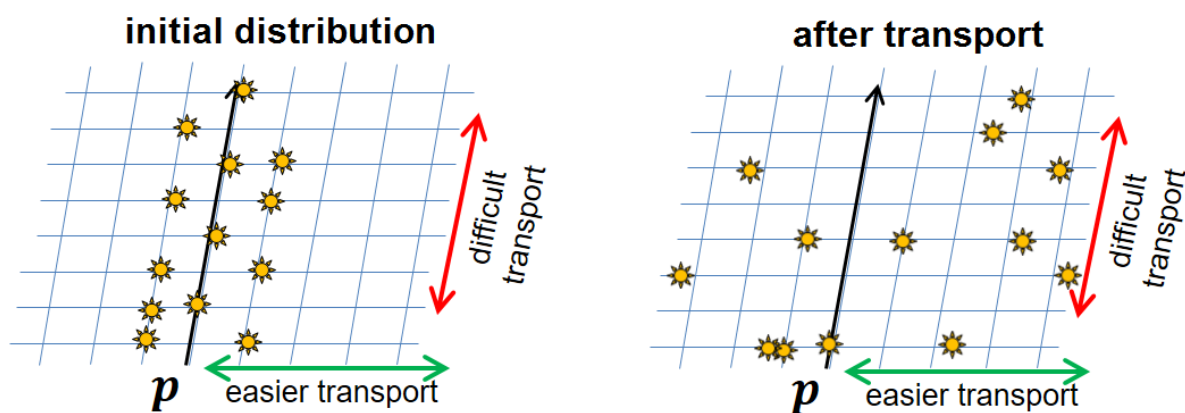
Figure 2.10b shows the other extreme in which the proton recoil interacts along the vertical axis that has more difficult transport. Over time, the excitations transport preferentially in the horizontal direction away from the initial distribution. Thus, the density of excited states drops over time as the excitations disperse.

Since the excitation density decreases over time for the case shown in Fig. 2.10b, the likelihood of the interactive kinetic processes including singlet quenching and triplet-triplet annihilation is less after transport has occurred than in the case shown in Fig. 2.10a. Following the same logic responsible for the difference in light output and pulse shape between neutron and gamma-ray events, the case in which the density of excitations remains high in Fig. 2.10a would produce less prompt and more delayed scintillation than the case in Fig. 2.10b, producing an overall higher fraction of delayed light.

The anisotropy may be distilled into two values measured from each event. The first is the total amount of light emitted, L , which depends primarily on the rate of singlet quenching as the light emission is dominated by the fluorescent emissions from the initial singlet population. While delayed light contributes to L , it is a small contribution on the



(a) Example of excitation distribution when charged particle interacts along the direction of easy transport.



(b) Example of excitation distribution when charged particle interacts along the direction of difficult transport.

Figure 2.10: Difference in excitation distribution after transport for heavy charged particle interactions at different directions.

order of a few percent. The pulse shape parameter, S , which measures the time distribution of light emitted by calculating the fraction of light in a designated delayed region, is affected by both singlet quenching and triplet-triplet annihilation.

Chapter 3

Methods

This chapter provides details on the experimental and data analysis methods used in this work. Sec. 3.1 explains the coordinate system used to visualize the scintillation anisotropy measurements in two dimensions. Sec. 3.2 provides information about the measurement equipment including the detector preparation, data acquisition electronics, rotational stage apparatus, and radiation sources. The digital signal processing used to calculate the light output and pulse shape for each event are discussed in Sec. 3.3.1

3.1 Expressing Proton Recoil Direction in Spherical and Polar Coordinates

In many of the crystal samples characterized in this work, the crystal axis directions are unknown, so an arbitrary set of axes has been established. The direction of the interacting particle will be described in (θ, ϕ) spherical coordinates. As shown in Fig. 3.1a, θ represents the angle between the direction and the positive z -axis, and ϕ represents the angle between the positive x -axis and the projection of the direction on the xy -plane. Because an interacting particle traverses the same crystalline structure in the forward and backward directions, only one hemisphere worth of interaction directions must be measured.

In order to visualize the proton recoil direction in two dimensions, polar coordinates defined by $(r(\theta), \phi)$ were used. The relationship $r(\theta)$ was constructed as follows in order to make area on the two-dimensional representation proportional to solid angle in three-dimensional space. The differential solid angle in spherical coordinates is equal to:

$$d\Omega = \sin \theta d\theta d\phi,$$

and the differential area in polar coordinates is equal to:

$$dA = r(\theta) dr d\phi.$$

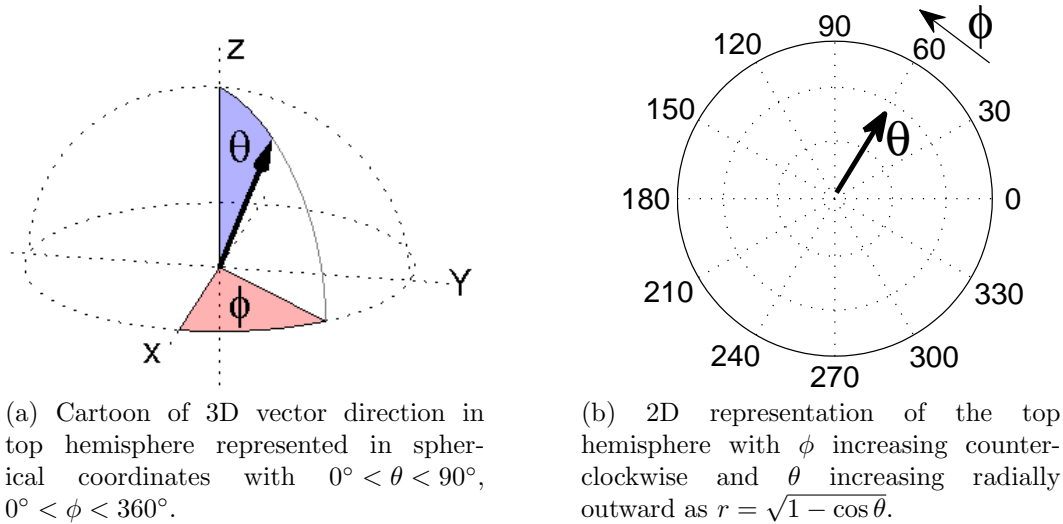


Figure 3.1: 2D and 3D visualization of directions in spherical coordinates.

The next step is to look for a real function $r(\theta)$ such that $d\Omega \propto dA$. Insert a proportionality constant B :

$$B d\Omega = dA, \text{ and}$$

$$B \sin \theta d\theta d\phi = r(\theta) dr d\phi.$$

Let $r(\theta) = \sqrt{1 - \cos \theta}$, and calculate $r dr$ in terms of θ :

$$r(\theta) = \sqrt{1 - \cos \theta},$$

$$dr = \frac{(\sin \theta d\theta)}{2\sqrt{1 - \cos \theta}},$$

$$r(\theta) dr = \sqrt{1 - \cos \theta} \frac{(\sin \theta d\theta)}{2\sqrt{1 - \cos \theta}}, \text{ and}$$

$$r(\theta) dr = \frac{1}{2} \sin \theta d\theta.$$

This definition of $r(\theta)$ makes the proportionality constant $B = 1/2$. For a range of $0^\circ < \theta < 90^\circ$, the radial range on the two-dimensional polar plot is $0 < r < 1$, which is intuitive for the viewer. Thus, the directions in the top hemisphere of space can be represented in two dimensions as shown in Fig. 3.1b.

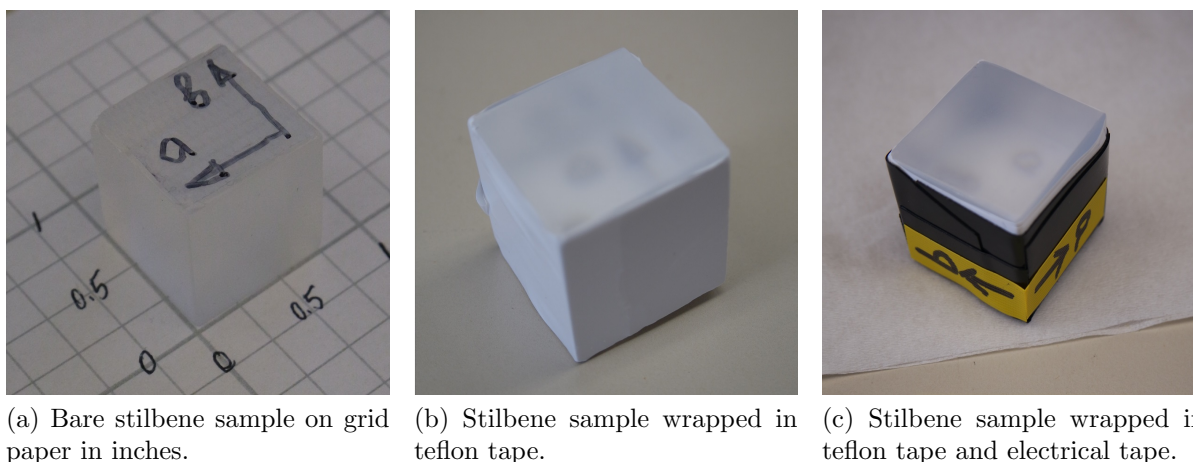


Figure 3.2: Wrapping stilbene 316A sample.

3.2 Equipment and Data Acquisition

3.2.1 Crystal Preparation and Coupling

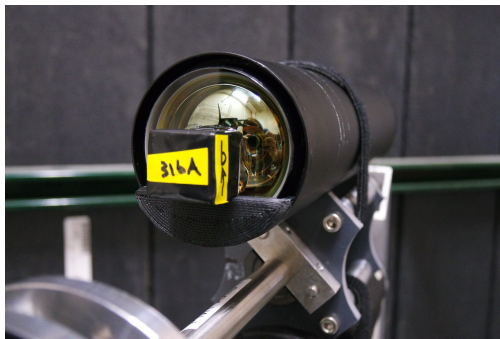
For all measurements, the crystals were wrapped in teflon tape to increase light reflection and collection by the photomultiplier tube (PMT). Figure 3.2a shows the stilbene 316A sample before it is wrapped. This sample has known crystal axes, which are labeled on the sample. The grid paper under the sample is in units of inches to provide a reference to the sample's size. Figure 3.2b shows stilbene sample 316A wrapped in teflon tape. Some samples, including stilbene 316A, were wrapped in an outer layer of black electrical tape for easier handling, as shown in Fig. 3.2c.

Crystals were then mounted to the face of a 60 mm Hamamatsu H1949-50 photomultiplier tube (PMT) assembly using V-788 optical grease. In order to place the crystal samples in a consistent orientation on the face of the PMT, plastic guards were 3D-printed to fit on to the face of the PMT and provide a reference position. Figure 3.3 shows the face of a PMT with the plastic guard in place. The plastic sleeve off to the side is placed over the face of the PMT after the crystal is mounted to block out any external light.

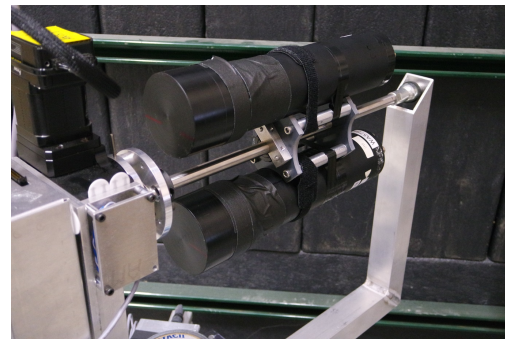
For the directional measurements, crystals were mounted while the PMT was already mounted to a rotational stage that will be described in Sec. 3.2.2, and a level was used to make sure that the plastic guard on the face of the PMT was parallel to the floor, as shown in Fig. 3.4a. The straight edge of the crystal was pushed against the plastic guard so that the edge of the crystal was level with the floor. This was done to better control the positioning of the crystal so that if a given crystal is removed and replaced, it will be placed in the exact same orientation with respect to the PMT and rotational stage. After the crystal was mounted to the face of the PMT, the black plastic sleeve was placed over the face of the PMT and a horizontal line was drawn on the face of the sleeve. This allowed for



Figure 3.3: PMT with plastic positioning guard and external sleeve.



(a) Stilbene 316A crystal mounted to PMT face.



(b) Detectors wrapped in gaffer's tape to block external light.

Figure 3.4: Photos showing the procedure for mounting and wrapping detectors on the rotational stage.

the detector to be removed from the rotational stage in order to wrap the interface between the PMT and the sleeve in gaffer's tape to block any light from entering. Then the detector was reattached to the rotational stage and a level was used to position the line drawn on the face of the sleeve to be horizontal, as shown in Fig. 3.4b. This ensured that the edge of the crystal inside the sleeve was also parallel to the ground.

3.2.2 Rotational Stage

Each detector was mounted to a rotational stage, shown in Fig. 3.5, that is capable of positioning the detector at any angle in 4π with respect to the incident neutron direction. The stage has two motor-driven axes of rotation: 1) The circular turn table on which the support is mounted can rotate 360° around the vertical axis, and 2) the metal arm on which

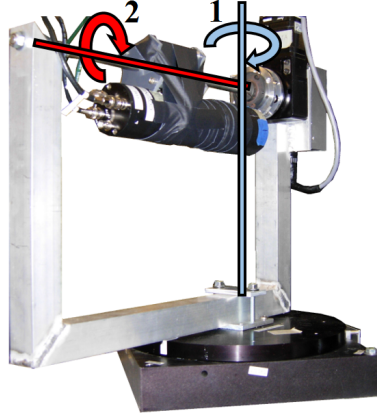


Figure 3.5: Photo of anthracene detector on rotational stage used in neutron and gamma-ray measurements showing the two motor-driven axes of rotation around 1) the vertical axis and 2) the arm axis.

the detector is mounted can rotate 360° on its axis.

For a given measurement, the incident neutron direction is calculated with respect to the crystal axes given the rotation angles of the two stage axes, the position of the generator, and the slight offset between the detector and the intersection of the stage axes. This calculation will require Rodrigues' rotation formula:

$$\vec{v}_{\text{rot}} = \vec{v} \cos \theta + (\vec{k} \times \vec{v}) \sin \theta + \vec{k}(\vec{k} \cdot \vec{v})(1 - \cos \theta),$$

where \vec{v} is the initial vector, \vec{k} is a unit vector describing the axis of rotation around which \vec{v} rotates, and θ is the angle of rotation. For convenience, the following notation will be used to refer to \vec{v}_{rot} as calculated by Rodrigues' rotation formula:

$$\vec{v}_{\text{rot}} = R(\vec{v}, \vec{k}, \theta).$$

Figure 3.6a shows a top view of the rotational stage in the lab space. This configuration shows the home position before any rotation has been performed. The two axes of rotation are the table axis \vec{k}_{table} , corresponding to rotation of the circular turn table around a vertical axis, and the arm axis \vec{k}_{arm} , corresponding to rotation around the metal arm to which the detector is mounted. The origin $(0, 0, 0)$ of the lab coordinate system is at the intersection of these two axes.

$$\begin{aligned} \vec{k}_{\text{table}} &= [0 \ 0 \ 1], \text{ and} \\ \vec{k}_{\text{arm}} &= [\cos(40^\circ) \ -\sin(40^\circ) \ 0]. \end{aligned}$$

For many materials measured in this work, the a -, b -, and c ' crystal axes directions within the sample are unknown. Because of this, an arbitrary set of orthogonal a -, b -, and c '-axes

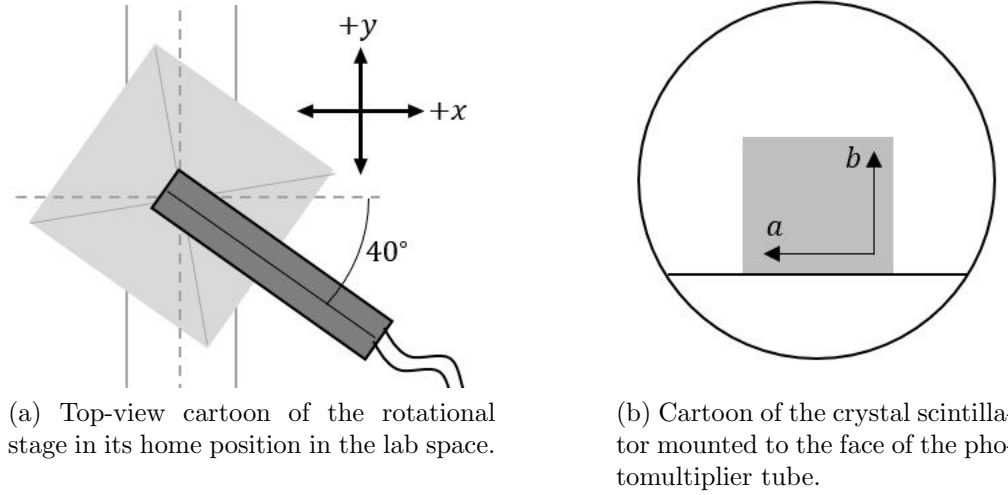


Figure 3.6: Cartoon representation of equipment indicating relevant directions used to calculate the direction of the proton recoil within the arbitrary crystal axes coordinate system.

are established for the crystal within the detector in the home position on the rotational stage. As shown in Fig. 3.6b, the a and b axis are established as the horizontal and vertical vectors on the plane of the face of the PMT, respectively. The c' axis is in the direction of the length of the PMT. The initial position of the crystal is characterized by the unit vectors in the direction of the a -, b -, and c' -axes and the initial position \vec{x} of the crystal:

$$\begin{aligned}\vec{a}_0 &= [\sin(40^\circ) \quad \cos(40^\circ) \quad 0], \\ \vec{b}_0 &= [0 \quad 0 \quad 1], \\ \vec{c}'_0 &= [\cos(40^\circ) \quad -\sin(40^\circ) \quad 0], \text{ and} \\ \vec{x}_0 &= (0 \quad 0 \quad -2.5).\end{aligned}$$

The first rotation performed is around the arm axis by angle θ_{lab} . The resulting crystal axes directions and crystal position are:

$$\begin{aligned}\vec{a}_1 &= R(\vec{a}_0, \vec{k}_{\text{arm}}, \theta_{\text{lab}}), \\ \vec{b}_1 &= R(\vec{b}_0, \vec{k}_{\text{arm}}, \theta_{\text{lab}}), \\ \vec{c}'_1 &= R(\vec{c}'_0, \vec{k}_{\text{arm}}, \theta_{\text{lab}}), \text{ and} \\ \vec{x}_1 &= R(\vec{x}_0, \vec{k}_{\text{arm}}, \theta_{\text{lab}}).\end{aligned}$$

The second rotation performed is around the table axis by angle ϕ_{lab} . The final crystal axes

directions and crystal position are:

$$\begin{aligned}\vec{a}_2 &= R(\vec{a}_1, \vec{k}_{\text{table}}, \phi_{\text{lab}}), \\ \vec{b}_2 &= R(\vec{b}_1, \vec{k}_{\text{table}}, \phi_{\text{lab}}), \\ \vec{c}_2 &= R(\vec{c}_1, \vec{k}_{\text{table}}, \phi_{\text{lab}}), \text{ and} \\ \vec{x}_2 &= R(\vec{x}_1, \vec{k}_{\text{table}}, \phi_{\text{lab}}).\end{aligned}$$

The direction of an incident particle entering the crystal from a source at position \vec{S} is calculated as:

$$\vec{p} = \vec{x}_2 - \vec{S}.$$

Finally, \vec{p} can be calculated with respect to the final crystal axes directions in spherical coordinates (θ, ϕ) as described in Sec. 3.1. θ is calculated as the angle between \vec{p} and \vec{c}_2 :

$$\theta = \cos^{-1} \left(\frac{\vec{p} \cdot \vec{c}_2}{|\vec{p}| |\vec{c}_2|} \right).$$

ϕ is calculated as the angle between the a -axis and the projection of \vec{p} onto the ab -plane, \vec{p}_{ab} :

$$\begin{aligned}\vec{p}_{ab} &= \vec{c}_2 \times (\vec{p} \times \vec{c}_2), \text{ and} \\ \phi &= \cos^{-1} \left(\frac{\vec{p}_{ab} \cdot \vec{a}_2}{|\vec{p}_{ab}| |\vec{a}_2|} \right).\end{aligned}$$

3.2.3 Electronics Rack and Neutron Source

Events were recorded using a Struck SIS3350 500 MHz 12-bit digitizer. The high voltage, gain, and offset were adjusted so that the raw baseline of the negative pulse, calculated as the average of the first 85 samples, was approximately 3965, and the largest amplitude events used about 80% of the dynamic range. Triggering was performed with an Ortec CF8000 constant fraction discriminator set low with respect to events used in the analysis.

A Thermo Electric MP 320 neutron generator was used to produce neutrons via a DD ($D+D \rightarrow {}^3\text{He}+n$; $E_n=2.5$ MeV) or DT ($D+T \rightarrow {}^4\text{He}+n$; $E_n=14.1$ MeV) reaction. This neutron generator is capable of producing 10^8 n/s for the DT reaction [33], though it was operated below maximum output for these measurements due to limitations resulting from the age of the generator, producing an event count rate of approximately 1000 cps for the DT measurements and 100 cps for the DD measurements.

3.3 Calculating Light Output and Quantifying Pulse Shape

3.3.1 Raw Pulse Processing

For a detector setup composed of an organic scintillator mounted to a photomultiplier tube and read out by a digitizer, each event in the detector produces a digitized pulse with samples

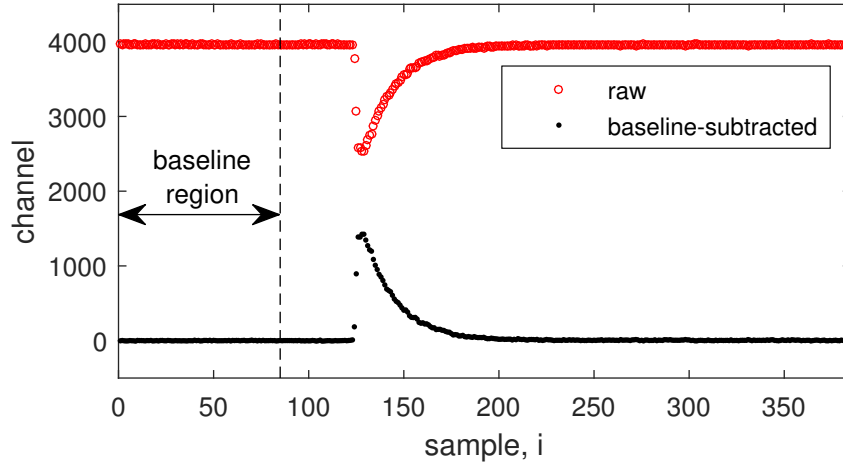


Figure 3.7: Raw and baseline-subtracted pulses from an event recorded from the mixed field produced by a DT neutron generator incident on an anthracene detector.

of amplitude x_i in baseline-subtracted digitizer channel units, where i is the sample number. For the measurements presented in this work, events were recorded using a Struck SIS3350 500 MHz 12-bit digitizer which records samples at 2 ns intervals across a range of 4096 channels. This digitizer was configured to measure 384 samples per event.

The raw pulse recorded by the digitizer is shown in Fig. 3.7. The baseline-subtracted pulse is calculated by subtracting each sample in the raw pulse from the baseline, which is calculated as the mean of the first 85 events in the raw pulse. If the samples in the raw pulse are y_i , then the baseline-subtracted samples x_i can be calculated as shown in Eq. (3.1), where $1 \leq i \leq 384$.

$$x_i = \frac{\sum_{j=1}^{85} y_j}{85} - y_i. \quad (3.1)$$

3.3.2 Calculating Light Output

For each event, the light output L is calculated as the sum of the baseline-subtracted pulse samples, as shown in Eq. (3.2). Before an energy calibration is performed, L is in integrated digitizer channel units (IDCU). In certain cases where it is important to make this clear, a subscript is added as L_{ch} :

$$L_{\text{ch}} = \sum_{i=1}^{i=384} x_i. \quad (3.2)$$

In order to express L in terms of energy, a calibration must be performed to convert the light output produced by each event from integrated digitizer channel units to energy units. One challenge in converting to energy units is that the digitized pulse is not a direct

measurement of energy deposited but rather of light produced by the scintillator. To account for this, L may be expressed in units of keVee or MeVee, where the *ee* appended to keV or MeV stands for *electron equivalent*. This corrects for a difference in light output per energy deposited produced by various particle types. Compared to electron recoil events, proton recoil events suffer significantly more quenching processes that reduce the amount of light produced for a given energy deposited. Thus, a 1 MeV electron recoil will produce more light output than a 1 MeV proton recoil. The units keVee and MeVee refer to the amount of light output produced by an electron recoil that deposited that amount of energy in keV or MeV. For example a 1 MeV electron recoil will produce 1 MeVee of light, while a 1 MeV proton recoil will produce less than 1 MeVee of light.

The calibration produces a calibration factor, C , in units of electron equivalent energy per integrated digitizer channel unit (keVee/IDCU). C is directly multiplied as shown in Eq. (3.3) to calculate L in electron equivalent energy units:

$$L = C \sum_{i=1}^{i=384} x_i. \quad (3.3)$$

In this work, the light output energy calibrations for all measurements were performed using a ^{137}Cs source producing monoenergetic gamma rays at $E_\gamma = 662$ keV. These gamma rays interact via Compton scatter, as described in Sec. 2.1.2, to produce Compton edge electron recoils of energy $E_{\text{CE}}=478$ keV. The position of the Compton edge in the light output spectrum is used for the light output energy calibration.

3.3.3 Calibrating Light Output

The calibration factor for converting the light output from L_{ch} in IDCU units to L in keVee or MeVee units is calculated as:

$$C = \frac{478 \text{ keVee}}{L_{478} \text{ IDCU}}. \quad (3.4)$$

Where L_{478} is the light output in integrated digitizer channel units of a Compton edge electron recoil at 478 keV. The position of the feature on the light output spectrum that corresponds to 478 keV was determined through an MCNP5 simulation to be $N_{478} = 0.74N_{\text{peak}}$, where N_{peak} is the number counts in the peak feature. This simulation is described in detail in App. A.

In order to locate the position of the feature corresponding to L_{478} on a measured light output distribution, a fit function was constructed that analyzes the smoothed light output spectrum and its differential. The smoothed spectrum was produced using the MATLAB function `smooth` that applies a moving average filter with a span of five samples. Figure 3.8 shows both of these spectra. In order to locate the peak feature in the smoothed light output spectrum, the fit function finds the numbered features on the smoothed differential spectrum with the following steps:

1. Find the maximum of the entire distribution.

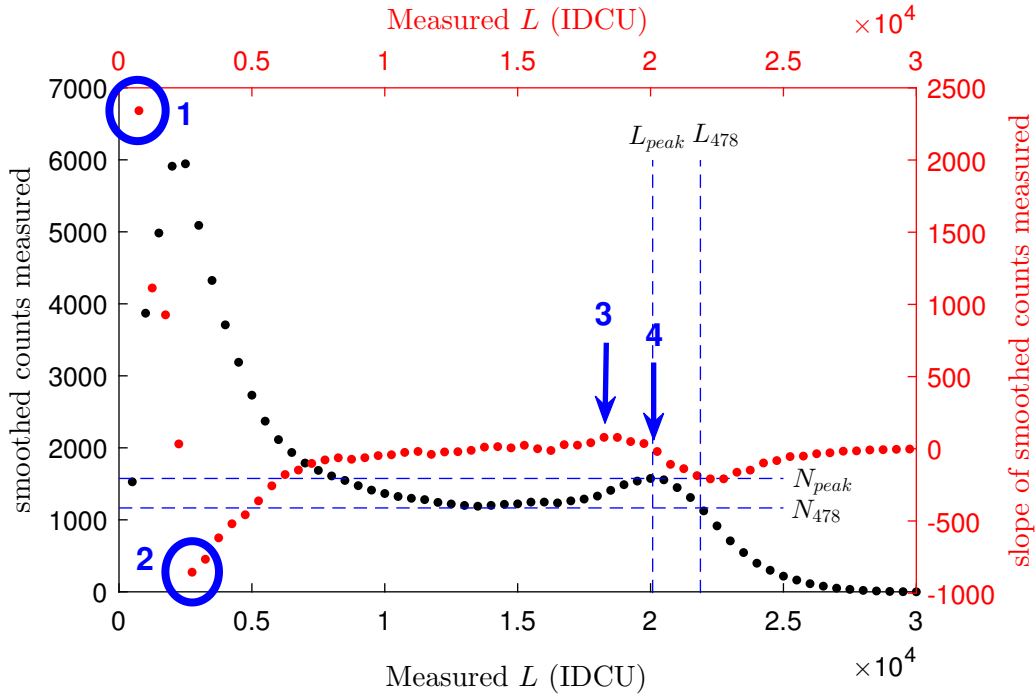


Figure 3.8: Distribution of smoothed counts and differential of smoothed counts as a function of light output for a measurement of ^{137}Cs on anthracene. Key features used by the fit function for performing the light output energy calibration are indicated.

2. Find the minimum of the distribution to the right of the maximum found in step 1.
3. Find the maximum of the distribution to the right of the minimum found in step 2.
4. Find the next zero-crossing point of the point after that. This corresponds to the peak feature to the left of the Compton edge.

The fit function then locates L_{478} on the smoothed light output spectrum. Working toward the right from the peak feature at $(L_{\text{peak}}, N_{\text{peak}})$, the fit function identifies the light output L_{478} that corresponds to a count number of $N_{478} = 0.74N_{\text{peak}}$, then calculates the calibration factor C as defined in Eq. (3.4).

3.3.4 Quantifying Pulse Shape

There are many ways of expressing the shape of an electronic pulse measured from a radiation interaction quantitatively. A simple technique for expressing the shape in a one-dimensional value, often called the “tail-to-total method,” is to calculate a pulse shape parameter S as the fraction of light in a defined delayed region of the pulse relative to the total light in the

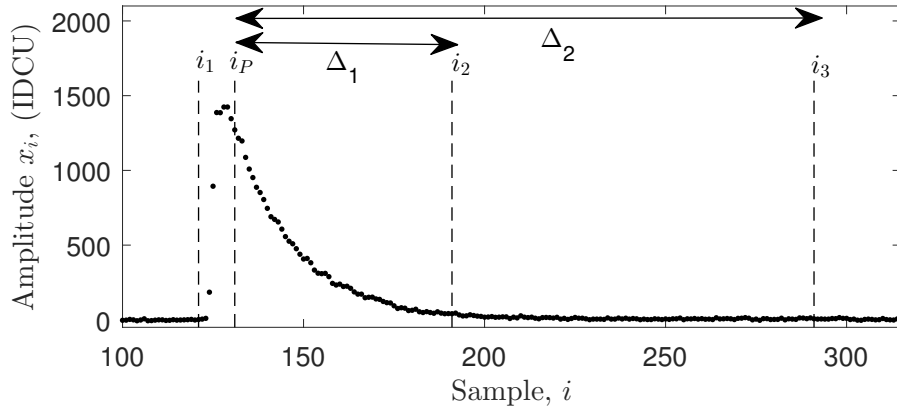


Figure 3.9: Baseline-subtracted pulse measured from a DT neutron event incident on anthracene. Samples i_1 , i_2 , i_3 , and i_P define regions relevant to calculating S .

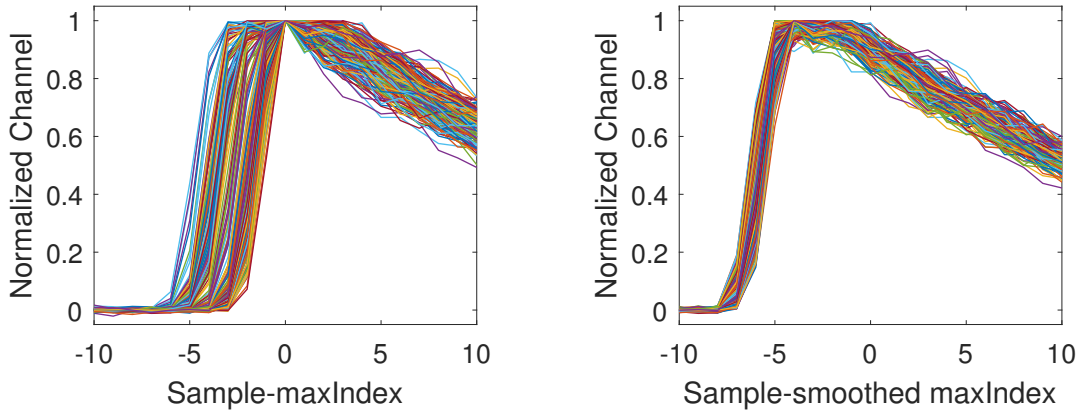
pulse:

$$S = \frac{\sum_{i_2}^{i_3} x_i}{\sum_{i_1}^{i_3} x_i}. \quad (3.5)$$

The samples i_1 , i_2 , and i_3 define the beginning of the pulse, the beginning of the delayed region, and the end of the pulse, respectively. They are calculated as $i_1 = i_P - 10$, $i_2 = i_P + \Delta_1$, and $i_3 = i_P + \Delta_2$, where i_P corresponds to a reference position. These values are shown for an example measured pulse in Fig. 3.9.

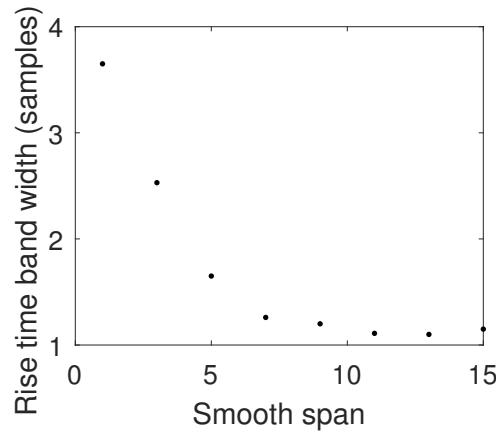
Due to fluctuations in photostatistics, the maximum index of the raw pulse varies in its position relative to the rise time of the pulse by up to ten samples between events. This is especially strong in anthracene, which has a slow decay time compared to the other measured materials. In order to position i_P at a consistent feature with respect to the rise time of the raw pulse, i_P corresponds to the peak of the baseline subtracted pulse after a smoothing filter is applied with a smoothing span of 11 samples. Figure 3.10 provides a visualization of raw pulses shifted to the maximum index as calculated without and with a smoothing filter to show that the smoothed maximum index better lines up the pulses. The smoothing filter is only used for determining i_P , not for calculating L and S via Eq. (3.3) and Eq. (3.5).

Δ_1 and Δ_2 are calculated separately for each material via an iterative process to maximize the separation of the S values for neutron and gamma-ray events. Δ_1 and Δ_2 vary across materials because the decay time and pulse shape characteristics differ across materials. For most crystals, this was performed for data measured from the mixed field produced by a DT neutron generator. For each combination of Δ_1 and Δ_2 values, the plots shown in Fig. 3.11 are produced. Figure 3.11a shows the density plot of L vs S values as measured on anthracene. Events in a given light output range, in this case between 2000 and 4000 keVee, are selected and a histogram of S values for those events is produced as shown in Fig. 3.11b. The lower peak in this distribution corresponds to gamma-ray events and the upper peak to neutron events. A double Gaussian fit function is applied to the data. The separation



(a) Raw pulses shifted to the maximum amplitude index of the saw pulse.

(b) Raw pulses shifted to the maximum amplitude index of the smoothed pulse (smoothspan = 11).



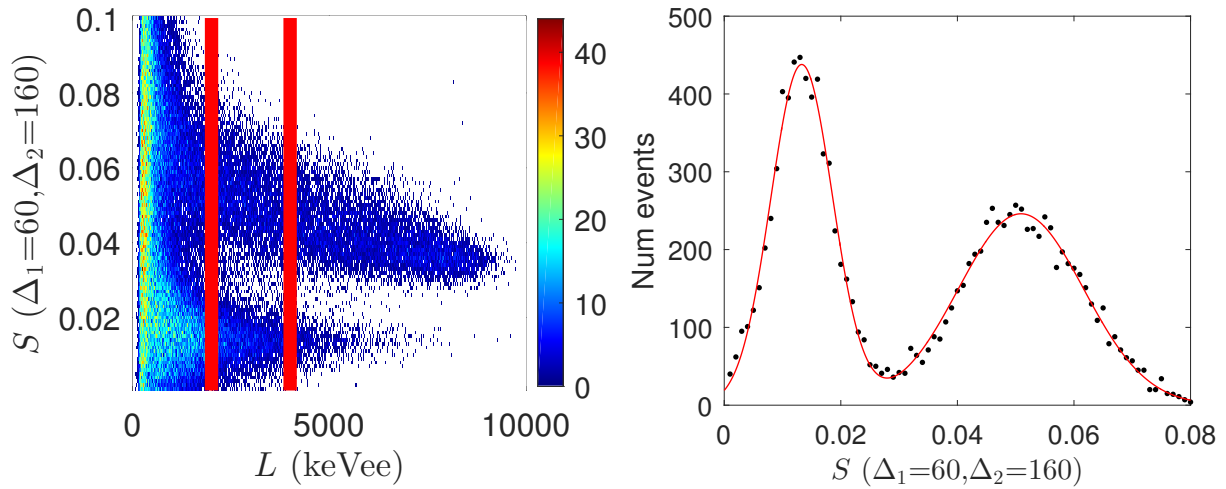
(c) Width of the rise time band vs. smoothing span.

Figure 3.10: Raw events from the mixed field produced by a DT neutron generator measured by an anthracene detector. Calculating the maximum index of the smoothed pulse rather than the raw pulse provides a method for consistently locating i_p with respect to the rise time.

between the neutron and gamma-ray distributions is calculated using the following figure of merit:

$$\text{FOM} = \frac{|\mu_1 - \mu_2|}{\sqrt{\text{FWHM}_1^2 + \text{FWHM}_2^2}},$$

where μ_1 is the centroid pulse shape parameter S for neutron events and μ_2 is the centroid pulse shape parameter S for gamma-ray events as found by the fit function. The FOM is calculated for a range of (Δ_1, Δ_2) values, as shown in Fig. 3.12. Higher FOM values indicate



(a) Density plot of L vs. S . Red lines indicate limits at 2000 and 4000 keVee.

(b) Histogram of S values for events with light output between 2000 and 4000 keVee. The red curve is an automated double Gaussian fit.

Figure 3.11: PSD distributions measured from the mixed field produced by a DT neutron generator on anthracene.

better separation between the neutron and gamma-ray ranges. Figure 3.12 shows that the best separation for events on anthracene from a DT generator in this light output range occurs for $(\Delta_1, \Delta_2) \approx (60, 160)$, so those values are chosen as standards for all anthracene measurements. The optimal (Δ_1, Δ_2) values may change for a given detector depending on what energy range you look in. For this work, the goal is not to achieve optimal pulse shape discrimination, but rather to develop a consistent and robust quantitative representation of the pulse shape, so using the same (Δ_1, Δ_2) for all light output ranges is acceptable. The (Δ_1, Δ_2) values used for all materials measured in this work are provided in Table 3.1.

	110	120	130	140	150	160	170	180	190	200
50	1.501321	1.559204	1.588645	1.622914	1.644084	1.657158	1.656942	1.654893	1.668666	1.661981
52	1.520557	1.576215	1.612801	1.644545	1.669757	1.673364	1.673255	1.672038	1.67592	1.677047
54	1.546923	1.598597	1.626232	1.653981	1.66844	1.690421	1.682981	1.675474	1.681104	1.677886
56	1.559606	1.596277	1.648194	1.664327	1.693445	1.687337	1.681423	1.679465	1.677751	1.679949
58	1.569456	1.612032	1.650744	1.692133	1.684984	1.690211	1.689965	1.685098	1.683536	1.686091
60	1.575859	1.635127	1.669721	1.701896	1.691901	1.709492	1.693819	1.693017	1.690283	1.68178
62	1.587801	1.658941	1.660035	1.692484	1.700079	1.709461	1.697643	1.686502	1.691576	1.6911
64	1.602646	1.651439	1.667527	1.698295	1.708926	1.715244	1.696977	1.687357	1.685391	1.675702
66	1.593197	1.638711	1.674205	1.697963	1.699132	1.70508	1.695239	1.677446	1.67217	1.667679
68	1.589109	1.646386	1.671105	1.70386	1.697579	1.699393	1.683534	1.66839		1.662172
70	1.594791	1.642576	1.678338	1.6988	1.691976	1.70302	1.672236	1.673519	1.656843	1.661526

Figure 3.12: Screenshot of *FOM* comparison in Microsoft Excel for *S* distributions calculated on anthracene for various values of Δ_1 (rows) and Δ_2 (columns).

Table 3.1: Δ_1 and Δ_2 values as used for calculating *S* for all PSD-capable materials measured in this work.

Detector	Δ_1	Δ_2
Anthracene	60	160
EJ309 Liquid	10	40
Stilbene	10	60
Stilbene Melt	16	70
Plastic	10	60
Pure DPAC	3	70
BB317	24	100
P-Terphenyl	6	60
DPAC-Stilbene (80:20)	7	50
BB-Stilbene (50:50)	15	65

Chapter 4

Investigating the Scintillation Anisotropy for Various Particle Types in Crystalline Anthracene

In order to study the anisotropy as produced by different interacting particle types, detailed measurements were made of neutron, gamma-ray, and muon interactions on an anthracene crystal. As described in Sec. 1.1, previous authors measured a directional dependence of the light output and pulse shape from interactions by alpha particles and proton recoils produced by neutron interactions. In order to contribute to the understanding of these systems, a new characterization has been performed on the directional dependence of proton recoil events from neutron interactions in anthracene. These measurements serve to augment and confirm similar measurements made previously at a range of neutron energies.

Thus far, no directional dependence has been observed in electron recoil events produced by gamma-ray interactions, but no quantitative measurements have been published to demonstrate this. The hypothesized mechanism of preferred directions of excitation transport described in Sec. 2.2.4 may produce a smaller but non-zero directional dependence for electron recoil events produced by gamma-ray interactions. Thus, a characterization has been performed on the directional response to electron recoil events produced by gamma-ray Compton scatter interactions in anthracene. Anthracene was chosen for this study because it has the largest magnitude of pulse shape anisotropy of the organic crystal scintillators that have been measured in the past [7]. If there is a small anisotropy in the gamma-ray response, it is more likely that a measurement system with a given sensitivity level could observe it in anthracene than in other materials because the effect is larger in anthracene. These measurements will serve either to demonstrate that there is a directional dependence and measure its magnitude, or, if no effect is observed, to set an upper bound on its magnitude.

Heavy charged particle recoils differ from electron recoils in that they deposit their energy with a high stopping power dE/dx in a straight path. Brooks hypothesized that the lack of anisotropy in electron recoil events is due to their non-straight path [7], but it is also possible that it is due to their low dE/dx . Energetic cosmogenic muons are minimum

ionizing particles that, like electrons, deposit energy with low dE/dx , but, like protons, travel in a straight path. The differences between these three particle types is described in greater detail in Sec. 2.1. Measurements of cosmic muons were therefore performed to test for a directional dependence. The presence or absence of a directional dependence in cosmic muon interactions will probe whether a high stopping power dE/dx or straight trajectory is necessary for producing a directional dependence.

4.1 Neutron Measurements in Anthracene

In order to confirm the directional dependence that has been documented in anthracene [7, 8, 9, 10], proton recoil events from neutron interactions have been measured. The directional dependence is characterized by measuring the \hat{L} and \hat{S} , the expected L and S values produced by a proton recoil, as a function of the recoil direction for protons of a fixed energy. The measurements presented in this paper have been made with digital pulse acquisition and processing, allowing for detailed offline analysis.

4.1.1 Experimental Setup

The anthracene crystal used in these measurements is an older sample with unknown history and considerable wear. Several minor cracks are visible within the crystal and the surface has been polished numerous times. The crystal was produced using a melt growth technique, so it is unlikely to be to a perfect monocrystal. The sample is a cylinder approximately 1.9 cm tall and 2.5 cm diameter. The arbitrary set of axes was maintained for measurements with all three particle types on this anthracene sample so that the (θ, ϕ) coordinates are consistent.

In order to characterize the response of anthracene to proton recoil events at different directions within the crystal, the energy and direction of the proton recoil must be known. This was accomplished by selecting full energy proton recoil events produced by monoenergetic neutrons, fixing the proton recoil energy as $E_{\text{recoil}} \approx E_n$ and the proton recoil direction as that of the incident neutron. The physics supporting this constraint is discussed in Sec. 2.1.1. In order to change the direction of the proton recoil in the crystal axes, the anthracene crystal was rotated via the rotational stage described in Sec. 3.2.2 to change its orientation with respect to the incident neutron direction. The anthracene crystal was approximately 150 cm away from the neutron generator, controlling the incident angle of the neutrons on the detector to within 2° .

Measurements were made of DT neutrons at 14.1 MeV and DD neutrons at 2.5 MeV produced by a neutron generator described in Sec. 3.2.3. For the DT measurements, 76 proton recoil directions were chosen to measure evenly across a hemisphere worth of directions. For the DD measurements, which are limited by lower flux produced by the neutron generator, 34 evenly distributed proton recoil directions were chosen.

4.1.2 Data Analysis

For each measurement, the following steps were taken to determine \hat{L} and \hat{S} , the expected L and S values for a full-energy proton recoil at the angle of interest.

1. Neutron selection: An L vs. S distribution was produced, as shown in Fig. 4.1. In this figure, the upper band with higher S values is populated primarily by neutron events, and the lower band with lower S values is populated primarily by gamma-ray events, as described in Sec. 2.2.3. The lines indicate the light output threshold and cutoff for separating the neutron and gamma-ray events. The light output threshold was set at 3000 keVee for DT measurements and 300 keVee for DD measurements. Events above and to the right of the lines are selected for further analysis.
2. Neutron light output spectrum fit: To calculate the light output at the spectrum endpoint, the energy spectrum of the selected events is fitted to the following function:

$$f(L) = \frac{mL + b}{2} \left[1 - \operatorname{erf} \left(\frac{L - \hat{L}}{\sigma\sqrt{2}} \right) \right] - \frac{m\sigma}{\sqrt{2\pi}} e^{-\frac{(L - \hat{L})^2}{2\sigma^2}}. \quad (4.1)$$

This function represents a sloped distribution with a hard cutoff convolved with a Gaussian resolution function. The line with negative slope m and y-intercept b serves as a first order approximation to incorporate light output nonlinearity in the conversion of proton recoil energy to light output in the upper end of the light output spectrum. The hard cutoff represents the upper limit of the proton recoil energy in a monoenergetic neutron-proton scattering interaction, and the Gaussian term accounts for detector resolution. The value \hat{L} is the expected light output from a full energy proton recoil event, and σ is the fitted resolution of the detector. A light output spectrum, along with its best-fit function, is shown in Fig. 4.2.

3. Full energy event selection: Events within the range $\hat{L} \pm \sigma$ are selected as full-energy proton recoils. For these measurements, this selection widens the range of proton recoil directions to events within 7° of the forward direction.
4. Pulse shape distribution fit: A distribution of the S value for full energy proton recoil events is produced. A Gaussian fit is applied to this distribution to calculate the centroid tail-to-total value \hat{S} as shown in Fig. 4.3.

4.1.3 Measurement Results

For each measurement at a unique proton recoil direction, the \hat{L} and \hat{S} values for full energy proton recoils are calculated. Figure 4.4 shows the \hat{L} and \hat{S} values produced by 14.1 MeV proton recoils produced by a DT neutron generator at 76 directions in anthracene. The distributions show smooth transitions between maximum and minimum regions.

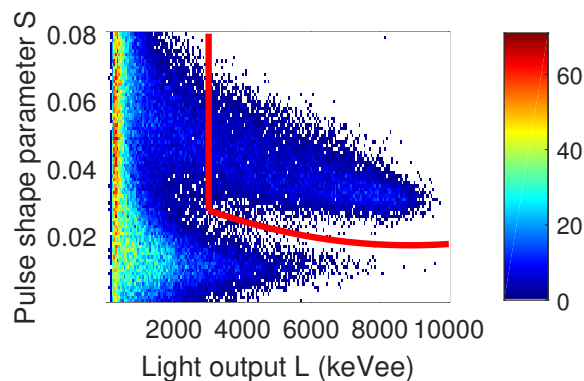


Figure 4.1: Density plot of L vs. S for the mixed radiation field produced by a DT neutron generator incident on anthracene at $(\theta, \phi) = (8.3^\circ, 131.7^\circ)$. The lines are drawn to show the cutoff point for selecting neutron events above 3000 keVee.

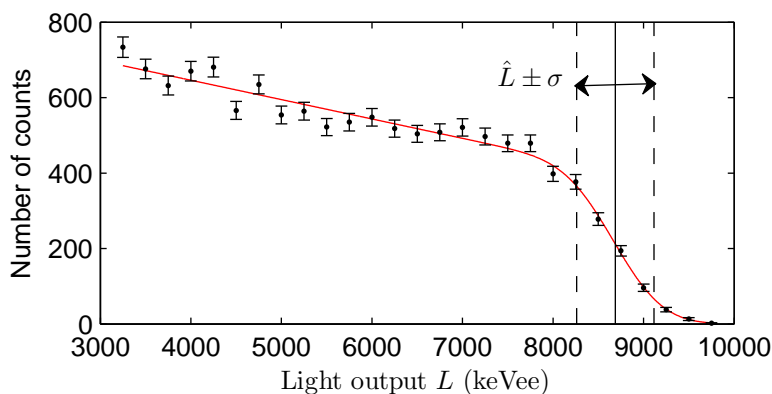


Figure 4.2: Light output spectrum for neutron events above 3000 keVee produced by a DT neutron generator incident on anthracene at $(\theta, \phi) = (8.3^\circ, 131.7^\circ)$. Points are experimental data, the line is the applied fit function, and the light output range $\hat{L} \pm \sigma$ in which interactions are selected as full energy interactions is indicated.

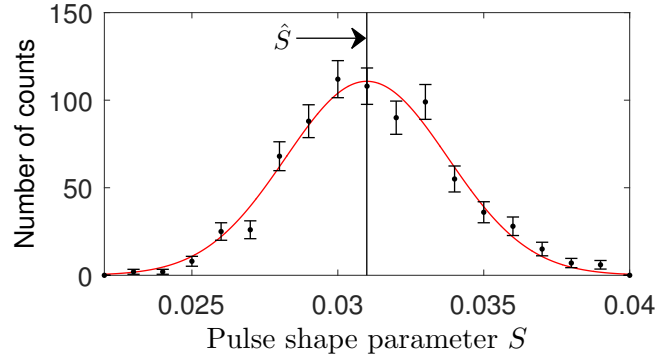


Figure 4.3: S distribution for neutron events with L within $\hat{L} \pm \sigma$ produced by a DT neutron generator incident on anthracene at $(\theta, \phi) = (8.3^\circ, 131.7^\circ)$. Points are experimental data, the line is the applied Gaussian fit function.

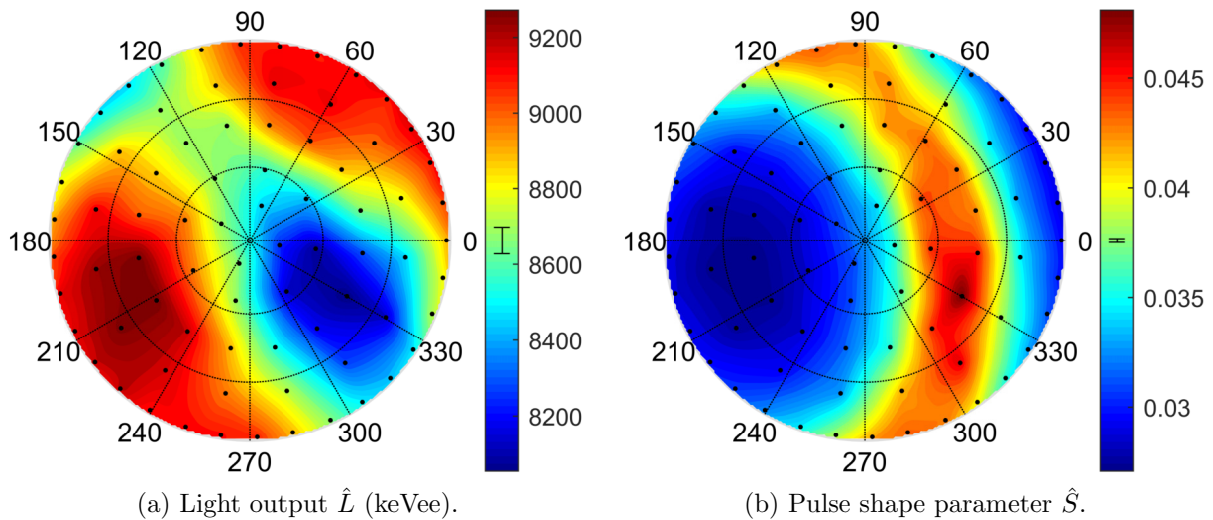


Figure 4.4: Response of anthracene crystal at various recoil directions to 14.1 MeV protons. Points indicate measurements and the gradients represent a smooth interpolation between measurements. Length of vertical bar on colorbar indicates average $\pm\sigma$ statistical error. The 2D distribution represents a hemisphere worth of 3D directions in spherical coordinates with ϕ increasing counter-clockwise and θ increasing radially outward as $r = \sqrt{1 - \cos\theta}$.

Figure 4.5 shows the same distributions for 2.5 MeV proton recoils produced by a DD neutron generator at 34 directions in anthracene. Although there is less resolution in the DD distributions due to fewer measurements, less data per measurement, and larger uncertainties, Fig. 4.4 and Fig. 4.5 demonstrate that the maximum, minimum and saddle point features in the \hat{L} and \hat{S} distributions occur at the same proton recoil directions for 14 MeV and 2.5 MeV proton recoils.

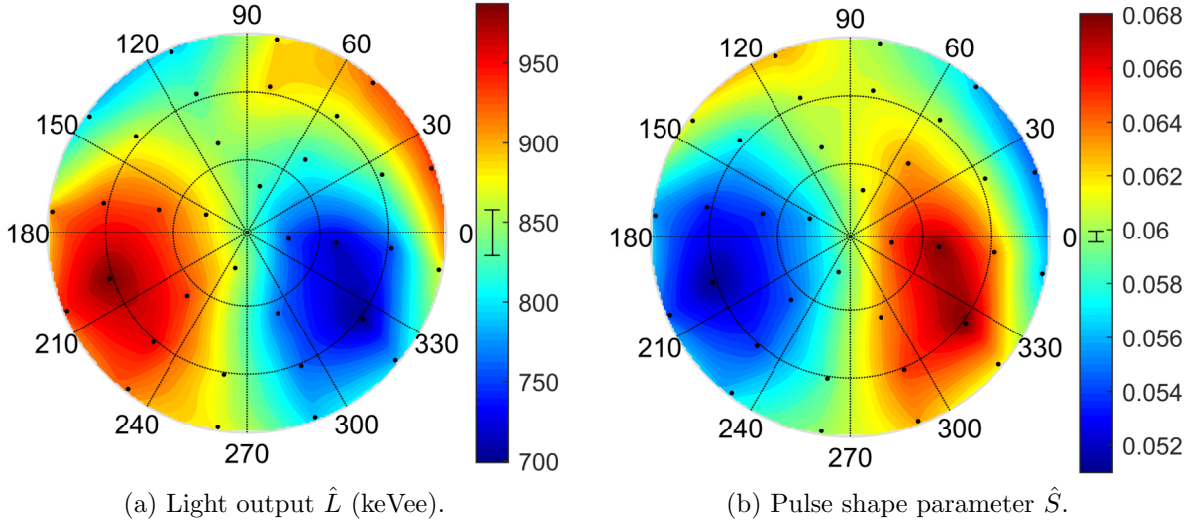


Figure 4.5: Response of anthracene crystal at various recoil directions to 2.5 MeV protons.

To quantify the magnitude of the anisotropy at each energy, the ratio between the maximum and minimum observed values is calculated:

$$A_L = \frac{\hat{L}_{\max}}{\hat{L}_{\min}}, \text{ and} \quad A_S = \frac{\hat{S}_{\max}}{\hat{S}_{\min}}.$$

These ratios for 14.1 MeV and 2.5 MeV proton recoil events in anthracene are shown in Table 4.1. The errors are statistical only and are propagated from the errors in the calculation of \hat{L} and \hat{S} as found by the fit function. These measurements demonstrate that the magnitude of the light output anisotropy is greater at lower proton recoil energies, while the magnitude of the pulse shape anisotropy is greater at higher proton recoil energies.

Table 4.1: Magnitude of Anisotropy Measured in Expected Light Output \hat{L} and Pulse Shape Parameter \hat{S} Produced by Proton Recoil Events in Anthracene

E_{recoil}	14.1 MeV	2.5 MeV
A_L	1.155 ± 0.006	1.383 ± 0.023
A_S	1.798 ± 0.006	1.307 ± 0.005

These measurements of the magnitude of change in the light output agree with past measurements made by others and described in Sec. 1.1.2, as shown in Fig. 4.6. All measurements are consistent with the trend that the magnitude of change in the light output decreases as the proton recoil energy increases.

It should be noted that systematic limitations exist in this measurement system that bias A_L and A_S toward smaller values. By selecting proton recoils traveling in a range of directions and traversing an imperfect crystal structure, the \hat{L} and \hat{S} measurements at a

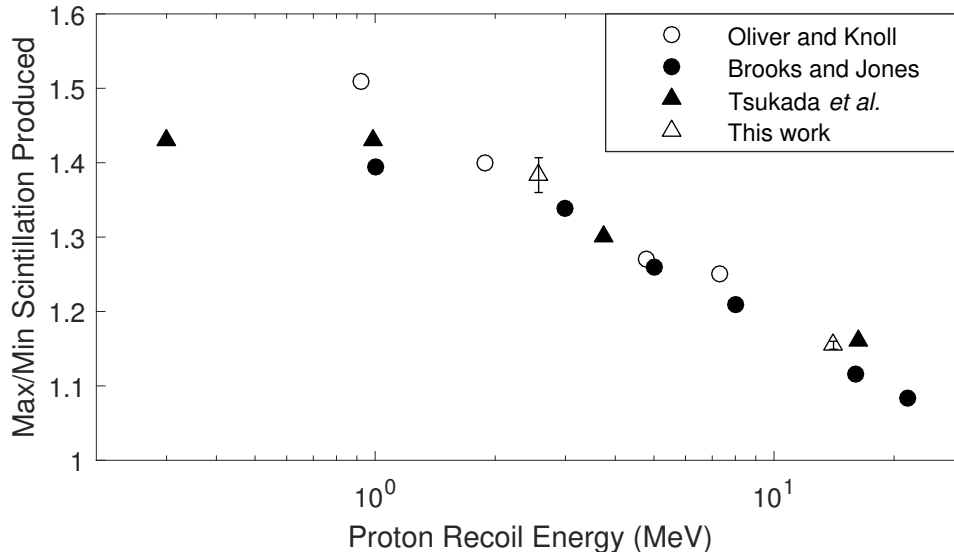


Figure 4.6: Magnitude of change in light output produced by proton recoil events in anthracene as a function of proton energy [7, 8, 10].

given proton recoil direction represent average \hat{L} and \hat{S} values for proton recoils within a small range of directions with respect to the crystal axes. It follows, then, that the true maximum value of \hat{L} or \hat{S} for a proton recoil traveling in the crystal structure may be larger than is measured, and the true minimum value may be smaller than is measured, pushing the measured A_L and A_S toward smaller magnitudes than their true values.

It is also possible that A_L and A_S could be biased toward larger values due to statistical fluctuations. For example, statistical fluctuations may push the maximum value or measurements near the maximum value to be larger than the true maximum value. Similarly, the minimum measured value may be lower than the true minimum value due to statistical fluctuations.

4.1.4 Handling Statistical Error

Another metric for quantifying the anisotropy is evaluating the additional variability that the directional dependence introduces into the measurement of \hat{L} and \hat{S} in a situation where the proton recoil direction is unknown and the proton recoil is equally likely to travel in any direction. These measurements can be used to estimate this variability for proton recoil events at either 14 MeV or 2.5 MeV. A metric σ_{anis} is related to the observed standard deviation σ_{obs} of measured \hat{L} and \hat{S} values at a given energy. The contribution from statistical variance is subtracted in quadrature, e.g.

$$\sigma_{\text{anis}} = \sqrt{\sigma_{\text{obs}}^2 - \sigma_{\text{stat}}^2},$$

where σ_{stat}^2 is the average statistical variance from the set of measurements at different recoil directions. The relevant quantities for each group of datasets are given in Table 4.2, normalized to the average measured value μ .

Table 4.2: Variability in pulse shape and light output in proton recoil events in anthracene.

	E_{recoil}	14 MeV	2.5 MeV
\hat{L}	$\sigma_{\text{obs}} / \mu$	3.7%	8.6%
	$\sigma_{\text{stat}} / \mu$	0.4%	2.2%
	$\sigma_{\text{anis}} / \mu$	3.7%	8.3%
\hat{S}	$\sigma_{\text{obs}} / \mu$	16.8%	7.2%
	$\sigma_{\text{stat}} / \mu$	0.3%	0.4%
	$\sigma_{\text{anis}} / \mu$	16.8%	7.2%

Strictly speaking, σ_{anis} includes both the anisotropy effect and other sources of systematic error, some of which have already been mentioned. These systematic errors include but are not limited to the width of the proton recoil direction selection window due to the physical size of the detector and the range of energies selected at the endpoint, the possibility of several low energy interactions summing to a full energy event, the imperfect crystal structure that exists in the sample, and the approximation of the fit function to represent the distribution. Additionally, no temperature correction, described for the gamma-ray measurements in Sec. 4.2.3, was performed on the neutron measurements because such data was not available at the time of the measurement. If the neutron measurements were to experience the same temperature swing that was observed in the directional gamma-ray measurements, it is expected that \hat{L} and \hat{S} would be subject to a temperature variability of $\sigma_{\text{temp}} / \mu$ of 1.3% and 0.8%, respectively. If σ_{anis} is recalculated to account for this temperature variability as $\sigma_{\text{anis}} = \sqrt{\sigma_{\text{obs}}^2 - \sigma_{\text{stat}}^2 - \sigma_{\text{temp}}^2}$, the only value for $\sigma_{\text{anis}} / \mu$ that changes more than 0.1% is that for \hat{L} at 14 MeV, which is reduced from 3.7% to 3.5%. Thus, while the availability of temperature data would have been desired, the variability in \hat{L} and \hat{S} introduced by temperature effects is expected to be small compared to the variability due to the anisotropy effect for proton recoil events. Given the qualitative features in the angular distribution of \hat{L} and \hat{S} , it appears that σ_{anis} for both \hat{L} and \hat{S} are dominated by the anisotropy effect in proton recoil interactions. Other explanations for the observed directional dependence have been considered, such as magnetic field effects on the PMT. However, any such external effect must be minimal compared to the internal effect in the crystal because this anisotropy is not observed for gamma-ray interactions in crystalline materials, as will be demonstrated in Sec. 4.2. Additionally, plastic and liquid scintillators do not exhibit a directional response, as stated by others [18, p. 261] and confirmed via measurements discussed in Sec. 5.

4.1.5 Inferring Anthracene Crystal Axes Directions

According to measurements made by previous groups, the proton recoil direction that produces maximum light output in anthracene is along the c' -axis, defined as the direction perpendicular to the ab -plane of the crystal, and the direction that produces minimum light output is along the b -axis [7, 9]. This allows for the crystal axes of the anthracene sample measured in this work to be inferred. According to Figs. 4.4 and 4.5, the b -axis is at approximately $(\theta, \phi) = (40^\circ, 330^\circ)$ and the c' -axis is at approximately $(\theta, \phi) = (60^\circ, 200^\circ)$. These directions make an angle of approximately 90° , as the b and c' -axes should. This puts the a axis at approximately $(\theta, \phi) = (65^\circ, 95^\circ)$. These measurements also confirm Tsukada and Kikuchi's findings that the saddle point in the light output distribution occurs in the ac plane about 30° from the a -axis [9].

4.2 Gamma-Ray Measurements in Anthracene

So far, no directional dependence has been documented in gamma-ray interactions in organic crystal scintillator detectors. Brooks and Jones' characterization of the heavy charged particle scintillation anisotropy noted that electron recoil events produced by gamma-ray interactions are not subject to a directional dependence [7], however, this was not quantified and no measurement details were provided.

Compton electrons do not maintain a unique direction as they slow down as they undergo multiple large-angle scattering events. Brooks and Jones hypothesized that this non-straight path is responsible for the lack of directional dependence in Compton electrons [7]. The lack of anisotropy may also be due to the low dE/dx deposited by electron recoil events. Considering the hypothesis that directionally dependent kinetic processes produce the directional dependence in heavy charged particle interactions, as described in Sec. 2.2.4, the excitation density produced by gamma-ray events may be so low that directionally dependent changes are not significant compared to the overall density. However, it is also possible that the effect is just much smaller for gamma-ray events than for neutron events, and a smaller anisotropy may be observable with a sensitive measurement. In order to investigate this, electron recoils produced by gamma-ray interactions have been measured at different directions in anthracene.

4.2.1 Experimental Setup

Measurements were made with a ^{137}Cs source that was placed 97 cm from the detector, producing a count rate of approximately 30 cps and controlling the incident gamma-ray direction to within 3° . The 662 keV gamma ray from ^{137}Cs produces a Compton edge electron recoil with energy $E_{e^-} = 478$ keV. In order to control the energy and initial direction of electron recoils produced in anthracene, Compton edge electron events were selected. As described in Sec. 2.1.2, these electrons' initial direction is in the same direction as the incident

gamma-ray, though their path is not straight as they scatter at wide angles as they deposit energy.

The same rotational stage was used for the gamma-ray measurements as was described in Sec. 3.2.2 for the neutron measurements. This provided the capability to change the initial direction of the electron recoil in the crystal axes by rotating the anthracene crystal with respect to the incident gamma-ray direction. Measurements were made at the same 76 recoil directions in the anthracene crystal as were measured in the DT neutron measurements.

4.2.2 Data Analysis

For each measurement, the following three steps were taken to calculate \hat{L} and \hat{S} , the expected L and S values for a 478 keV electron recoil generated at the angle of interest.

1. Light output spectrum fit: A light output spectrum of all events in a single measurement is shown in Fig. 4.7. The light output corresponding to N_{478} was recorded as \hat{L} using the method described in Sec. 3.3.3.
2. Compton edge event selection: Events within the range $\hat{L} \pm \sigma$, where σ is the light output resolution, were selected as Compton edge electron recoils. This widened the range of electron recoil directions to events within half-angle $\rho = 18.3^\circ$ around the forward direction.
3. Pulse shape distribution fit: A distribution of the S value for Compton edge electron recoil events was produced. A Gaussian fit was applied to this distribution to estimate the expected pulse shape parameter \hat{S} as shown in Fig. 4.8.

In order to estimate the statistical error in the calculation of \hat{L} in each measurement, a bootstrapping method was applied. One hundred light output spectra were generated based on Poisson fluctuations about the light output spectrum from each measurement, simulating a resampling of the data. The \hat{L} value was calculated for each bootstrap-generated spectrum, and the standard deviation in the 100 \hat{L} values served as an estimate for the statistical error in the measurement of \hat{L} .

4.2.3 Temperature Dependence

The light output and pulse shapes produced in anthracene have a temperature dependence that proved to be the largest source of systematic bias in the gamma-ray measurements. Therefore, the dependence was characterized and a correction was applied. A separate set of 10-min long measurements of a ^{137}Cs source at a fixed angle with respect to the detector were taken over six days as the temperature in the lab varied with the weather. The \hat{L} and \hat{S} values were calculated for each measurement and plotted vs. temperature as shown in Fig. 4.9 and Fig. 4.10. Linear fits to these data were used to correct the \hat{L} and \hat{S} values in the directional measurements to 25°C .

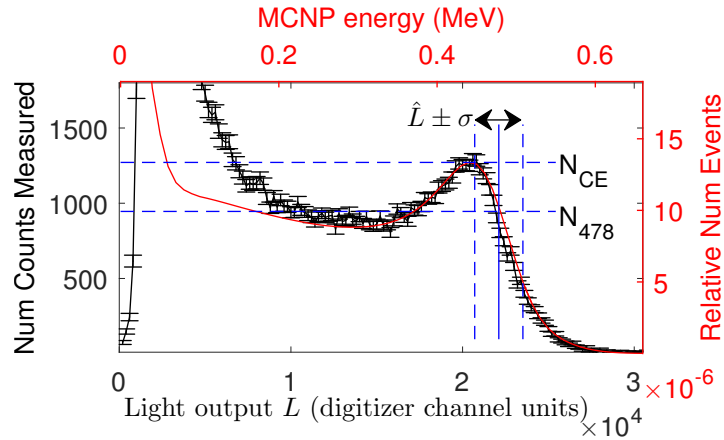


Figure 4.7: Light output spectrum for ^{137}Cs gamma-ray events incident on anthracene at $(\theta, \phi) = (50^\circ, 178^\circ)$. The solid curve, upper and right axes correspond to an MCNP5 simulation. The data points, lower and left axes correspond to a measurement. Dashed lines indicate N_{478} and N_{CE} as found in the fit function, which produce a final \hat{L} value for the light output in summed digitizer channel units of a 478 keV electron recoil event.

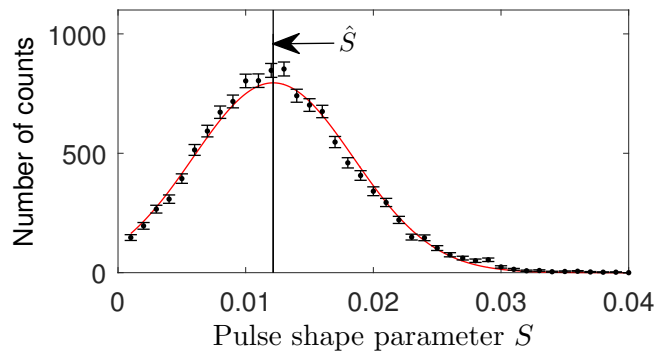


Figure 4.8: Distribution of S values for events with light output in the range $\hat{L} \pm \sigma$ produced by ^{137}Cs gamma rays incident on anthracene at $(\theta, \phi) = (50^\circ, 178^\circ)$. Points are experimental data and the curve is the applied Gaussian fit function.

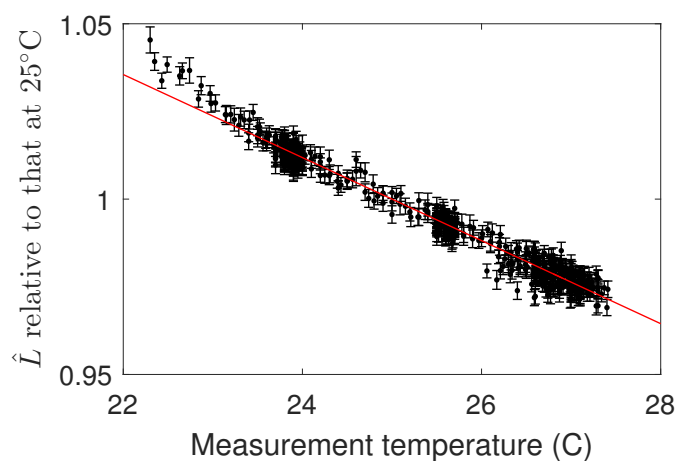


Figure 4.9: \hat{L} produced by a ^{137}Cs source at a fixed position at temperatures 22-28°C relative to that at 25°C.

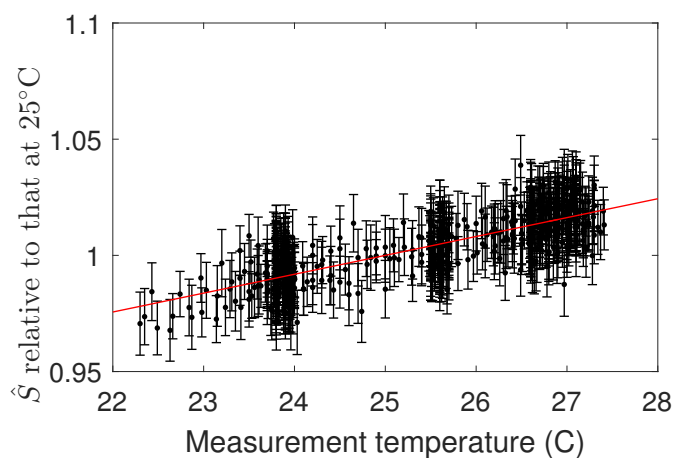


Figure 4.10: \hat{S} produced by a ^{137}Cs source at a fixed position at temperatures 22-28°C relative to that at 25°C.

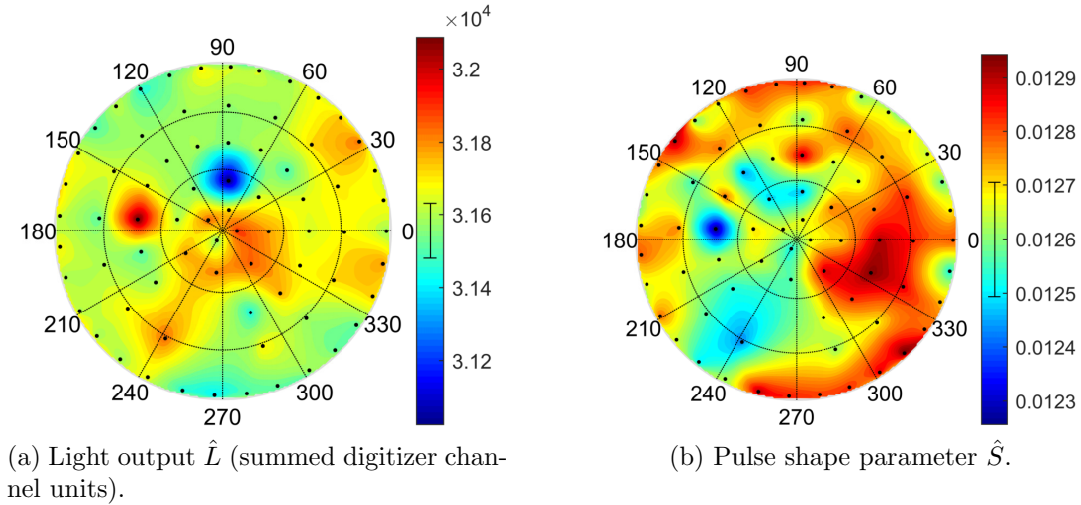


Figure 4.11: Response of anthracene crystal at various recoil directions for 478 keV electron recoils. See Fig. 4.4 caption for a detailed explanation of the anisotropy plots.

4.2.4 Measurement Results

Figure 4.11 shows the \hat{L} and \hat{S} values measured for 478 keV electron recoil events in anthracene at different electron recoil directions. The length of the line on the colorbar is the average statistical uncertainty in the measurement. Three measurements were omitted in which the motor system was between the source and the detector, causing considerably more environmental scattering and producing outlying values for \hat{L} and \hat{S} .

Although there are variations in these measurements greater than the statistical uncertainties, these distributions do not show the same qualitative features observed in the proton recoil measurements shown in Sec. 4.1.3. Features observed in the proton recoil measurements include one maximum region and one minimum region over a hemisphere of angle space with smooth transitions between them. Since the variation in the electron recoil measurements does not show these features, other systematic effects are thought to be dominating the observed directional dependence. Thus, it is concluded via qualitative observations that no anisotropy effect as seen for neutron interactions is present for gamma-ray interactions in anthracene.

4.2.5 Measurement Variability

Following the method explained in Sec. 4.1.2, Table 4.3 shows the relative standard deviations due to statistical uncertainty and other effects. Compared to the neutron measurements in which it was concluded that the anisotropy was the dominant effect in the variability of \hat{L} and \hat{S} , the qualitative features on the angular distributions of \hat{L} and \hat{S} indicate that the variability in the gamma-ray measurements is dominated by sources of bias and not an anisotropy. For that reason, this variability will be named σ_{other} . Several sources of bias

exist in these measurements. First, as the rotational stage changes its position, the position of the detector relative to the source and environment change, so the scattering environment differs. This may be significant for a gamma-ray source among the high-Z materials in the laboratory equipment. Second, the temperature correction is not a perfect method because the temperature sensor is outside of the detector and provides a measurement of the room temperature rather than the temperature in the crystal. Third, the light output window in the gamma-ray measurements produces a wider selection of recoil angles than in the neutron measurements.

Table 4.3: Variability in Pulse Shape and Light Output in Electron Recoil Events in Anthracene.

	E_{recoil}	0.478 MeV
\hat{L}	σ_{obs}/μ	0.5%
	σ_{stat}/μ	0.3%
	$\sigma_{\text{other}}/\mu$	0.4%
\hat{S}	σ_{obs}/μ	1.1%
	σ_{stat}/μ	0.8%
	$\sigma_{\text{other}}/\mu$	0.7%

However, if a conservative assumption is made that the anisotropy is the dominating effect, an upper limit on the magnitude of the anisotropy from 478 keV electron recoils may be approximated as σ_{other} . Even under this assumption, the anisotropy effect in electron recoil events is still less than one tenth of that for the proton recoil interactions (cf. Table 4.1).

4.3 Muon Measurements in Anthracene

As demonstrated in the previous sections, a directional dependence in anthracene has been observed in heavy charged particle interactions but not in electron recoil events. Two reasons have been hypothesized as being responsible for the lack of directional dependence in electron recoil events. First, Brooks attributed this lack of anisotropy to the non-straight path that electrons follow as they slow down due to the large-angle scattering that they undergo [7]. Electrons may not actually populate a directionally dependent excitation distribution, and it is possible that an electron recoil event, were it to travel in a straight path, could be subject to a directional dependence, but the non-straight path traveled by the electron washes out the effect. Second, electrons deposit their energy with a much lower dE/dx than heavy charged particles, producing a lower excitation density. Changes in the excitation density due to directional transport may be on too small a scale compared to the overall density to affect the relative rates of kinetic processes for the electron recoil.

In order to test whether the lack of directional dependence from the electron recoil is due to its low dE/dx or due to its non-straight path, cosmic muon events were measured. A muon in an elementary particle similar to an electron but with a mass of $105.7 \text{ MeV}/c^2$.

Like electrons, muons interact with a much lower dE/dx than heavy charged particles. In anthracene, muons deposit approximately 2.4 MeV/cm [34]. This is very close to the dE/dx deposited by a 478 keV electron of 2.5 MeV/cm, and much less than the 166.7 MeV/cm deposited by a 2.5 MeV proton recoil [35]. However, due to their large mass compared to the electrons in the medium in which they are interacting, muons are not subject to large-angle scattering and thus travel in a quasi-straight path. Additional information on the physics of muon interactions is provided in Sec. 2.1.3.

Since muons travel with lower dE/dx like the electron recoil, but in a quasi-straight path like the proton recoil, the presence or lack of directional dependence in muon interactions will provide information on whether a directional dependence requires that a particle interact with high dE/dx or in a straight path. The goal of these measurements is to measure the anisotropy present in muon events in anthracene, or if no anisotropy is observed, set an upper bound on its magnitude.

As described in Sec. 2.1.3, the energy deposited by a muon in an organic scintillator is proportional to the path length that the muon travels in the detector, so the deposited energy spectrum will be equal to the path length distribution multiplied by a constant factor. If there were a light output anisotropy in muon interactions in anthracene, it is expected that muons traveling at different angles would produce a different light output per energy deposited. Thus, the light output spectra produced by muons traveling at different directions would be equal to the path length distribution multiplied by different constant factors, and any features in those spectra would be shifted to different light output values. This constrains the measurements to arrangements that have the same path length distributions of muon trajectories through the detector.

4.3.1 Experimental Setup

Figure 4.12 shows the detectors used in this measurement. The rectangular blocks are EJ200 plastic scintillator detectors, and the cylinder is the anthracene crystal. Only events that exceeded the trigger threshold in all three detectors were used in order to select muons that traveled within a set angle ρ from the vertical direction through the anthracene. As the distance between the anthracene and the plastic blocks is increased, the angle ρ decreases to select muons traveling within a narrower range of angles in the anthracene, and the count rate decreases. The distance was chosen so that ρ was comparable to the range of proton recoil directions accepted in the neutron measurements. Each plastic block was placed 67 cm away from the anthracene detector, limiting the muon directions to within the half-angle $\rho = 9.1^\circ$ of the vertical direction.

In order to investigate muon interactions with paths along different directions within the anthracene crystal axes, measurements were taken with the crystal at different orientations with respect to a vertical muon trajectory. Due to the requirement that the geometry of the system be identical in the measurements in order to preserve the path length distribution, only angles at which the height axis of the crystal was perpendicular to the vertical muon path, as shown in Fig. 4.12, were candidates for the muon measurements. Two such directions

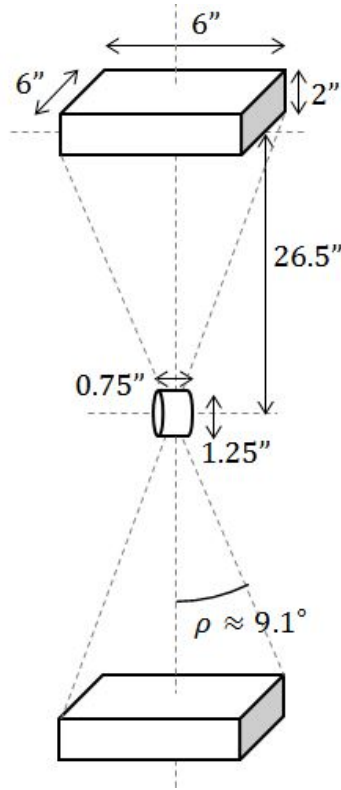


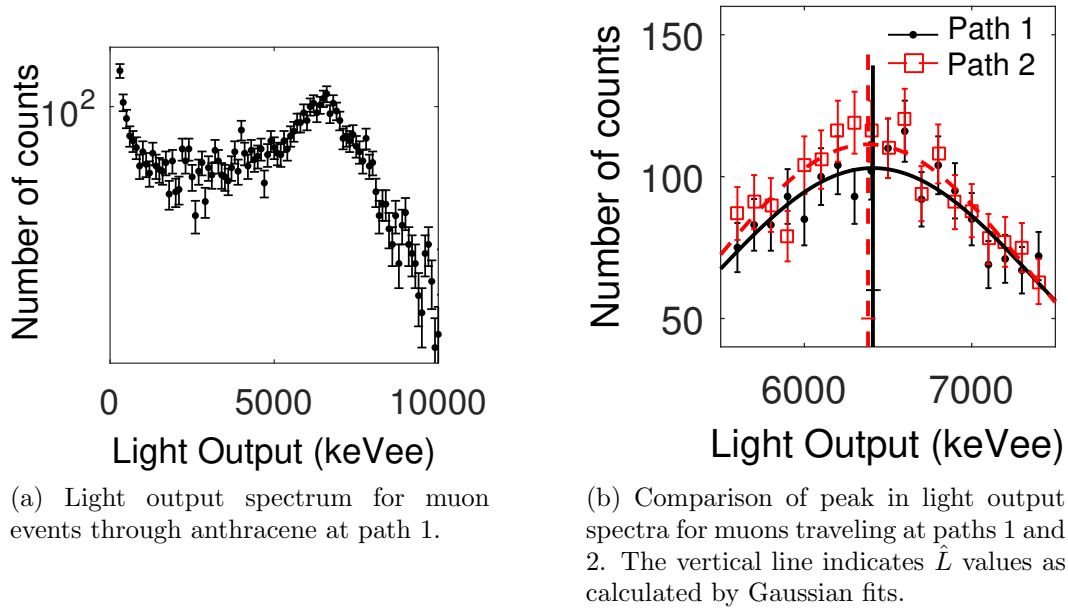
Figure 4.12: Cartoon of experimental setup for muon measurements with anthracene detector (not to scale).

were chosen and will be referred to as directions 1 and 2. Direction 1 was selected at $(\theta, \phi) = (90^\circ, 68.7^\circ)$, and direction 2 was at $(\theta, \phi) = (90^\circ, 158.7^\circ)$. Each measurement was taken for 20 days, producing approximately 2300 muon events in each measurement.

An assumption has been made that any anisotropy that would exist in the light output and pulse shape produced by muon interactions would follow the same crystal axes as the anisotropy from proton recoil events. Although these two interaction directions are not those of greatest difference in light output and pulse shape from the neutron measurements, there was still a significant difference in the light output and pulse shape at these two angles from 14 MeV and 2.5 MeV proton recoils, as listed in Table 4.4.

4.3.2 Data Analysis

In order to evaluate whether there is a significant difference in the light output and pulse shapes produced by muon events at directions 1 and 2, the expected light output \hat{L} and pulse shape parameter \hat{S} for events at the peak feature in the light output spectrum were calculated by following these three steps:



(a) Light output spectrum for muon events through anthracene at path 1.

(b) Comparison of peak in light output spectra for muons traveling at paths 1 and 2. The vertical line indicates \hat{L} values as calculated by Gaussian fits.

Figure 4.13: Analysis of light output spectra in muon measurements.

1. Light output spectrum fit: A light output spectrum of all events was produced, as shown for the measurement at direction 1 in Fig. 4.13a. A Gaussian fit with centroid \hat{L} and standard deviation σ was applied to the peak feature, as shown for both directions in Fig. 4.13b.
2. Peak event selection: Events in the peak feature are identified by selecting events with light output in the range $\hat{L} \pm \sigma$.
3. Pulse shape distribution fit: A distribution of the S values for peak events is produced. A Gaussian fit is applied to this distribution to estimate the expected pulse shape parameter \hat{S} produced by a muon, as shown in Fig. 4.14.

4.3.3 Measurement Results

The magnitudes of change in the \hat{L} and \hat{S} values between measurements at paths 1 and 2 were calculated as the ratio of the maximum to minimum value measured. The magnitude of change in the \hat{L} value was 1.005 ± 0.009 , and the magnitude of change in the \hat{S} value was 1.004 ± 0.026 . Neither showed a statistically significant change for muons between paths 1 and 2. Thus, no difference was measured in the light output and pulse shape produced by muon events traveling in anthracene at paths 1 and 2.

It is still possible that there is a very small anisotropy present that is not measurable by this system. These results can serve to set an upper boundary on the magnitude of

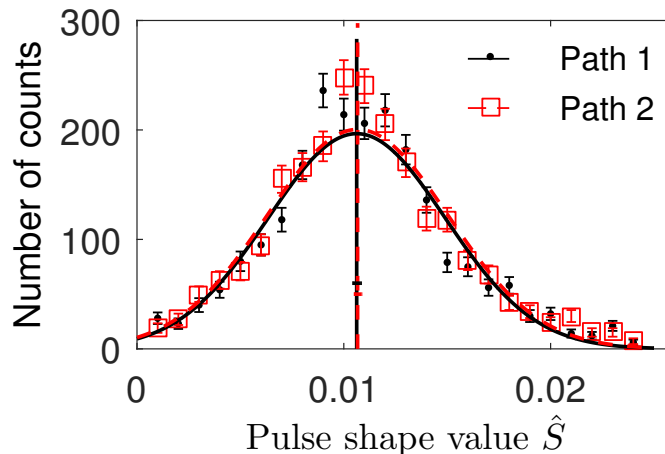


Figure 4.14: Distribution of S values for events with light output in the range $\hat{L} \pm \sigma$ produced by cosmic muons in anthracene at paths 1 and 2. Points represent measurements, and overlying curves are the Gaussian fits applied. The vertical lines indicate the locations of the expected pulse shape parameters \hat{S} .

anisotropy in anthracene at these muon paths. To $1\text{-}\sigma$, these results are inconsistent with a magnitude of change in light output greater than 1.013 and a magnitude of change in the pulse shape parameter greater than 1.030 for muons traveling at directions 1 and 2.

4.4 Interpretation of Anthracene Results and Update to Hypothesis

Table 4.4 compares the magnitude of change measured in the light output and pulse shape parameter for protons, electrons, and muons traveling at directions 1 and 2, as defined in Sec. 4.3, in the anthracene crystal. The table shows two major differences in the interactions of these particles. First, protons and muons travel in a straight path as they deposit their energy, while the electron does not. Second, the electron and muon produce comparable dE/dx , while the proton recoil produces much higher dE/dx in the material. Of these particles, an anisotropy was only observed in proton recoil interactions.

The lack of anisotropy observed in muon interactions provides new insights into the mechanism that produces the directional dependence in heavy charged particle interactions, which was introduced in Sec. 2.2.4. Since the muon, which travels in a straight path, does not experience a directional dependence, it can be concluded that the meandering path of the recoil electron is not solely responsible for the lack of directional dependence in gamma-ray interactions. This lends support to the theory that a high dE/dx is necessary for producing a measurable directional dependence.

This result fits into the hypothesis that the anisotropy is partly due to preferred directions

Table 4.4: Summary of Measurements Made on Anthracene Sample for Interactions at Directions 1 and 2.

Source Particle	Neutron	Neutron	Gamma ray	Muon
Recoil Particle	Proton	Proton	Electron	–
Path	Straight	Straight	Non-straight	Straight
Energy (MeV)	14	2.5	0.478	4000
dE/dx (MeV/cm)	42.9	166.7	2.5	2.4
\hat{L} mag. change	1.060 ± 0.005	1.108 ± 0.012	1.005 ± 0.004	1.005 ± 0.009
\hat{S} mag. change	1.062 ± 0.002	1.022 ± 0.007	1.006 ± 0.017	1.004 ± 0.026
Anisotropy Observed	Yes	Yes	No	No

of excitation transport. This transport changes the excitation density over time, affecting the relative rates of the physical chemistry processes responsible for light emission and quenching presented in Sec. 2.2.2. Depending on the initial distribution of excitations compared to the directions of rapid transport, the excitations may move towards one another or away from one another, changing the rates of interactive processes such as triplet-triplet annihilation and singlet quenching and, in turn, affecting the amount of light produced and the time distribution. For heavy charged particles that interact with high dE/dx , the change in the excitation density is significant compared to the overall density. For gamma-ray and muon interactions, the overall excitation density is low enough due to their low dE/dx that these changes are not significant enough to change the scintillation output on an observable level.

Brooks and Jones postulated that exciton transport occurs more rapidly within ab -planes than between ab -planes. These results argue that transport occurs most rapidly in the b -direction, next most rapidly in the a -direction, and least rapidly in the c' -direction. In turn, the exciton density remains highest when the proton recoil deposits its excitations along the b -axis because excitons will more readily travel within the path and encounter other excitons. In the a -, and even more so in the c' -directions, excitations will move away from the proton recoil's path and the density will decrease over time. Figure 2.10 illustrates two scenarios in which a proton recoil deposits energy along the direction of easy or difficult transport.

Similarly to understanding why the light output and pulse shape per energy deposited are different between neutron and gamma-ray events as discussed in Sec. 2.2.3, the anisotropy effect may be understood by considering the exciton density at different proton recoil directions. Table 4.5 summarizes the characteristics of excitation dynamics produced by proton recoil events along the b and c' -axes, hypothesized to be the directions of fastest and slowest excitation transport, respectively. Because excitations produced along the b -axis will experience faster transport within their recoil track, the density of excitations will remain high even as transport proceeds. This is compared to excitations produced along the c' -axis which will experience slowest transport within their track and faster transport away from their track so the density of excitations drops as transport proceeds. In the case of highest exciton density along the b -axis, excitons will experience relatively more singlet quenching and triplet-triplet annihilation compared to excitons generated along the c' -axis, resulting in

a minimal light output and maximal fraction of delayed light. In the case of lowest exciton density along the c' -axis, in which the excitons move away from their trajectory most rapidly, excitons will experience the least singlet quenching and triplet-triplet annihilation relative to other processes, resulting in a maximal light output and minimal fraction of delayed light. The proton recoil traveling in the a -direction is the saddle point for both distributions in Figs. 4.4 and 4.5 as it is the direction of “middle” exciton travel and therefore “middle” exciton density.

Table 4.5: Comparison of excitation dynamics for proton recoil events along the b and c' axis. Dynamics for proton recoil events along the a axis are hypothesized to be in between those along the b - and c' -axes.

Characteristic	Recoil along b -axis	Recoil along c' -axis
Transport rate within recoil track	Fastest	Slowest
Spatial density of excitations	Remains high	Largest decrease
Rate of singlet quenching	Highest	Lowest
Amount of prompt light	Least	Most
Rate of triplet-triplet annihilation	Highest	Lowest
Amount of delayed light	Most	Least
Total light produced L	Least	Most
Pulse shape parameter S	Most	Least

Note: This assumes that the total light output L is dominated by and follows the directional dependence of the prompt light.

The inverse relationship between L and S depends on the assumption that L is dominated by the prompt light. To be more clear, it assumes that the absolute change in the prompt light due to the anisotropy is larger than the absolute change in the delayed light due to the anisotropy. While this holds for anthracene in which the direction of minimum light output corresponds to maximum pulse shape and visa versa, other materials have a different relationship between these two characteristics as will be demonstrated in Sec. 6.2. The hypothesis will be updated further in response to those observations in Sec. 6.2.6.

Chapter 5

Validation of Isotropic Response in Amorphous Scintillator Materials

According to the hypothesis presented in Sec. 2.2.4 and updated in Sec. 4.4, the physical mechanism that produces the directional dependence in the crystal scintillator materials relies on an ordered arrangement of molecules within the materials. If these materials did not have fixed, repeating molecular and crystal structure, no anisotropy should be produced. Thus, no anisotropy should be observed in plastic and liquid organic scintillators which have amorphous structure. Previous authors stated that no anisotropy effect was observed in amorphous plastic and liquid materials [18, p. 261], but no measurements were published to support that statement. In order to verify their statements and support the hypothesis, measurements were made of plastic and liquid scintillators to verify that no anisotropy is observed.

5.1 Materials and Measurement Technique

Directional measurements were made on a PSD-capable plastic scintillator and an EJ309 liquid scintillator. The plastic sample was a cylinder approximately 1.25 cm tall and 2.5 cm in diameter. The plastic sample was wrapped and coupled to the PMT using the same procedure as described in Sec. 3.2.1. The liquid scintillator was EJ-309 encased in a 5 cm tall 5 cm diameter cylinder.

In order to characterize the directional response in these materials, the expected light output \hat{L} and pulse shape \hat{S} were measured for 14.1 MeV proton recoil events at different directions in the materials. Measurements were performed using the same process described in Sec. 4.1, and the same process was used for calculating \hat{L} and \hat{S} as was used for the anthracene measurements described in Sec. 4.1.2.

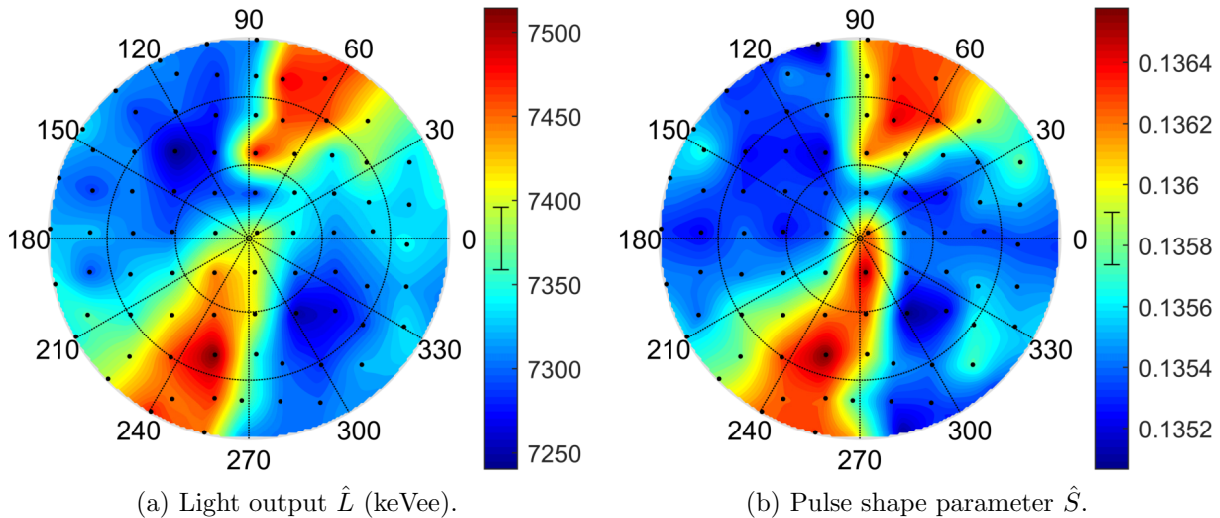


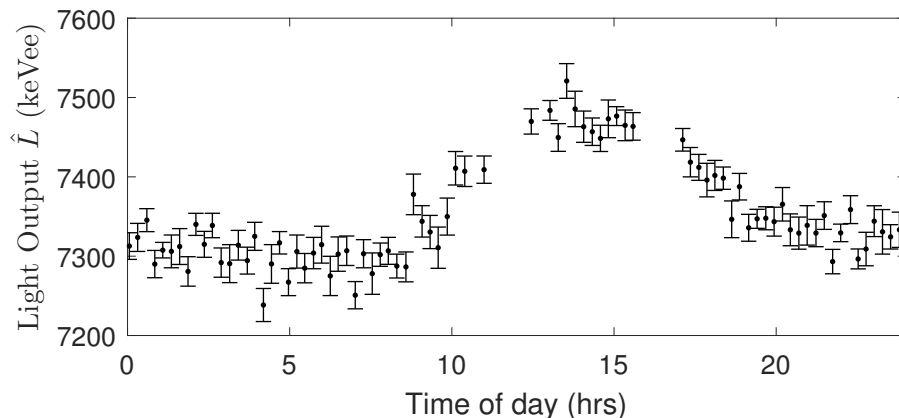
Figure 5.1: Response of PSD-capable plastic scintillator at various recoil directions to 14.1 MeV protons for preliminary measurement without temperature characterization. See Fig. 4.4 caption for a detailed explanation of the anisotropy plots.

5.2 First Observation of Temperature Dependence

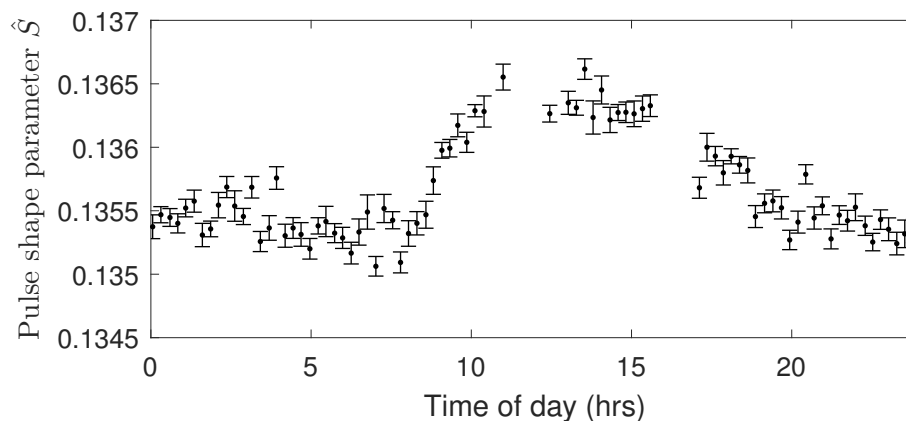
The first attempt at measuring the scintillation anisotropy in the plastic scintillator produced seemingly very surprising results. Figure 5.1 shows the directional \hat{L} and \hat{S} distributions calculated for 14.1 MeV proton recoil events incident on the plastic scintillator detector. It appears from these distributions that there is in fact a scintillation anisotropy correlated to the detector orientation, which would not exist if the plastic scintillator were amorphous, as it is.

Upon further analysis it was discovered that the light output and pulse shape parameter are correlated with the time of day when each measurement was taken. Figure 5.2 shows plots of the light output \hat{L} and pulse shape parameter \hat{S} vs. the time of measurement expressed as the hour in the day. These measurements were taken over two days with each measurement lasting about 30 min. The distribution is consistent with a temperature dependence in which \hat{L} and \hat{S} both increase as the temperature increases. Both \hat{L} and \hat{S} peak near noon and remain high until approximately 3:00 PM much like the temperature profile in the Livermore, California area in July when these measurements were taken.

This was the first measurement that provided an indication that temperature effects may be significant. After this measurement, a temperature sensor was purchased and the room temperature was recorded for all measurements. Since the temperature in the laboratory is not fixed or easily controlled, two strategies were successful for minimizing temperature effects: 1) temperature effects were corrected for using an independent characterization of the temperature dependence, as in the case of the gamma-ray measurements on anthracene



(a) Light output \hat{L} (keVee).



(b) Pulse shape parameter \hat{S} .

Figure 5.2: Response of PSD-capable plastic scintillator vs. time of measurement for preliminary measurement without temperature characterization.

discussed in Sec. 4.2, or 2) measurements were made over a period in which the temperature did not vary much, which was accomplished entirely by luck in several measurements such as the plastic and liquid measurements shown next in Sec. 5.3. This was not always successful, and several measurements in this dissertation display what appears to be noticeable temperature effects, such as the measurements of DD neutrons on stilbene in Fig. 6.3.

5.3 Measurement Results and Analysis

Figure 5.3 shows the directional light output and pulse shape response of the EJ309 liquid to 14.1 MeV protons and the average temperature in the laboratory during the time of each measurement. The same distributions for measurements of the PSD-capable plastic sample are shown in Fig. 5.4. For both measurements, which were taken simultaneously with

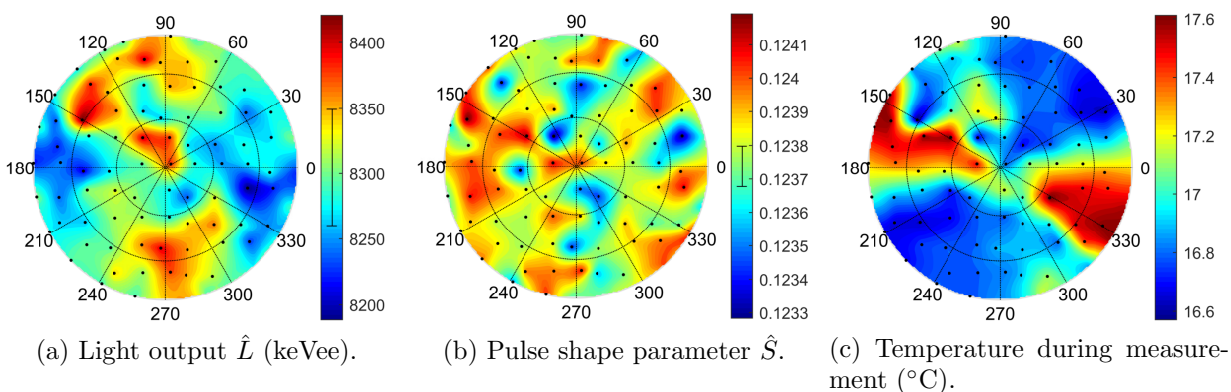


Figure 5.3: Response of EJ309 liquid scintillator at various recoil directions to 14.1 MeV protons.

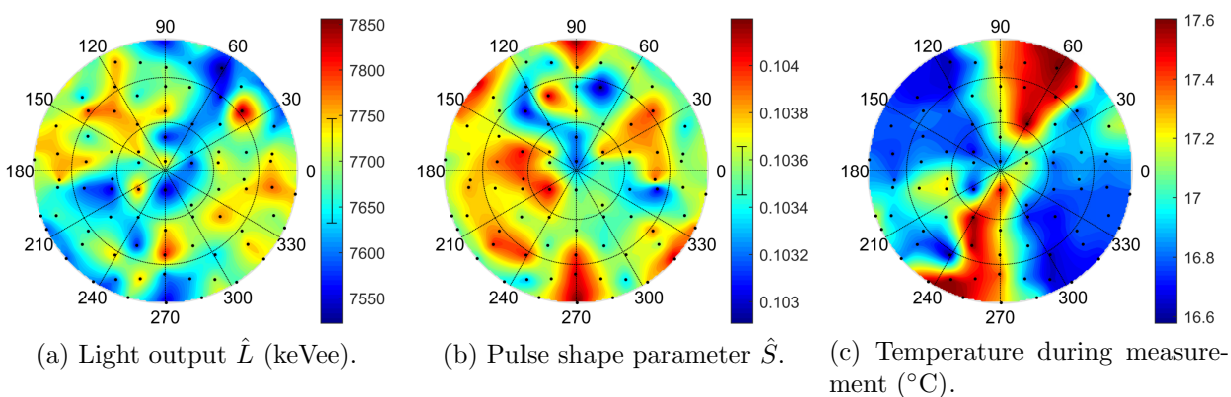


Figure 5.4: (a-b) Response of PSD-capable plastic scintillator at various recoil directions to 14.1 MeV protons and (c) approximate room temperature during measurements. See Fig. 4.4 caption for a detailed explanation of the anisotropy plots.

the two detectors in different positions on the rotational stage, the average temperature in the lab changed over a range of approximately 1°C . Additional measurements were taken of 2.5 MeV proton recoils for both detectors, and similar features were observed in the directional responses.

These measurements do not show any directional dependence correlated to detector orientation. The strongest evidence supporting that conclusion is the lack of qualitative features that are observed in the crystalline detectors. These measurements do not show a maximum, minimum, and saddle point region in the hemisphere with smooth transitions in between as was observed in the anthracene measurements in Sec. 4.1 or the other pure crystals that will be shown in Sec. 6. Instead, the directional dependence appears to be random variability from statistical and other non-statistical effects.

One source of variability that was significant in the measurements of gamma-ray events on anthracene in Sec. 4.2 was temperature. For the measurements on the plastic and liquid detectors, the room temperature varied within a range of 1°C for the DT measurements and within 2°C for the DD measurements. If the relationship between the light output, pulse shape, and temperature were known, temperature effects could be corrected for, but the plots in Fig. 5.3 and Fig. 5.4 show that the features in the temperature distribution do not mimic those in the light output or pulse shape distributions, so temperature effects do not appear to dominate the variations. There are a handful of sharp features that appear correlated that may be eliminated with a temperature correction. For instance, in the EJ309 data at $(\theta, \phi) = (70^\circ, 150^\circ)$, there is a sharp contour in both the light output and temperature distributions. However, there are several other sharp contours in the temperature distribution that are not mirrored in the light output distribution, so it is concluded that temperature changes are not the leading source of variability and a temperature correction would not change the conclusion that no directional dependence correlated with detector orientation is observed.

Table 5.1 shows the observed variability σ_{obs} and the average statistical variability σ_{stat} in the liquid and plastic measurements. For all cases, σ_{obs} is on the order of σ_{stat} , and in the case of the light output at 2.5 MeV, σ_{stat} exceeds σ_{obs} . This indicates that statistical fluctuations dominate the observed variability, though other sources of variability exist. This is very different than in the anthracene measurements presented in Sec. 4.1.4, in which the statistical error was very small compared to the overall observed variability.

Table 5.1: Variability in directional measurements of liquid and plastic scintillators.

	E_{recoil} (MeV)	EJ309 Liquid		Plastic	
		14.1	2.5	14.1	2.5
\hat{L}	$\sigma_{\text{obs}} / \mu$	0.60%	1.51%	0.96%	2.37%
	$\sigma_{\text{stat}} / \mu$	0.55%	1.87%	0.76%	3.49%
\hat{S}	$\sigma_{\text{obs}} / \mu$	0.17%	0.62%	0.27%	1.10%
	$\sigma_{\text{stat}} / \mu$	0.05%	0.19%	0.10%	0.39%

5.4 Discussion

These measurements of liquid and plastic scintillators demonstrate that the light output and pulse shape do not experience a directional dependence correlated with detector orientation as the crystalline detectors do. Both qualitative and quantitative observations confirm statements made by previous authors that no directional dependence exists in amorphous organic scintillators.

The lack of directional variability correlated to detector orientation in these amorphous materials supports the leading hypothesis that the directional dependence observed in crys-

talline materials is in fact due to an internal effect requiring an ordered molecular or crystal structure and not produced by the measurement system or external factors [36].

Chapter 6

Investigation of Anisotropy Effect in Other Pure and Mixed Crystals

The following sections discuss measurements to characterize the scintillation anisotropy across a wide range of pure and mixed crystalline materials. Sec. 6.1 presents measurements of four crystalline stilbene materials of different sizes and growth methods that were made to investigate whether the scintillation anisotropy effect varies across stilbene samples of different conditions and characteristics. Sec. 6.2 presents and compares measurements of the scintillation anisotropy across five pure materials including anthracene, stilbene, p-terphenyl, bibenzyl (BB), and diphenylacetylene (DPAC). Sec. 6.3 presents a characterization of the scintillation anisotropy in mixed crystals containing BB and stilbene or DPAC and stilbene. The measurements in this section provide a broad set of observations that demonstrate that the scintillation anisotropy is extremely complex.

6.1 Investigating the Effect for Stilbene Detectors of Different Size and Quality

Stilbene is an organic crystal scintillator that has been used for many decades for radiation detection. Recently, a new solution-based growth method has been developed that produces large crystals with high light output and excellent neutron-gamma pulse shape discrimination (PSD) [3, 4, 5]. This solution-grown stilbene is receiving substantial interest over liquid and plastic alternatives as its performance is better than liquid and PSD-capable plastic scintillators [4, 37, 38]. Additionally, crystalline stilbene is not toxic and its solid form is often easier to work with than liquid scintillators that are subject to thermal expansion and risk of leaks.

While it has been established that stilbene is subject to a directional dependence in its response to heavy charged particle interactions, only limited measurements have been reported. Previous measurements of proton recoil events in stilbene include the magnitude of change in light output at 3.7, 8, and 22 MeV [7, 9], and the light output vs. angle in

two planes at 3.7 MeV [9] and in one plane at 14 MeV [15]. Thus far, no measurements of the effect across a full hemisphere of crystal axes have been provided. Additionally, all previous measurements were of melt-grown stilbene crystals. Given the rising popularity of solution-grown stilbene as a detection material, it is important to thoroughly characterize the directional dependence and understand if it depends on crystal size or growth method.

6.1.1 Samples Measured

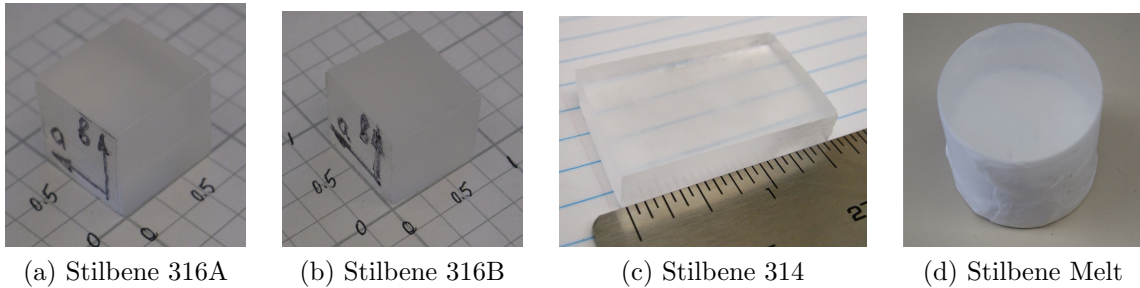
Measurements were made to characterize the scintillation anisotropy in melt-grown and solution-grown stilbene for 14.1 MeV and 2.5 MeV proton recoil events. In order to investigate how consistent the anisotropy effect is across stilbene detectors, four stilbene samples have been characterized. These include two solution-grown samples with the same dimensions, a solution-grown sample of different dimensions, and a melt-grown sample of different dimensions.

Characterizing the effect across these four detectors will provide information on whether the effect depends on crystal geometry or growth method, and will evaluate whether the effect varies significantly between two seemingly identical stilbene samples. The geometry of a crystal has been hypothesized to affect the anisotropy as it impacts the light collection efficiency and PSD performance [39]. The growth method and quality of the crystal has also been hypothesized to impact the measured anisotropy since the growth method does impact the light output and PSD performance [3, 4].

The directional response to 14.1 MeV and 2.5 MeV proton recoils was characterized in four stilbene samples, shown in Fig. 6.1. Three were produced using the solution-growth method. Of these three samples, two are cubic samples with 1.5 cm edge lengths and known crystal axes directions. The third is a rectangular prism with approximate dimensions 4.3 cm x 2.5 cm x 0.9 cm. The crystal axes directions in the third sample are unknown. The fourth sample is an older stilbene crystal with unknown history and considerable wear. It was produced using a melt-growth technique, so it is unlikely to be a perfect monocrystal. The crystal is cloudy and the surface has been polished many times. This crystal is a cylinder of size approximately 2.5 cm height and 2.5 cm diameter. Different timing windows were used for calculating the pulse shape parameter S for the solution-grown and melt-grown materials. The geometries and pulse shape timing windows are summarized in Table 6.1.

Table 6.1: Characteristics of stilbene materials measured, including steps used in calculating S in the pulse shape analysis.

		Shape	Dimensions (cm)	Δ_1	Δ_2
Solution-grown	316A	Cube	1.9 cm x 1.9 cm x 1.9 cm	10	60
	316B	Cube	1.9 cm x 1.9 cm x 1.9 cm	10	60
	314	Rectangular Prism	4.3 cm x 2.5 cm x 0.9 cm	10	60
Melt-grown		Cylinder	d = 2.5 cm; h = 2.5 cm	16	70



(a) Stilbene 316A (b) Stilbene 316B (c) Stilbene 314 (d) Stilbene Melt

Figure 6.1: Photos of solution-grown and melt-grown stilbene samples.

6.1.2 Measurement Results

Figure 6.2 shows the directional response of the 316B cubic solution-grown stilbene samples to 14.1 MeV proton recoil events, respectively. For each measurement, the expected light output \hat{L} , expected pulse shape parameter \hat{S} , and approximate room temperature are shown. The arbitrary set of axes described in Sec. 3.2.2 has been rotated in order to view the data such that the features of interest are on the interior of the plot and not on the edges. These measurements confirm statements by previous authors that the proton recoil direction of maximum light output is along the b -axis and minimum light output is along the c' -axis. The \hat{L} distribution shows a distinct maximum region at approximately $(\theta, \phi) = (50^\circ, 210^\circ)$ which is confirmed to be the direction of the b -axis in the crystal axes. The minimum region is at approximately $(\theta, \phi) = (60^\circ, 330^\circ)$ which is the c' -axis, and a saddle point is at approximately $(\theta, \phi) = (45^\circ, 90^\circ)$ which corresponds to the a -axis.

The locations of key features are similar between the \hat{L} and \hat{S} distributions. The locations of the maximum, minimum, and saddle points are approximately the same in both distributions. One difference between the \hat{L} and \hat{S} distributions in stilbene is that the gradient near larger values is much steeper in the \hat{S} distribution, making for wider “valleys” in the \hat{S} distribution than in the \hat{L} distribution.

Figure 6.3 shows the same plots for measurements of 2.5 MeV proton recoils produced by DD neutron interactions in stilbene crystal 316B. The qualitative features appear approximately the same as the DT measurements shown in Fig. 6.3, however the temperature fluctuations appear more noticeable. In the DT measurements, the \hat{L} and \hat{S} distributions did not show a noticeable correlation to the features in the temperature distribution, but in the DD measurements, there are several noticeable correlations. For instance, the \hat{S} measurement at approximately $(\theta, \phi) = (30^\circ, 30^\circ)$ is noticeably larger than the values in its vicinity, correlated to a lower temperature value. But temperature effects certainly do not dominate all of the features, and the scintillation anisotropy remains the most significant effect. The temperature dependence was not characterized on stilbene, but such a relationship could be used to correct for temperature effects in these measurements.

Figure 6.4 shows the directional \hat{L} and \hat{S} distributions at 14.1 MeV on the other cubic solution-grown stilbene sample 316A. The qualitative features are very similar to those in

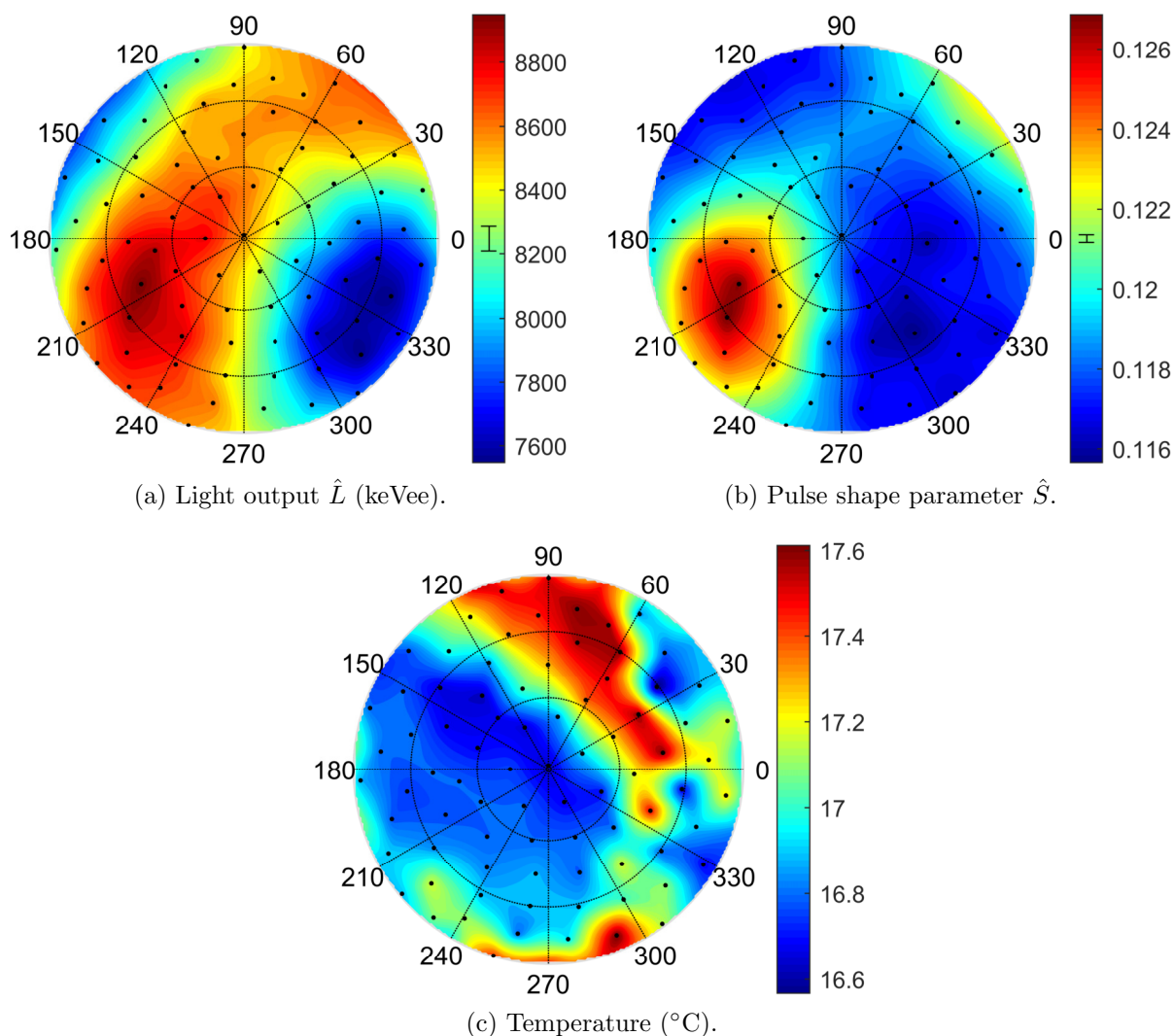
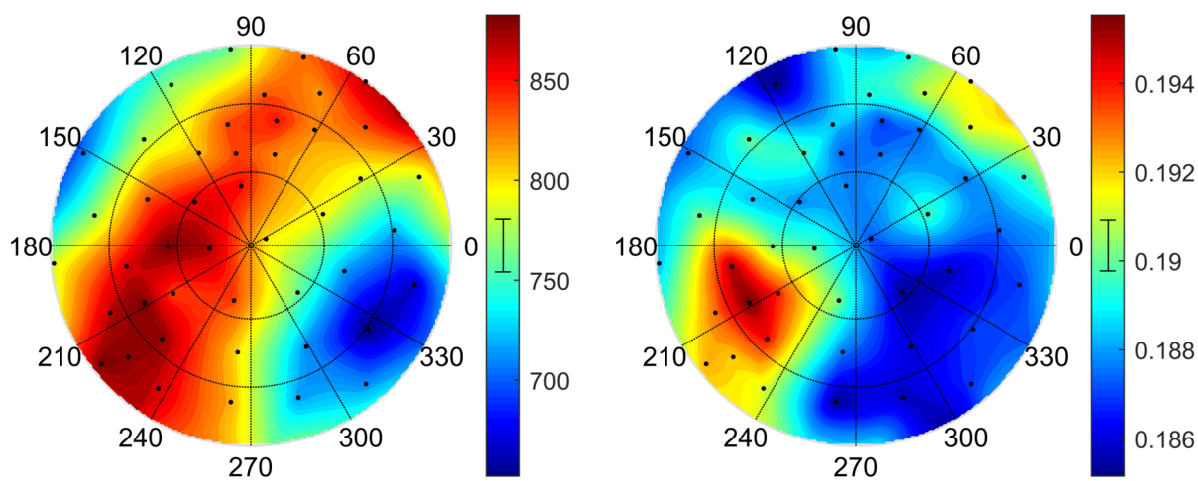


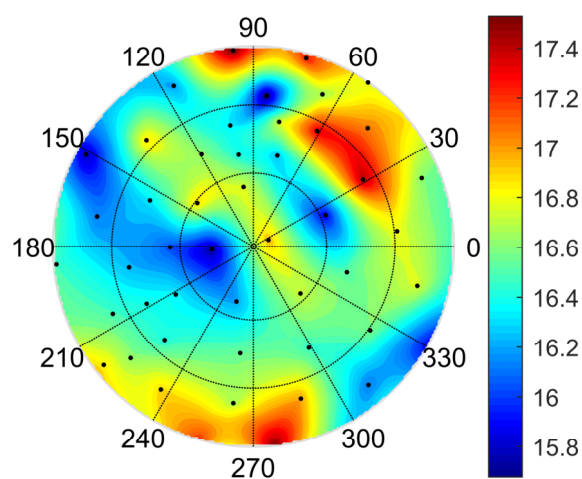
Figure 6.2: (a-b) Response of solution-grown cubic stilbene crystal 316B to 14.1 MeV proton recoil events at various proton recoil directions and (c) approximate room temperature during measurements. See Fig. 4.4 caption for a detailed explanation of the anisotropy plots.

stilbene sample 316B in Fig. 6.2, which was expected as those two detectors are the same size and produced by the same growth method. Fig. 6.5 shows the same distributions for the rectangular solution-grown stilbene crystal 314 which, again, show the same qualitative features. These measurements showed that the qualitative features observed in the directional distribution of the light output and pulse shape are consistent across solution-grown stilbene samples with different geometries and at different proton recoil energies.

Figures 6.6 and 6.7 shows the directional distributions for the melt-grown stilbene detector at 14.1 MeV and 2.5 MeV, respectively. The arbitrary crystal axes in the melt-grown



(a) Light output \hat{L} (keVee) for 2.5 MeV protons. (b) Pulse shape parameter \hat{S} for 2.5 MeV protons.



(c) Temperature ($^{\circ}\text{C}$).

Figure 6.3: (a-b) Response of solution-grown cubic stilbene crystal 316B to 2.5 MeV proton recoil events at various proton recoil directions and (c) approximate room temperature during measurements. See Fig. 4.4 caption for a detailed explanation of the anisotropy plots.

stilbene have been oriented so that the features approximately line up with the corresponding features in the solution-grown stilbene. These distributions show that the qualitative features in the directional light output and pulse shape responses are consistent between a melt-grown and solution-grown stilbene sample. Once again, the \hat{S} distribution presents more variability at 2.5 MeV than at 14.1 MeV. This variability may be due to temperature fluctuations, although there does not appear to be a distinct correlation between the \hat{S} and temperature distributions.

To quantify the magnitude of the directional dependence, two metrics are calculated

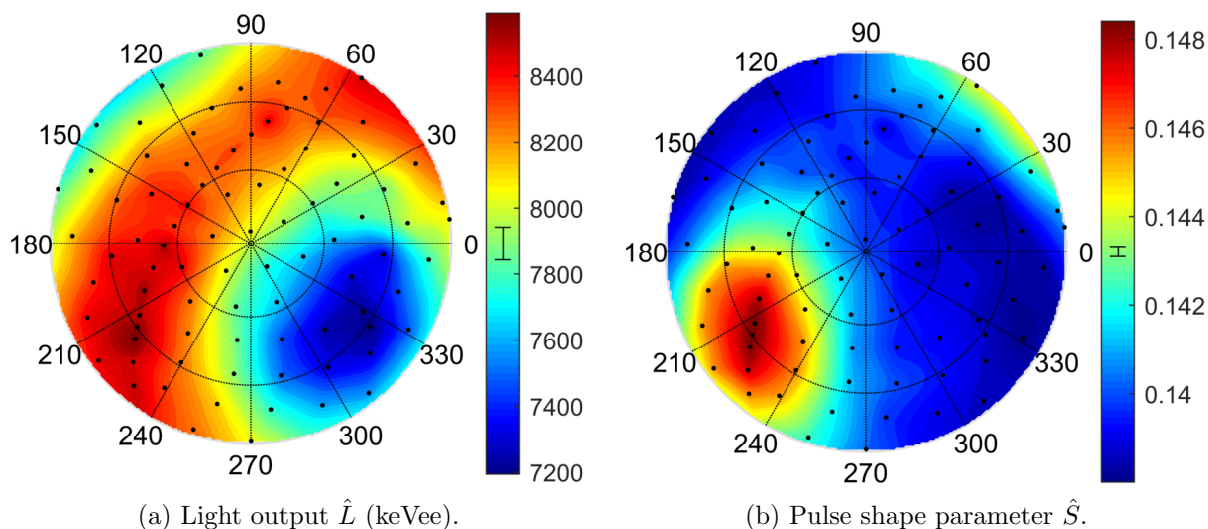


Figure 6.4: Response of solution-grown cubic stilbene crystal 316A to 14.1 MeV proton recoil events at various proton recoil directions. See Fig. 4.4 caption for a detailed explanation of the anisotropy plots.

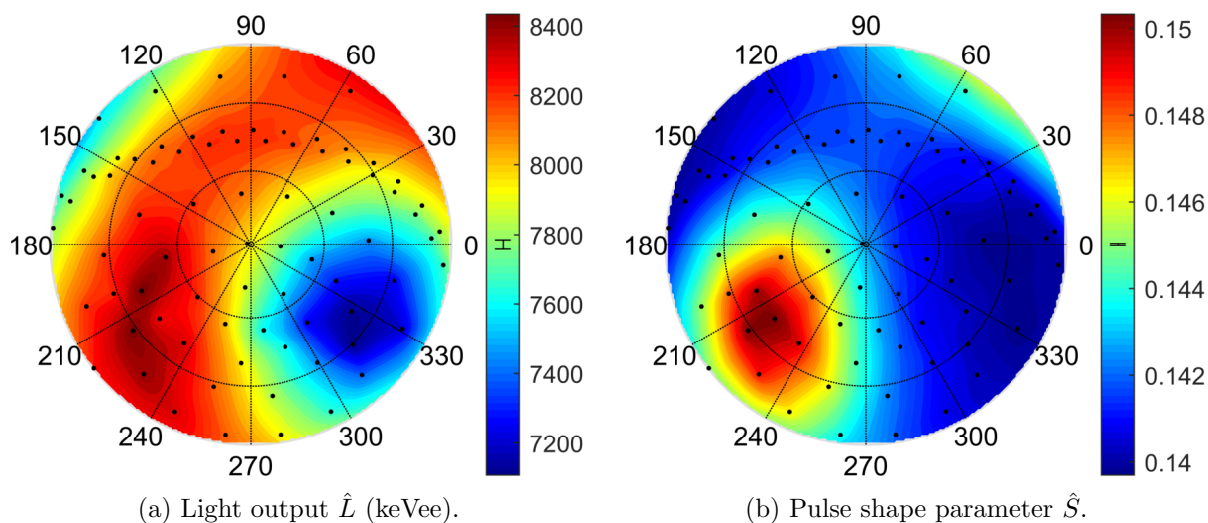


Figure 6.5: Response of solution-grown cubic stilbene crystal 314 to 14.1 MeV proton recoil events at various proton recoil directions. See Fig. 4.4 caption for a detailed explanation of the anisotropy plots.

for each detector. The first metric is the magnitude of change across all measurements,

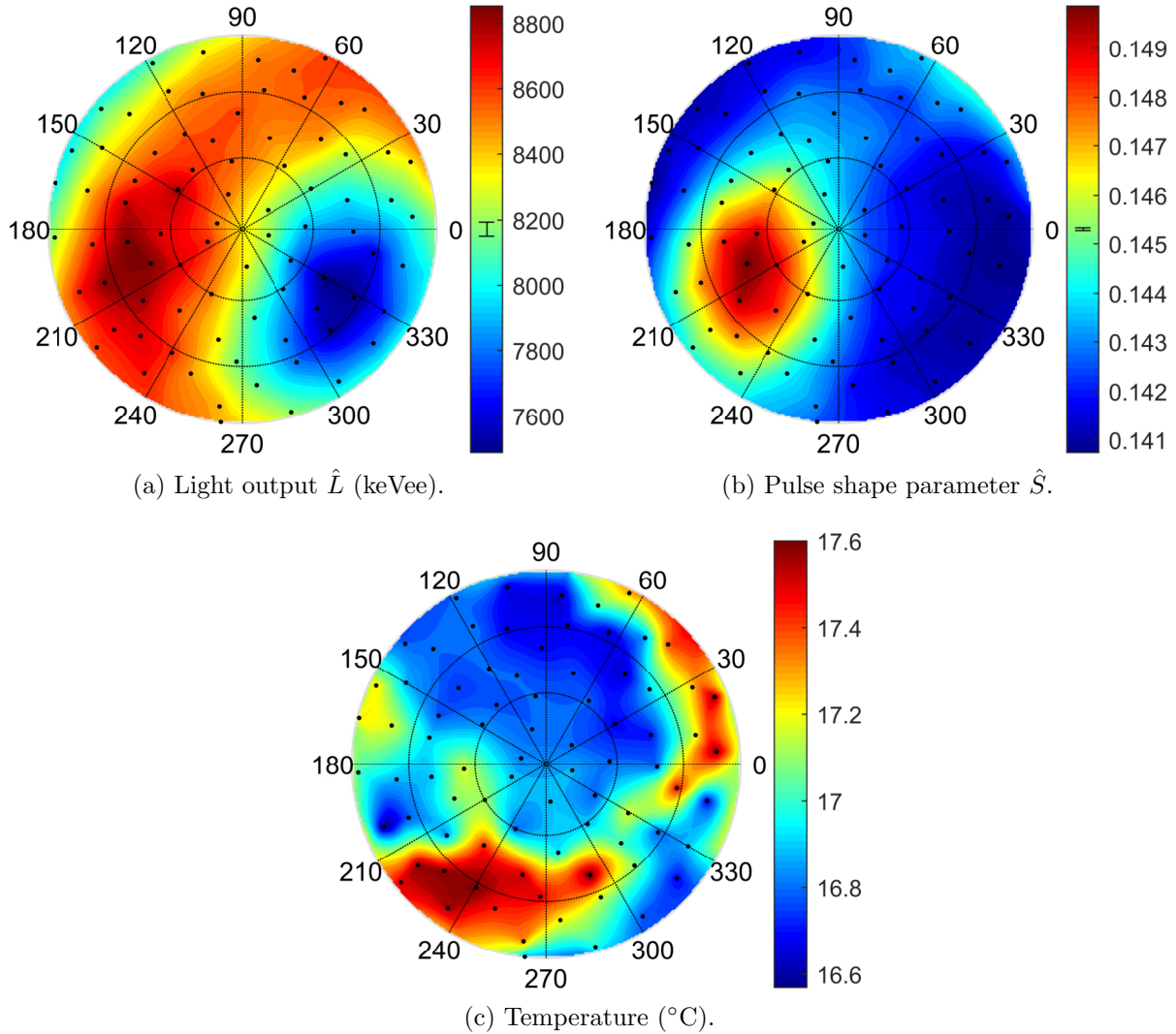


Figure 6.6: (a-b) Response of melt-grown stilbene crystal at various recoil directions to 14.1 MeV protons and (c) approximate room temperature during measurements. See Fig. 4.4 caption for a detailed explanation of the anisotropy plots.

calculated as the ratio of the maximum to minimum \hat{L} and \hat{S} values:

$$A_L = \frac{\hat{L}_{\max}}{\hat{L}_{\min}}, \text{ and} \quad A_S = \frac{\hat{S}_{\max}}{\hat{S}_{\min}}.$$

Table 6.2 shows the A_L and A_S values and their statistical errors calculated for the four stilbene materials measured. The A_L and A_S values are on the same order across all materials at 14.1 MeV, although the A_S value is not directly comparable between the solution-grown materials and the melt-grown materials because the timing windows for defining the delayed

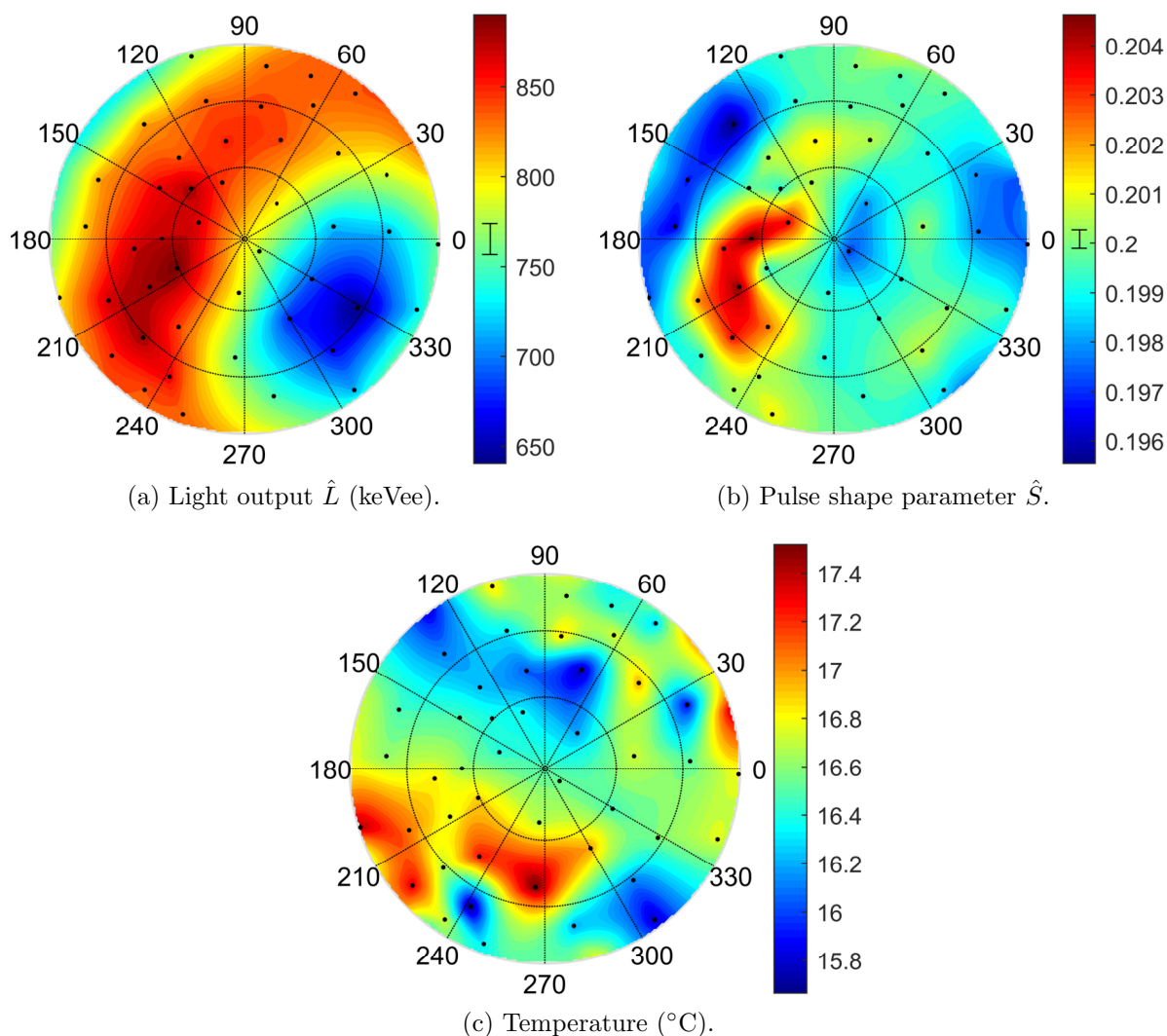


Figure 6.7: (a-b) Response of melt-grown stilbene crystal at various recoil directions to 2.5 MeV protons and (c) approximate room temperature during measurements. See Fig. 4.4 caption for a detailed explanation of the anisotropy plots.

region in calculating S are different. The statistical error is propagated from the error produced by the fit function, and does not account for systematic errors such as fluctuations due to temperature effects or the different distribution of angles measured in each material.

A_L and A_S vary more for measurements at 2.5 MeV than at 14.1 MeV, likely due to the difficulty in fitting the light output spectrum at 2.5 MeV. Figure 6.8 shows the neutron light output spectra for DT and DD neutrons measured at a given angle in the solution-grown cubic stilbene 316B sample. The edge in the light output spectrum is much clearer to the naked eye in the DT distribution than in the DD distribution for several reasons. First, the

Table 6.2: Magnitude of change in \hat{L} and \hat{S} values measured for stilbene detectors. *Indicates only maximum and minimum angles from DT measurements were measured at DD energies.

		A_L		A_S	
		14.1 MeV	2.5 MeV	14.1 MeV	2.5 MeV
Solution-grown	316A	1.200 ± 0.007	$1.468 \pm 0.050^*$	1.071 ± 0.001	$1.034 \pm 0.005^*$
	316B	1.191 ± 0.008	1.365 ± 0.039	1.100 ± 0.001	1.058 ± 0.007
	314	1.191 ± 0.004	$1.327 \pm 0.026^*$	1.078 ± 0.001	$1.039 \pm 0.005^*$
Melt-grown		1.187 ± 0.005	1.401 ± 0.055	1.066 ± 0.001	1.048 ± 0.003

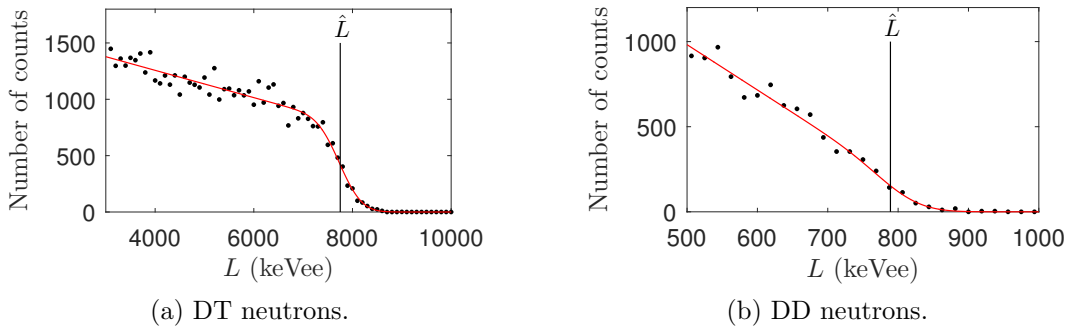


Figure 6.8: Light output spectrum fit as measured for DT and DD neutrons incident on the cubic solution-grown stilbene sample B.

DD measurements suffer from fewer events as the cross section for the DD reaction is much lower than that for the DT reaction. Also, there are fewer optical photons produced per DD event, making for lower energy resolution due to photostatistics. The fit function is much more robust for the DT measurements, and consistently locates the same \hat{L} value regardless of bin size. Although the fit function locates \hat{L} in the DD light output spectrum, it is not a very robust process, as changing the binning or fitting range can change the final \hat{L} value significantly. In the DD measurements on the cubic 316B and melt-grown samples, over 70 proton recoil directions were measured, and the distribution of \hat{L} and \hat{S} values showed features similar to the DT distributions, lending confidence that the fit function selected a consistent feature on the light output spectra. In the DD measurements on the cubic 316A and rectangular 314 samples, however, measurements were only taken at the angles of maximum and minimum light output from the corresponding DT measurements so no assessment of the overall features could be made, giving less confidence that the fit function performed consistently on those measurements, so the A_L and A_S values calculated from those two measurements are considered less reliable. Those values are indicated with an asterisk (*) in Table 6.2.

The magnitude of change of the light output in melt-grown stilbene samples has been reported by previous authors [7, 9]. Figure 6.9 shows the A_L value measured by previous authors and in this paper at different proton recoil energies. All measurements are consistent

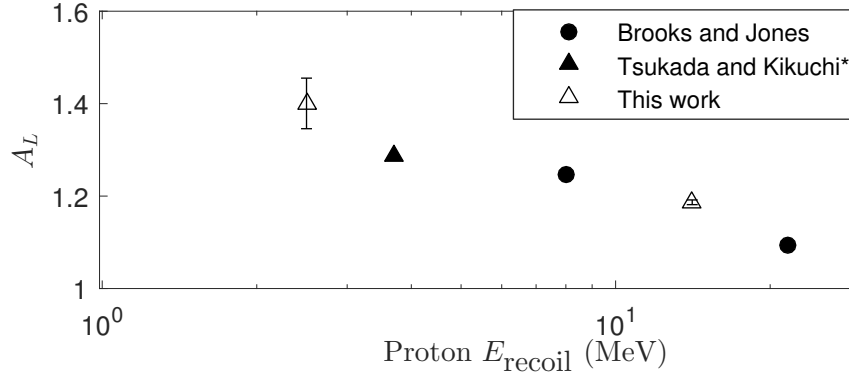


Figure 6.9: Magnitude of change in light output for proton recoil events at energies from 2.5-22 MeV in melt grown stilbene detectors as reported by Tsukada and Kikuchi [9], Brooks and Jones [7], and in this work. * A_L reported in [9] is for a polycrystalline sample, so it is likely lower than the true value.

with the trend that the magnitude of change in the light output decreases as the proton recoil energy increases. Comparing these results to similar measurements of anthracene in Sec. 4.1.3 made with the same detection system confirms previous authors' statements that the magnitude of the light output anisotropy in stilbene is on the same order as that in anthracene, but the pulse shape anisotropy is much greater in anthracene than in stilbene [7]. A comparison of \hat{L} and \hat{S} across five materials will be made in Sec. 6.2.

6.1.3 Assessment of Variability

Another metric for quantifying the anisotropy is the variability introduced to the \hat{L} and \hat{S} values by the effect. If the distribution of directions measured is approximated to be evenly distributed over the hemisphere, the observed standard deviation σ_{obs} of measured \hat{L} and \hat{S} values is related to the variability σ_{anis} introduced by the anisotropy effect. The contribution from statistical variance is subtracted in quadrature:

$$\sigma_{\text{anis}} = \sqrt{\sigma_{\text{obs}}^2 - \sigma_{\text{stat}}^2},$$

where σ_{stat}^2 is the average statistical variance from the set of measurements at different recoil directions. In all cases, the correction for σ_{stat} resulted in a $<5\%$ difference between σ_{obs} and σ_{anis} . Values of σ_{anis} for the four stilbene samples measured are given in Table 6.3, normalized to μ , the average measured value of \hat{L} or \hat{S} .

These measurements show that the variability introduced by the anisotropy at 14.1 MeV and 2.5 MeV is on the same order in solution-grown and melt-grown stilbene samples. Again, the pulse shape variabilities are not perfectly comparable as different timing windows were used for calculating S in the solution-grown and melt-grown detectors. Regardless, this

Table 6.3: Normalized variability, σ_{anis}/μ , introduced by the anisotropy in directional measurements of stilbene samples.

		Light output		Pulse shape	
		14.1 MeV	2.5 MeV	14.1 MeV	2.5 MeV
Solution-grown	316A	4.39%	n/a	1.95%	n/a
	316B	4.44%	7.42%	2.26%	1.37%
	314	3.92%	n/a	1.95%	n/a
Melt-grown		4.27%	7.80%	1.67%	0.99%

serves as an approximate comparison of the variability in the pulse shape as calculated for optimal neutron-gamma PSD in these materials.

These variability calculations have a number of systematic differences in measurements between samples that produce differing σ_{anis}/μ values. An obvious difference is that the alignment of the distribution of angles measured with respect to the crystal axes of the sample is different in all four samples. Even the two stilbene samples with known crystal axes were measured at different proton recoil direction distributions because of the difference in detector positions on the rotational stage. Since the calculation of σ_{anis}/μ assumes that the distribution of angles measured is evenly distributed across the hemisphere, which is an approximation, the distribution of proton recoils may be such that in one material the maximal and minimal directions are measured, while in another material those directions are missed so that the measured variability is smaller than the true variability. This work introduces the question of how significantly does the distribution of angles measured affect the σ_{anis}/μ value, and what do the \hat{L} and \hat{S} distributions look like around their maxima and minima. It is expected that taking measurements at more proton recoil directions would help mitigate this problem.

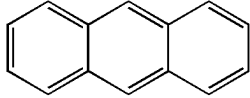
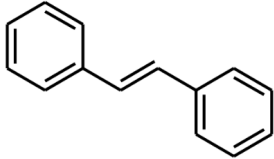

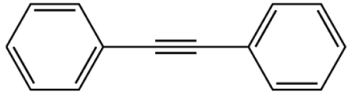
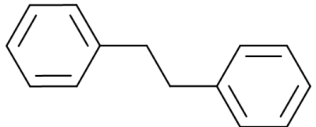
6.2 Comparison of Effect Across Five Pure Materials

6.2.1 Materials Measured

As shown in Sec. 4 and Sec. 6.1, the magnitude and behavior of the scintillation anisotropy for proton recoil events varies between anthracene and stilbene. While the magnitude of the light output anisotropy is on the same order between the two, the pulse shape anisotropy is much greater in anthracene ($A_S \approx 1.80$ at $E_{\text{recoil}} = 14.1$ MeV) than in stilbene ($A_S \approx 1.08$ at $E_{\text{recoil}} = 14.1$ MeV). Additionally, the behavior of the effect is different between the two materials. That is, the relationship between the light output and pulse shape differs. In anthracene, the proton recoil direction of maximal light output produced minimal pulse shape, but in stilbene the proton recoil direction of maximal light output produced maximal pulse shape. The question remains how the scintillation anisotropy compares in other organic crystal scintillator materials.

As described in Sec. 1.1.2, previous authors made limited measurements on other crystals and observed that the scintillation anisotropy was approximately the same across materials for a given proton recoil energy, but the pulse shape anisotropy varies greatly across materials. While measurements on several materials have been made, most of them only include the overall magnitude of change and do not provide the full hemisphere worth of proton recoil directions to thoroughly characterize the response. To investigate this further and produce a consistent dataset with the same measurement system, the scintillation anisotropy produced by 14.1 MeV proton recoil events was characterized across a number of pure materials using the system built for this dissertation. In addition to anthracene and stilbene, the characterization was performed on p-terphenyl, bibenzyl, and diphenylacetylene (DPAC). Characteristics of interest for these materials and illustrations of their molecular structures are shown in Table 6.4. Visualizations of the crystal structure from Mercury are shown in Fig. 6.10, and unit cell lengths as provided by Mercury are given in Table 6.5 [40].

Table 6.4: Summary of pure crystal materials characterized with their optimal pulse shape parameter Δ_1 and Δ_2 values.

	Formula	Density (g/cm ³)	Δ_1	Δ_2	Illustration
Anthracene	C ₁₄ H ₁₀	1.28	60	160	
Stilbene	C ₁₄ H ₁₂	0.97	10	60	
P-terphenyl	C ₁₈ H ₁₄	1.24	6	60	
DPAC	C ₁₄ H ₁₀	0.99	3	70	
Bibenzyl	C ₁₄ H ₁₄	0.98	24	100	

The anthracene sample was the same one described in Sec. 4 and is an older sample with considerable wear. The p-terphenyl sample was of approximately the same quality, and also has unknown history. Both of these samples have been polished many times and were produced by the melt-growth technique. The stilbene (stilbene 316B from Sec. 6.1),

Table 6.5: Crystal structure unit cell length for pure crystal materials [40].

	Formula	a (Å)	b (Å)	c (Å)
Anthracene	C ₁₄ H ₁₀	8.5526(12)	6.0158(11)	11.1720(16)
Stilbene	C ₁₄ H ₁₂	12.382(6)	5.720(1)	15.936(4)
P-terphenyl	C ₁₈ H ₁₄	8.106(4)	5.613(2)	13.613(6)
DPAC	C ₁₄ H ₁₀	15.488	5.754	12.766
Bibenzyl	C ₁₄ H ₁₄	12.77	6.12	7.7

bibenzyl, and DPAC samples were provided directly by Natalia Zaitseva of Lawrence Livermore National Laboratory, who grew the materials with a solution-growth method. These samples were all very high quality with few imperfections on the surface. The comparison of the anisotropy effect across all samples will not attempt to account for the differences in quality among these samples as it was demonstrated in Sec. 6.1 that stilbene samples of different sizes and growth methods produced approximately the same scintillation anisotropy in magnitude and behavior.

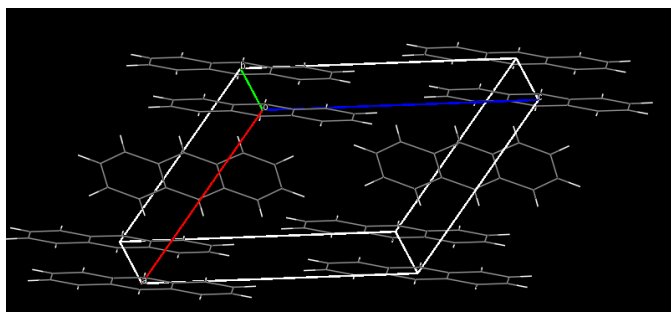
6.2.2 Data Analysis Challenges

One challenge in analyzing the data for these measurements was the great variety in the scintillation decay times that was observed. Table 6.4 shown the timing window boundaries Δ_1 and Δ_2 for the pulse shape parameter calculation. The values vary greatly as the decay times for each material vary, anthracene being the longest and DPAC being the shortest.

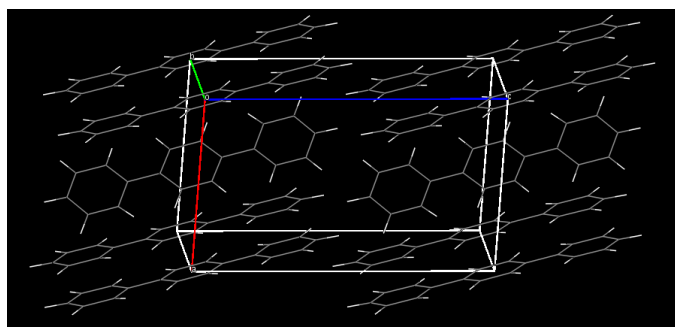
DPAC proved a difficult material to analyze because the light output resolution is very poor. Though the pulse shape resolution was excellent, it was difficult to produce a distribution of light output as a function of proton recoil direction that showed the expected maximal, minimal, and saddle point features, as will be shown in Sec. 6.2.3. To illustrate the difference in the light output resolution, Fig. 6.11 shows the neutron light output spectra for 14.1 MeV interactions on the stilbene and DPAC samples. In the stilbene measurement, the edge feature is much clearer to the naked eye and is identified with greater certainty by the fit function. In DPAC, the edge is nearly impossible to identify with the naked eye, and the fit function does not locate an edge position well. The uncertainty surrounding the edge location is greater than in the stilbene measurement, and the reliability of the fit function to pick out a consistent position between measurement is much less. Several techniques were attempted to improve the fit function on DPAC, but nothing was successful. DPAC was the only material with light output resolution poor enough to pose such a challenge.

6.2.3 Measurement Results

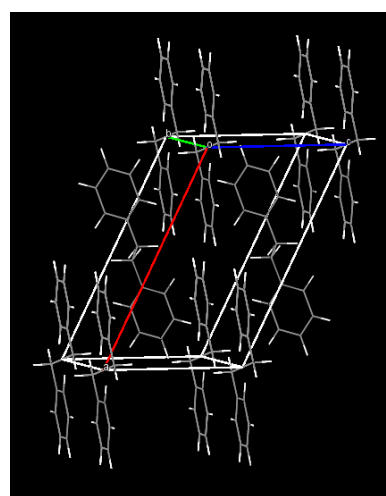
Fig. 6.12 shows the light output and pulse shape distributions for 14.1 MeV proton recoil events in all five pure materials measured. The anthracene and stilbene distributions have been provided in previous sections of the dissertation but are also reproduced here.



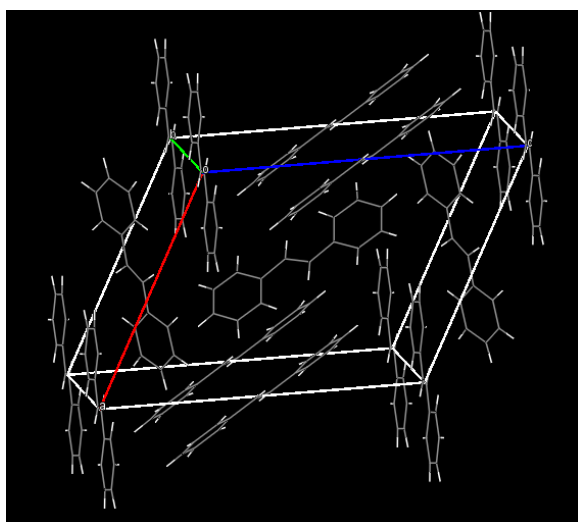
(a) Anthracene



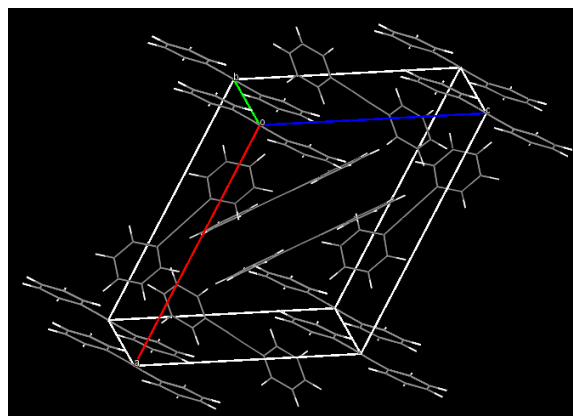
(b) P-terphenyl



(c) BB



(d) Stilbene



(e) DPAC

Figure 6.10: Visualization of the crystal structure for anthracene, p-terphenyl, bibenzyl (BB), stilbene, and diphenylacetylene (DPAC).

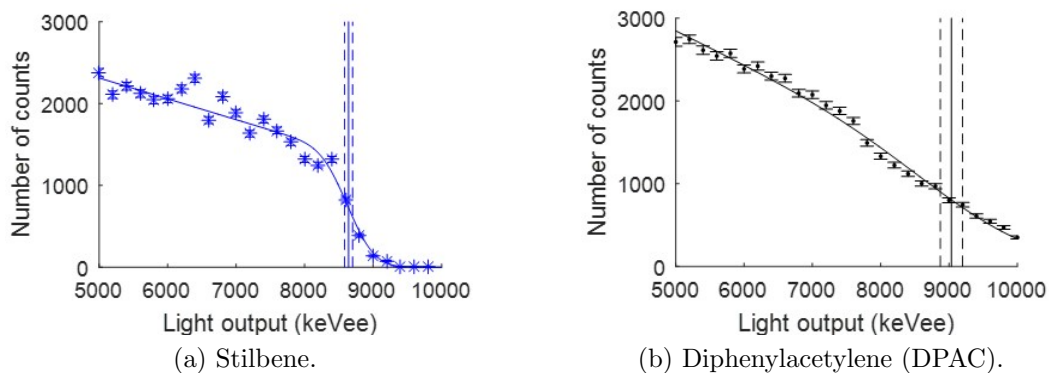
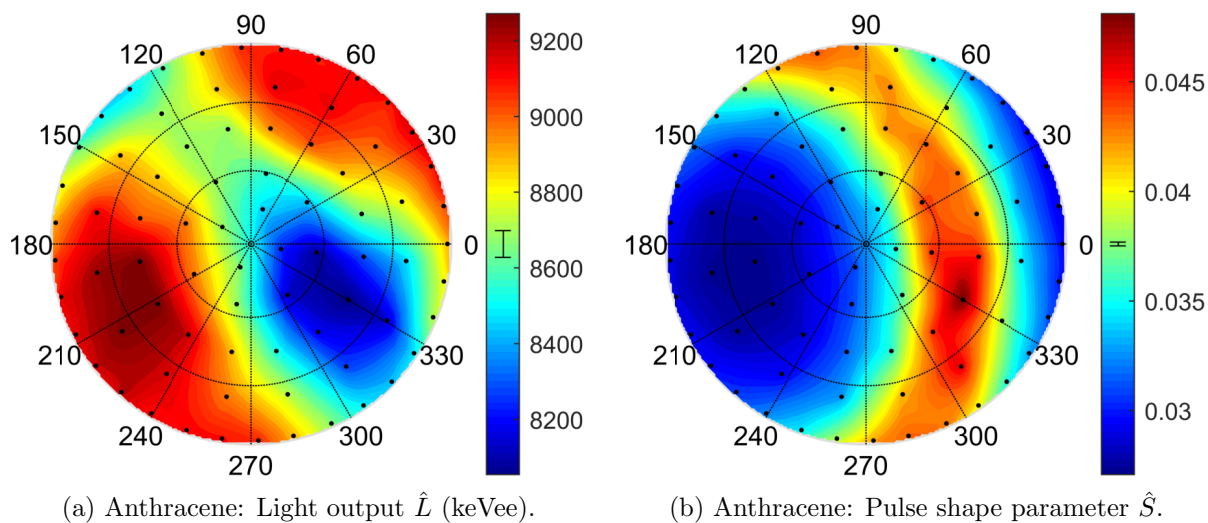
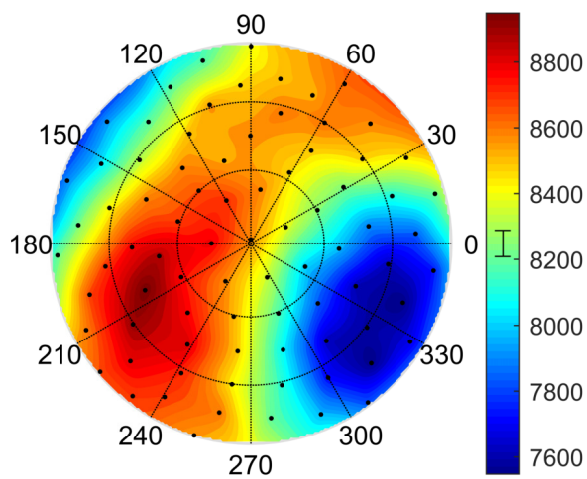


Figure 6.11: Comparison of light output spectrum produced by 14.1 MeV neutron events incident on stilbene and DPAC. The solid vertical line indicates the position of the edge, and the dotted vertical lines indicate the width of the uncertainty around the position of the edge as found by the fit function.

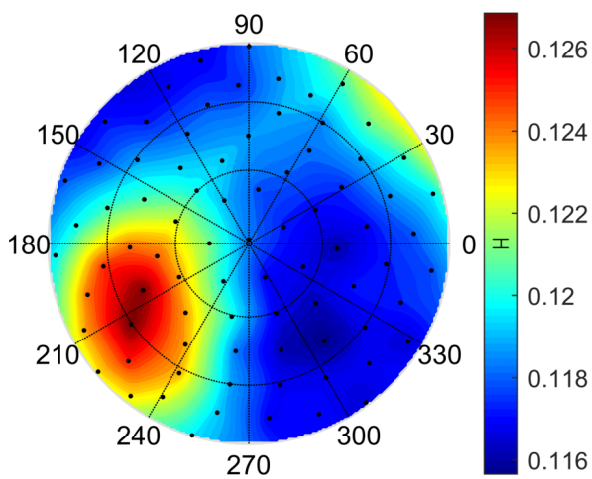


(a) Anthracene: Light output \hat{L} (keVee).

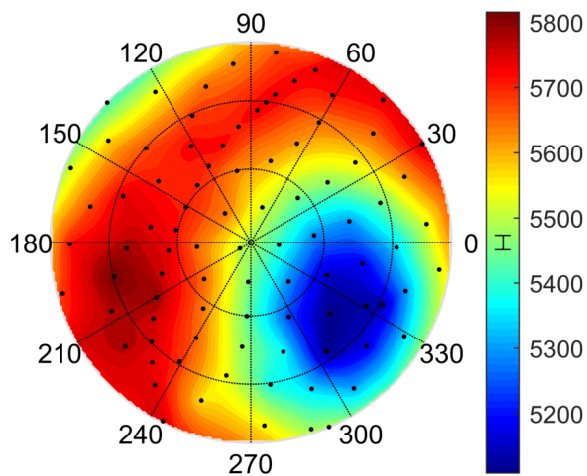
(b) Anthracene: Pulse shape parameter \hat{S} .



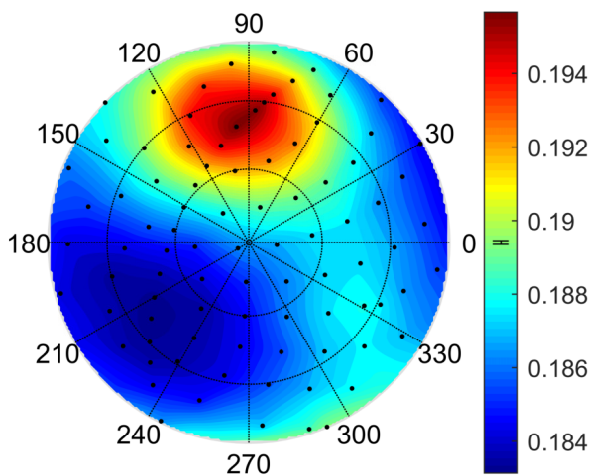
(a) Stilbene: Light output \hat{L} (keVee).



(b) Stilbene: Pulse shape parameter \hat{S} .



(a) P-terphenyl: Light output \hat{L} (keVee).



(b) P-terphenyl: Pulse shape parameter \hat{S} .

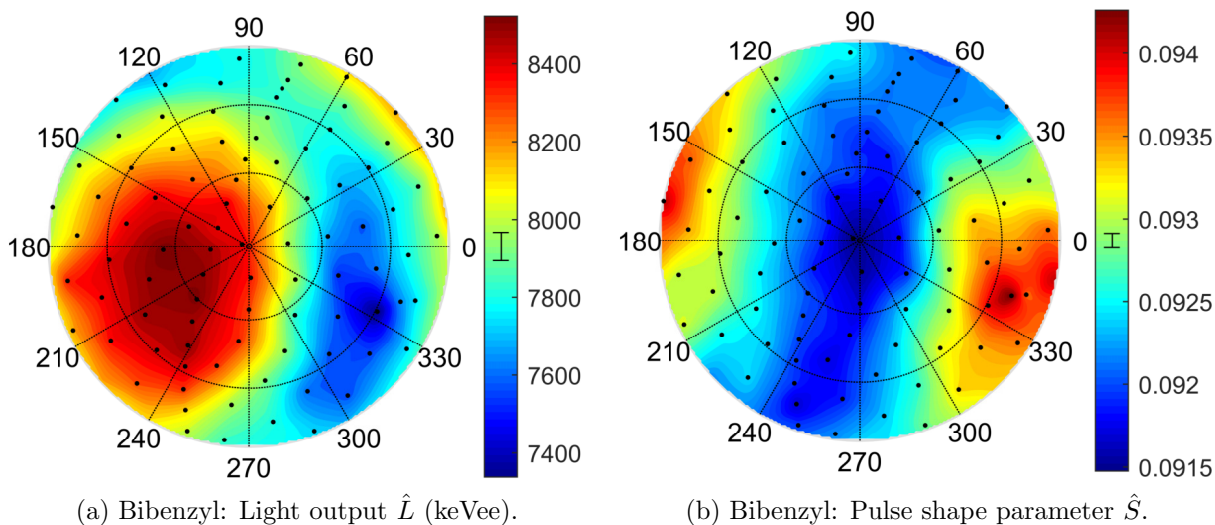
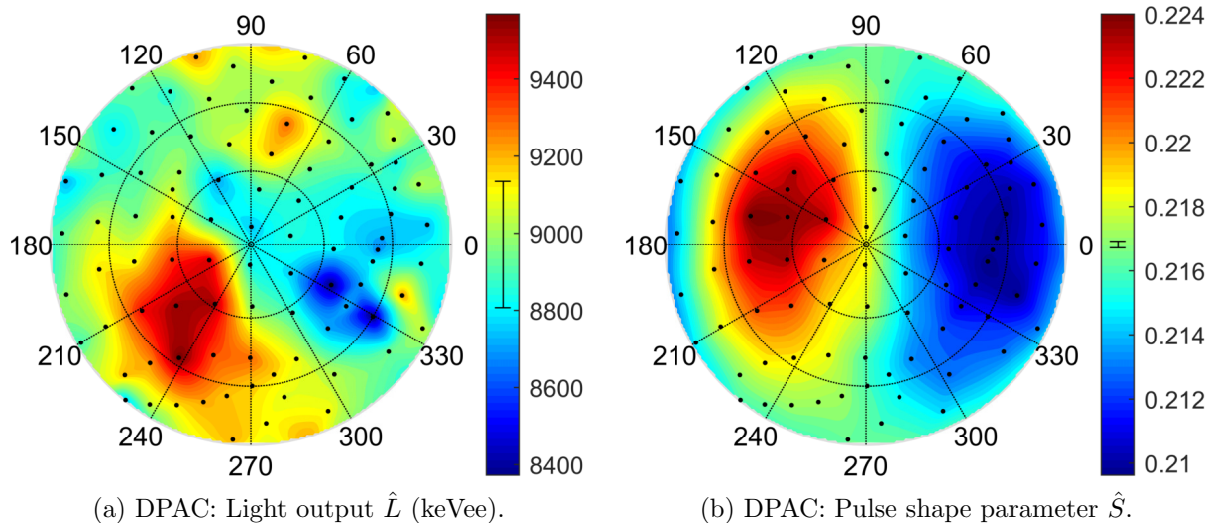


Figure 6.12: Response of five pure crystals at various recoil directions to 14.1 MeV protons. See Fig. 4.4 caption for a detailed explanation of the anisotropy plots.

The axes used in the directional distributions of the light output and pulse shape parameter for each material have been oriented so that the maximum, minimum, and saddle point features in the light output distribution occur in approximately the same position across all materials. This was done by shifting the entire coordinate system until an arbitrary set of axes was found in which the maximum light output occurred in the lower left of the 2D distribution, the minimum light output occurred in the lower right, and the saddle point near the top. This way, it is easy to look at the pulse shape distribution and quickly understand the relationship between the light output and pulse shape and how that relationship differs across materials. These differences will be discussed both quantitatively and qualitatively in the next sections.

6.2.4 Qualitative Analysis

The first observation across these distributions is that the relationship between the light output and pulse shape differs greatly between materials. It was already pointed out that anthracene and stilbene have a different relationship in that the maxima and minima are in opposite positions between the light output and pulse shape distributions in anthracene, but are in the same positions in stilbene. For convenience, the relationship in anthracene will be described as having the maxima and minima “out of sync” and the saddle point feature “in sync.” In stilbene the features are at the same proton recoil directions between the light output and pulse shape distribution, so they are all described as “in sync.” Table 6.6 compares the relationship in all materials.

Table 6.6: List of which feature in the \hat{S} distribution corresponds to which feature in the \hat{L} distribution for the five pure materials measured.

	Max \hat{L}	Min \hat{L}	Saddle \hat{L}	Relationship
Anthracene	Min \hat{S}	Max \hat{S}	Saddle \hat{S}	Max, min out of sync; Saddle in sync
Stilbene	Max \hat{S}	Min \hat{S}	Saddle \hat{S}	All in sync
P-terphenyl	Min \hat{S}	Saddle \hat{S}	Max \hat{L}	All out of sync
Diphenylacetylene	n/a	n/a	n/a	n/a
Bibenzyl	Min \hat{S}	Max \hat{S}	Saddle \hat{S}	Max, min out of sync; Saddle in sync

The relationship is complicated further in p-terphenyl, in which the three features are all out of sync. The maximum \hat{L} corresponds to the minimum \hat{S} ; the minimum \hat{L} corresponds to the saddle \hat{S} ; the saddle \hat{L} corresponds to the maximum \hat{L} .

The relationship in bibenzyl is also interesting because, while it appears to be the same as in anthracene with the maxima and minima out of sync and the saddle point in sync, the maximum \hat{L} and minimum \hat{S} are not perfectly lined up. This is similar to anthracene in that the saddle point in the \hat{L} and \hat{S} distributions in anthracene are actually off by about 30°. This shows that while the \hat{L} and \hat{S} values are correlated, and that correlation is different

across materials, there is not a one-to-one fixed relationship in each material, and the \hat{L} shape can differ greatly from the \hat{S} shape.

Unfortunately, because the light output resolution DPAC is so poor, the features are ambiguous and it is not clear whether the features are in or out of sync. It appears that the maxima and minima are in approximately the same position, but there is enough uncertainty that no conclusion can be drawn. This relationship in DPAC is of considerable interest because the crystal structure is very similar between stilbene and DPAC, and if the relationship between \hat{L} and \hat{S} were the same in both materials, that would support a hypothesis that the crystal structure determines the behavior of the effect.

6.2.5 Quantitative Analysis

The magnitude of the light output anisotropy is roughly the same order across all materials measured, as shown in Table 6.7. The pulse shape anisotropy, however, varies greatly in its magnitude across materials. Anthracene indeed experiences the greatest pulse shape anisotropy, as stated by previous authors and validating the choice to use anthracene for the gamma-ray and muon measurements. It appears that the smallest pulse shape anisotropy is experienced by bibenzyl.

Table 6.7: Magnitude of change in \hat{L} and \hat{S} values measured for 14.1 MeV proton recoil events in various pure crystal detectors (using stilbene 316B from Sec. 6.1.2).

	A_L	A_S
Anthracene	1.155 ± 0.006	1.798 ± 0.006
Stilbene	1.191 ± 0.008	1.100 ± 0.001
P-terphenyl	1.142 ± 0.003	1.070 ± 0.001
Diphenylacetylene	1.148 ± 0.031	1.070 ± 0.001
Bibenzyl	1.161 ± 0.008	1.032 ± 0.001

Again, the relationship between stilbene and DPAC is interesting, as they have very similar molecular and crystal structure. Although the A_L value for DPAC is not very robust due to the poor light output resolution, the A_S value is fairly robust, and is close to that of stilbene. Numerous systematic differences may exist to account for the small difference, which were discussed in detail in Sec. 4.1.4. While it's not possible from this data to assess which errors are more or less significant for DPAC compared to the detailed analysis of anthracene, this data argues that further work should be done to study DPAC and compare it to stilbene.

6.2.6 Interpretation of Pure Materials Measurement Results and Update to Hypothesis

According to the hypothesis presented in Sec. 2.2.4, a major process responsible for producing the scintillation anisotropy is the preferred directions of transport in organic crystal

scintillator materials. The scintillation anisotropy in anthracene was interpreted in Sec. 4.4 to be consistent with most rapid transport in the b -direction, next most rapid in the a -direction, and slowest transport in the c' -direction. Assuming that the absolute change in the prompt light due to the anisotropy is more than the absolute change in the delayed light, and the preferred directions of transport are the same for singlet and triplet excitations, it follows that proton recoil directions with highest total L values will experience lowest pulse shape parameter S values, and visa versa.

However, the directions of preferred transport in any given material (as compared with anthracene) are not necessarily the same for singlet and triplet excitations, so the densities of singlet and triplet excitations do not necessary increase and decrease together. Thus, the inverse relationship between light output L and pulse shape parameter S is not necessarily fixed, as observed in other materials.

6.2.6.1 Different Directions of Preferred Transport for Singlets, Triplets in Two Dimensions

Because each material has different molecular and crystal structure, the preferred direction of transport within a crystal for a singlet excitation may not necessarily be the same as that for a triplet excitation. As described briefly in Sec. 2.2.2, the preferred direction of singlet transport depends on the direction of the transition dipole moment of the molecule and the rate of triplet transport will be greater in directions with strong π -orbital overlap, both of which depend on the molecular and crystal structure. The dependence on molecular and crystal structure is likely not straight forward, but experimental or quantitative methods may exist for calculating the preferred directions of singlet and triplet transport. It may be possible to determine the direction of preferred singlet transport, a longer range interaction, by measuring the photoconductivity across a bulk material in different directions. Triplet transport, a shorter range interaction, depends more on the local crystal and electronic structure of a molecule. Optical measurement techniques exist for measuring the directional diffusion length of triplet excitations, such as that used by Akselrod *et al.* [31] on tetracene. Also, computational methods such as density functional theory (DFT) may be useful in calculating the directional transport likelihood for triplet excitations.

Revisiting the simple two-dimensional illustration of how excitation densities may change over time, one can imagine how different preferred directions of transport can change the relationship between light output and pulse shape. Figure 2.10 in Sec. 2.2.4 illustrated how the excitation density remains high when the excitations are produced along the crystal axis with easier transport and how the density drops when the excitations are produced along the crystal axis with difficult transport.

Figure 6.13 illustrates a simple two-dimensional lattice that has different directions of preferred transport for singlet and triplet excitations. In the case shown, the proton recoil travels roughly along the horizontal axis, creating a distribution of singlet (open) and triplet (filled) excitations. Over time, the singlet excitations travel preferentially away from the

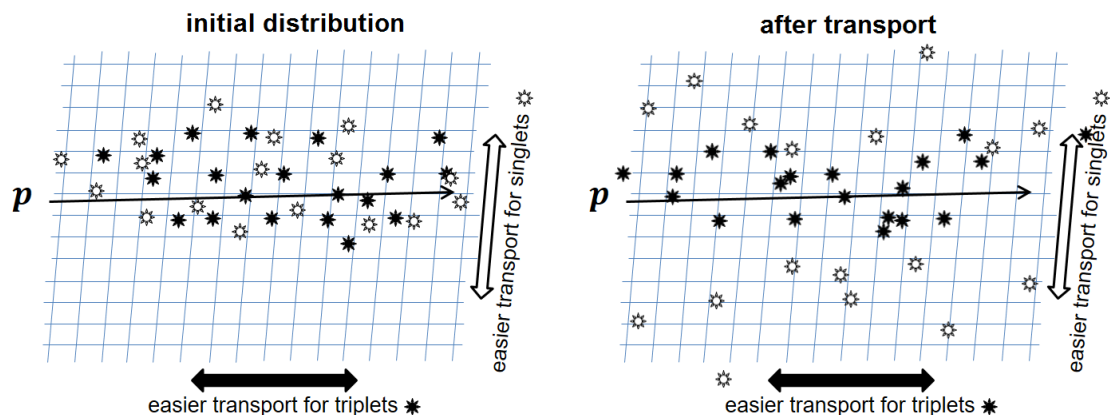


Figure 6.13: Illustration of excitation transport over time when singlet and triplet excitations have different directions of preferred transport.

track, and the singlet density drops. The triplet excitations, however, travel preferentially within the track, and the triplet density remains high.

When the directions of preferred transport were the same, the proton recoil direction that produced the highest excitation densities produced higher rates of singlet quenching and triplet-triplet annihilation, so a decrease in prompt light due to more singlet quenching was accompanied by an increase in delayed light due to more triplet-triplet annihilation. If the total light output was assumed to be dominated by the prompt light, and the pulse shape is calculated as the ratio of delayed to prompt light, then this means that an increase in L means a decrease in S .

In the case illustrated in Fig. 6.13, however, this is no longer true. Now a lower singlet density is accompanied by a higher triplet density. Thus, the direction that produces less singlet quenching, leading to more prompt light, also produces more triplet-triplet annihilation, leading to more delayed light. Now the total L is increased, but it is not clear how the pulse shape parameter S will change. Since S is the ratio of delayed to prompt light, both of which are changing, the overall change in S will depend on whether the prompt or delayed light changes by a greater factor. Now there exists the possibility for the light output and pulse shape parameter to be in sync, as is observed in stilbene.

6.2.6.2 Different Directions of Preferred Transport for Singlets, Triplets in Three Dimensions

In order to explain the relationship between L and S observed in p-terphenyl, in which the maxima, minima, and saddle points of each distribution are out of sync, one must consider that there are three dimensions within the crystal axes. When only limited to two dimensions, and assuming that the direction of easiest and hardest transport are along crystal axes (which may not be true), the direction of easiest and hardest transport for singlets and triplets must

be either the same direction or opposite directions. When opened up to three dimensions, now they need not line up. For instance, the direction of maximum and minimum transport for singlet excitations may correspond to the direction of maximum and medium transport for triplet excitations, and the direction of minimum transport for triplet excitations is the third remaining direction.

Since the light output anisotropy may be approximated as measuring the anisotropy due to singlet light emission, one may be able to infer the directions of preferred transport for singlet excitations based on the scintillation anisotropy. The pulse shape anisotropy is not as straightforward, as it depends on both singlet and triplet excitations. It may be possible to learn something about triplet transport by comparing the pulse shape anisotropy to the light output anisotropy.

6.3 Measurements of Mixed Crystals

6.3.1 Materials Measured

Work is being done by physical chemistry and materials science groups to improve the performance of organic crystal scintillators for many applications by producing new materials based on previous generations of materials. One example of this work is the production of mixed crystals by Zaitseva *et al.* at Lawrence Livermore National Laboratory [41]. They showed that crystals with varying proportions of diphenylacetylene (DPAC) and stilbene showed different scintillation properties. To summarize, pure DPAC and pure stilbene each are capable of pulse shape discrimination (PSD) because the pulse shape produced by a neutron event differs from that produced by a gamma-ray event. When stilbene is added to DPAC in very small concentrations from roughly 2% to 10%, the pulse shapes from events produced by neutron and gamma-ray events appear the same. As more stilbene is added, differences return for pulse shapes produced by neutron and gamma-ray events, and the resolution between the two distributions of pulse shapes is the best for approximately 55% stilbene. As the stilbene concentration increases further, the PSD remains, though decreases slightly in quality. Although DPAC and stilbene have the same crystal structure, it is not known what the crystal structure of the mixed crystals is.

Similar mixed crystalline materials were produced with bibenzyl and stilbene. Zaitseva *et al.* found that a dilute stilbene component wiped out the PSD in bibenzyl, but that further increasing the fraction of stilbene once again brought back the PSD, as occurred in DPAC. Zaitseva provided several samples for characterizing the scintillation anisotropy. Figure 6.14 shows pictures of the seven samples available, and Table 6.8 gives the timing windows used for PSD in the five that are PSD-capable. Measurements made on these materials confirmed that no PSD was present for the samples with dilute stilbene.

Figure 6.15 shows visualizations in the program “Mercury” of the crystal structure for BB, stilbene, and DPAC [40]. These visualizations show that the crystal structure of BB is slightly different from those for stilbene and DPAC, which have nearly identical crystal

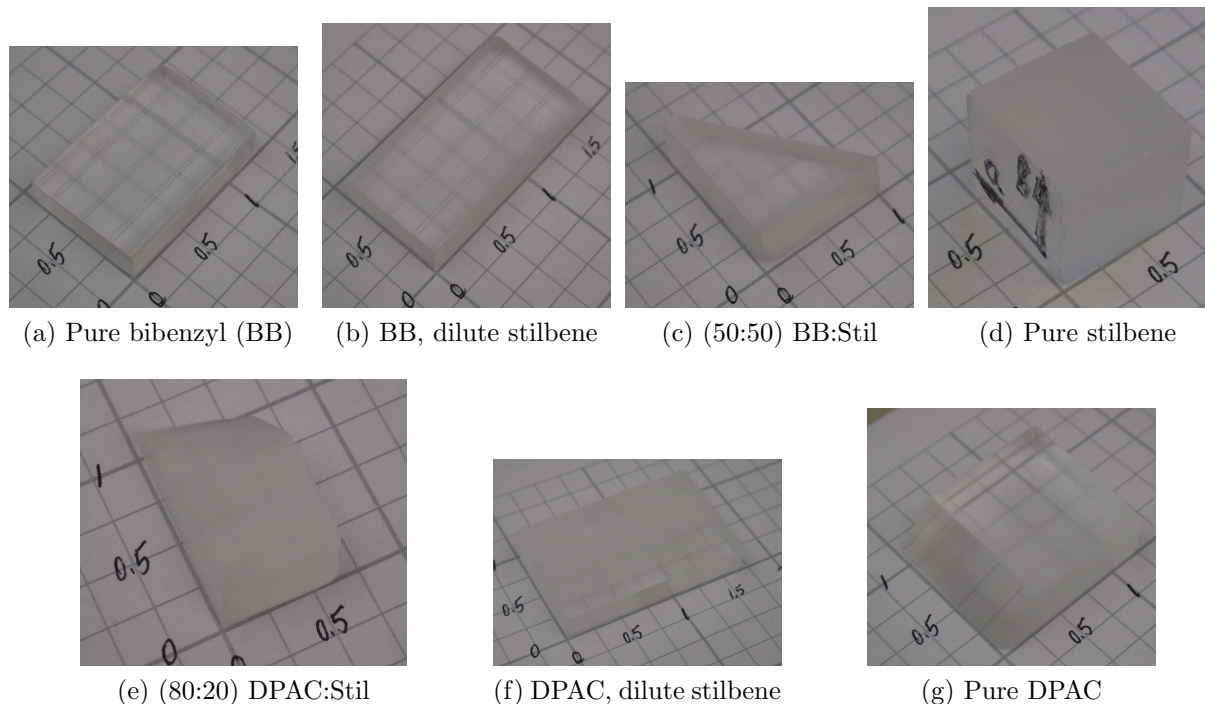


Figure 6.14: Photos of samples measured in the mixed crystal study.

Table 6.8: Summary of optimal pulse shape parameter Δ_1 and Δ_2 values for PSD-capable mixed crystal materials.

Material	Δ_1	Δ_2
Pure bibenzyl (BB)	24	100
(50:50) BB:Stil	15	65
Pure stilbene	10	60
(80:20) DPAC:Stil	7	50
Pure DPAC	3	70

structure. In all three materials, the orientation of molecules in alternating planes is different, but the angle between the long axis in molecules in alternating planes is much greater in stilbene and DPAC than in bibenzyl.

6.3.2 Measurement Results and Analysis for BB:Stil

Measurements of the BB with dilute stilbene sample did not show any neutron-gamma pulse shape discrimination, as was observed by Zaitseva *et al.* [41], so pulse shape parameters were not calculated for this material. The question remains whether there exists a light output anisotropy. Since the endpoint of the neutron light output spectrum exceeds the endpoint of

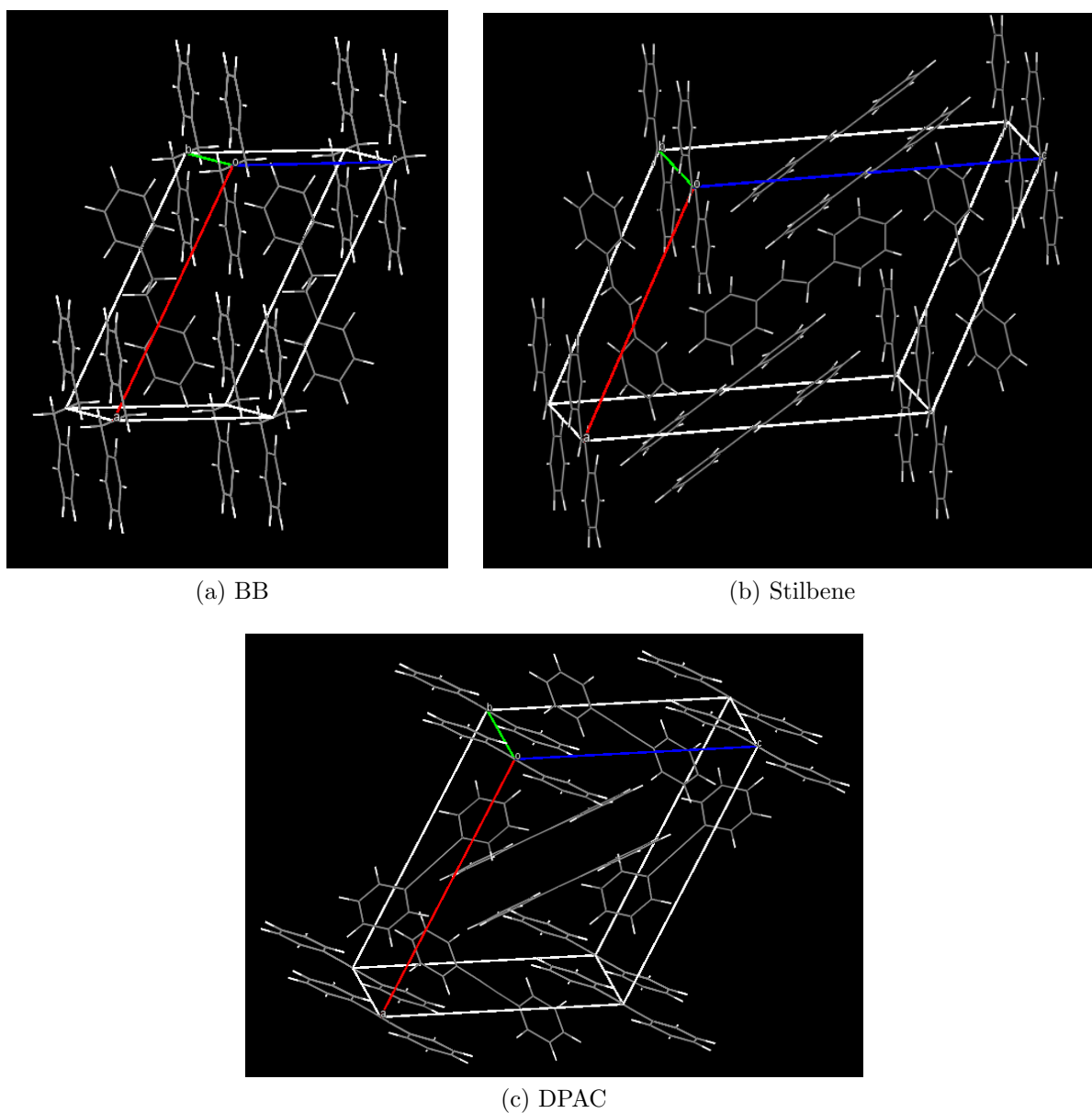


Figure 6.15: Visualization of the crystal structure for bibenzyl (BB), stilbene, and diphenylacetylene (DPAC).

the gamma-ray light output spectrum, it is possible to fit the endpoint of the neutron light output spectrum even without first identifying and removing gamma-ray events. Figure 6.16 shows the directional light output distribution next to the ambient room temperature for each measurement. The features in the two plots mirror each other very closely, indicating that the features in the light output distribution are not due to an internal scintillation anisotropy,

but rather are due to temperature effects. Figure 6.17 shows the relationship between the expected light output \hat{L} and ambient room temperature in this material. This relationship shows a very strong positive correlation. Although this correlation appears strong, this measurement can not be used as a characterization of the temperature dependence in this material because each measurement was taken at a different proton recoil direction. Since the proton recoil direction was not fixed, this is not a controlled measurement of the temperature dependence and can not be used to correct for the temperature dependence in the \hat{L} values. Regardless, it indicates that there is a strong temperature dependence in this material that is likely the dominating source of the observed variability.

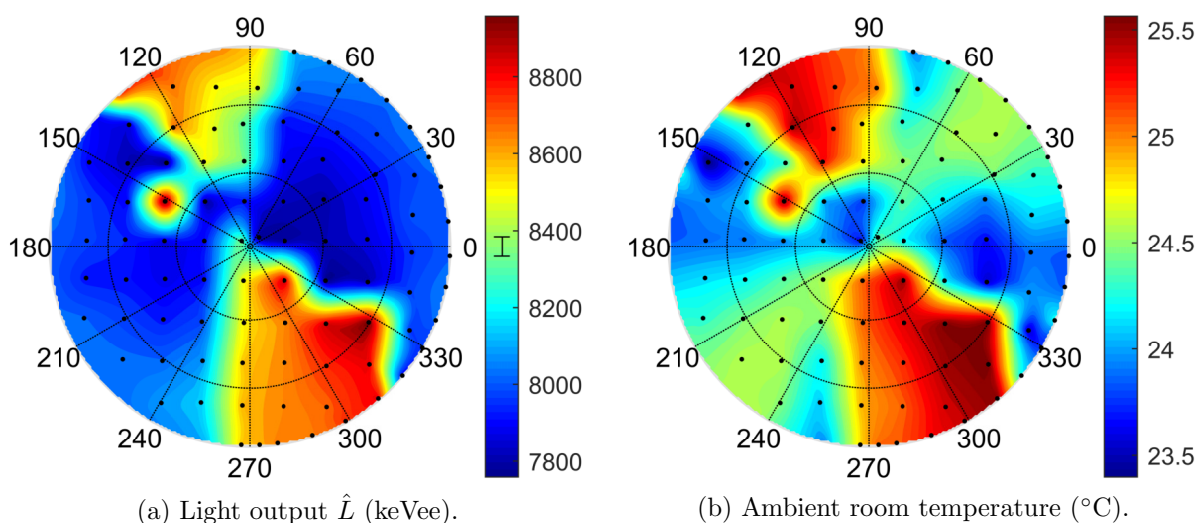


Figure 6.16: Light output response and approximate room temperature during measurement of bibenzyl with dilute stilbene crystal at various recoil directions to 14.1 MeV protons. See Fig. 4.4 caption for a detailed explanation of the anisotropy plots.

The first result for the (50:50) BB:stilbene sample to consider is the result of the PSD timing window optimization. Δ_1 and Δ_2 are given in Table 6.8. For both of the mixed materials, the optimal timing constants are between those for the two corresponding pure materials. BB has a slower decay time than stilbene, which produces longer optimal timing windows, while DPAC has a faster decay time than stilbene, producing shorter optimal timing windows. The mixed BB:Stil sample has timing windows between pure stilbene and pure BB, and the mixed DPAC:Stil sample has timing windows between pure stilbene and pure DPAC. Although the scintillation mechanism in the mixed crystal is not well understood, this indicates that it may be a function of both components in the crystal.

Figure 6.18 shows the light output and pulse shape scintillation anisotropies for the varieties of BB:Stil mixed crystals that are PSD-capable. The most significant qualitative feature is the relationship between the light output and pulse shape, which mirrors that of pure stilbene. The mixed BB:Stil sample behaves like the pure stilbene in that its maximal,

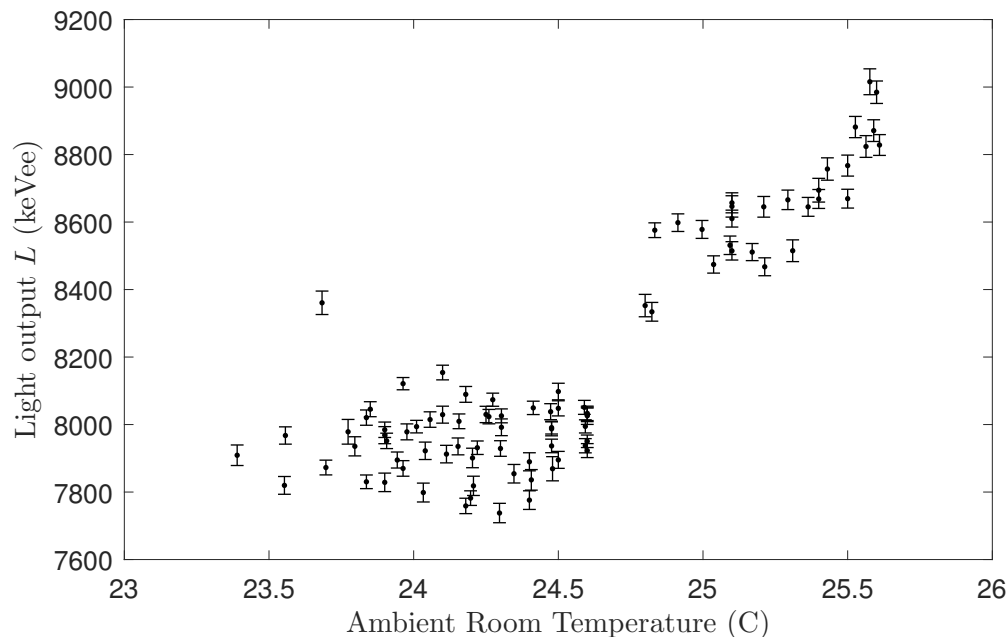


Figure 6.17: Expected light output \hat{L} vs. measurement temperature for measurements of 14.1 MeV neutrons incident on the bibenzyl with dilute stilbene detector.

minimal, and saddle point features in the light output and pulse shape distributions are in sync. Since it is still unknown which crystal or molecular properties dictate the anisotropy, it is not clear what this means. It could indicate that stilbene is the dominant scintillating molecule, or that the crystal structure of the mixed material follows the structure of pure stilbene.

The next interesting finding is in calculating the magnitude of the anisotropy. Table 6.9 gives the anisotropy expressed as the magnitude of change in the light output A_L and the pulse shape parameter A_S . While the light output anisotropy in the mixed sample is very close to that of pure stilbene, the pulse shape anisotropy is closer to that of BB. This may mean that the light output anisotropy, which is closely related to singlet excitation dynamics, is more tied to the stilbene population, while the pulse shape anisotropy, which is a combination of singlet and triplet excitation dynamics, is also tied to the BB population. Perhaps stilbene is the primary scintillating agent, explaining the mirrored relationship between the light output and pulse shape anisotropies and the similar magnitude in the pulse shape anisotropy, but the bibenzyl affects the triplet population to a larger degree, impacting the magnitude of the pulse shape anisotropy. The DPAC results in the next section, however, may indicate that the scintillation anisotropy in both mixed materials is more determined by stilbene than by DPAC or BB.

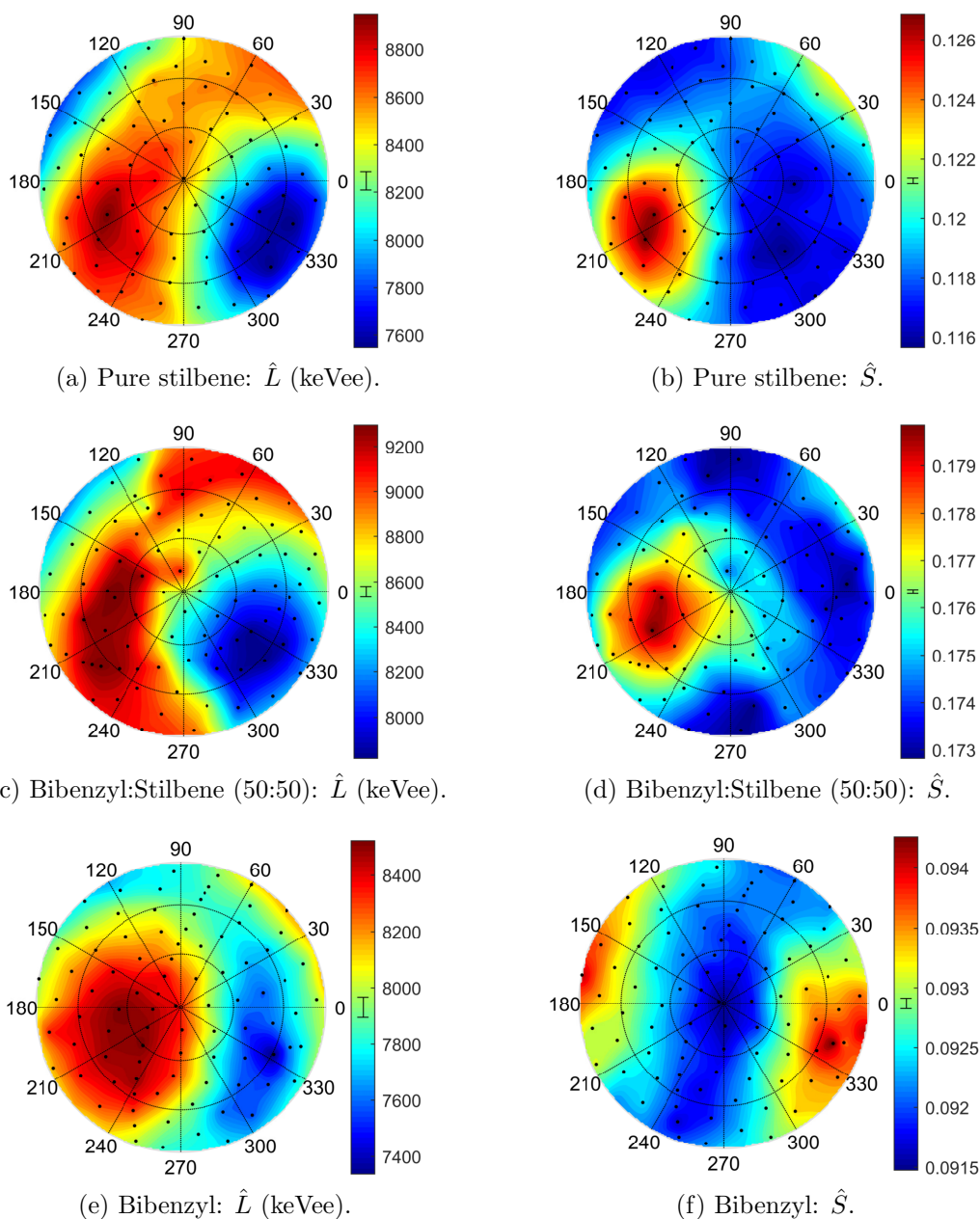


Figure 6.18: Response of stilbene and bibenzyl crystals at various recoil directions to 14.1 MeV protons. See Fig. 4.4 caption for a detailed explanation of the anisotropy plots.

Table 6.9: Magnitude of change in \hat{L} and \hat{S} values measured for 14.1 MeV proton recoil events in pure stilbene (using stilbene 316B from Sec. 6.1.2), pure bibenzyl, and a (50:50) BB:Stil mixed detector.

	A_L	A_S
Stilbene	1.191 ± 0.008	1.100 ± 0.001
Bibenzyl:Stilbene (50:50)	1.193 ± 0.005	1.042 ± 0.003
Bibenzyl	1.161 ± 0.008	1.032 ± 0.001

6.3.3 Measurements and Preliminary Results with DPAC:Stilbene

Unfortunately, the measurements of the mixed DPAC:Stilbene samples are again limited by the light output resolution of the DPAC materials. Additionally, it appears that the measurements made with the mixed DPAC detectors were subject to over 2°C change in the ambient room temperature, which is enough to introduce temperature effects on the order of the directional dependence. If a characterization of the relationship between the light output and pulse shape vs. temperature could be performed, the temperature dependence could be removed from the measurements to produce a more conclusive directional characterization.

Figure 6.19 shows the light output, pulse shape parameter, and average room temperature as a function of angle for these materials. The stilbene measurements do not seem to show any strong dependence on temperature. The DPAC:Stil (80:20) material does show a strong relationship between the light output and temperature. The high features in the light output distribution at approximately $\phi = 135^\circ$ correspond to high features in the temperature distribution. The pulse shape distribution, however, does not seem to show a temperature dependence.

One interesting finding about the temperature dependence is that in the DPAC:Stil (80:20) material, high temperatures seem to correlate to high light output values. But in the pure DPAC material, high temperatures seem to correlate to low light outputs. This conclusion is not very robust and is limited by statistics. Also, since there is no controlled temperature study, all of the directional measurements combine variability introduced by the temperature effects and the directional dependence, and it is impossible to separate the two or determine which factor is responsible for the observed variability.

One qualitative feature that may be observed in the pulse shape distribution is that the overall shape of the pulse shape distribution for the mixed sample looks closer to that of the pure DPAC than of the pure stilbene. Pure stilbene has a very wide region of low S values and a very sharp narrow peak. The mixed sample and pure DPAC both have more evenly distributed high and low features, each taking roughly the same solid angle from the whole distribution. This is not entirely conclusive, as temperature effects may be sculpting the shape in the pure DPAC and mixed DPAC:stilbene materials.

While nothing can really be concluded from the light output anisotropy, the magnitude of change in the pulse shape distribution can be calculated. Table 6.10 shows the magnitude of

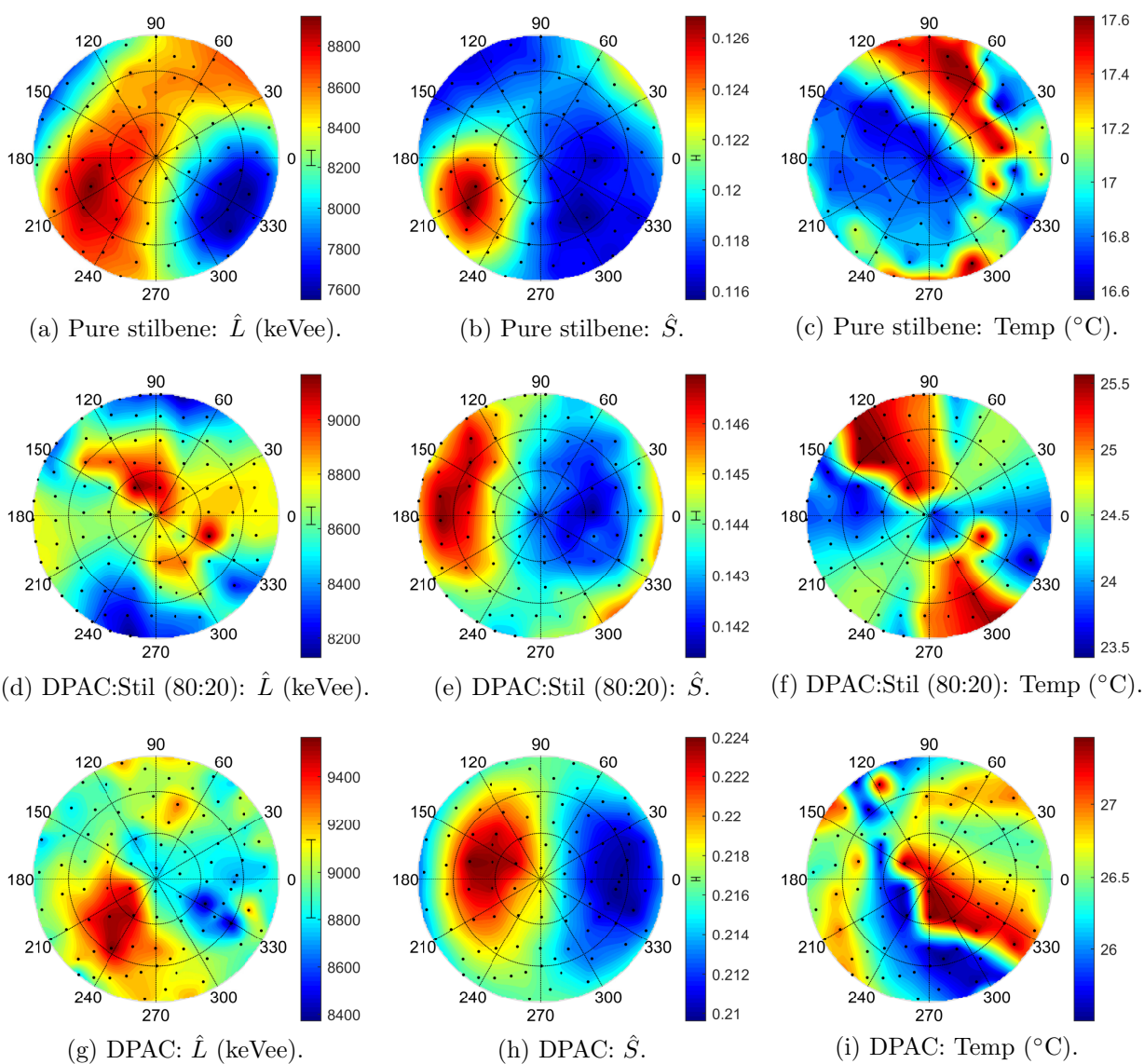


Figure 6.19: (a-b, d-e, g-h) Response of stilbene and DPAC crystals at various recoil directions to 14.1 MeV protons and (c, f, i) approximate room temperature during measurements. See Fig. 4.4 caption for a detailed explanation of the anisotropy plots.

the pulse shape anisotropy for these measurements. Interestingly, A_S for the mixed sample does not fall between the A_S values for the pure DPAC and pure stilbene materials. Instead it is much lower, almost exactly the same as the A_S value for the mixed BB:Stil sample measured in the previous section. This may be an indication that the A_S value is dependent on the stilbene population. It is possible that the spatial distribution of stilbene molecules is approximately the same between the BB:Stil and DPAC:Stil mixed crystals, producing

approximately the same pulse shape anisotropy.

Table 6.10: Magnitude of change in \hat{S} values measured for 14.1 MeV proton recoil events in pure stilbene (using stilbene 316B from Sec. 6.1.2), pure DPAC, and an (80:20) DPAC:Stil mixed detector.

	A_S
Stilbene	1.100 ± 0.001
DPAC:Stil (80:20)	1.041 ± 0.001
DPAC	1.070 ± 0.001

6.3.4 Interpretation of Mixed Material Results and Update to Hypothesis

While the scintillation mechanism in these mixed materials is not understood, a strong hypothesis was presented by Zaitseva *et al.* [41]. Their assessment was that stilbene is the scintillating agent in the DPAC:Stil mixtures because the band gap is lower for stilbene than for DPAC. When stilbene is present at very low concentrations, the impurity stilbene acts as a trap for both singlet and triplet excitations of the host. The stilbene traps prevent triplet energy migration and annihilation needed for the formation of delayed light in DPAC crystals containing stilbene in small concentrations. For this reason, there is no neutron-gamma PSD, and the delayed light in all events is lower than in pure DPAC or pure stilbene.

As the concentration of stilbene increases, the sudden reappearance of the delayed light corresponds to a restored exciton mobility. Once the density of stilbene molecules reaches a certain threshold, the stilbene no longer acts as a trap and the triplet excited states can then reach each other to incur the triplet-triplet annihilation and generate delayed fluorescence. As the stilbene concentration continues to rise, high stilbene density leads to stilbene network formation, resulting in higher PSD.

Although Zaitseva *et al.* do not mention singlet quenching, it should be considered in their hypothesis. Zaitseva *et al.* observed that the relative light yield decreases linearly with stilbene concentration in the mixed crystal [41]. This is likely dominated by the steady increase in singlet quenching as the stilbene concentration increases. This can not be explained by triplet-triplet annihilation, which would increase and contribute more delayed light as the stilbene concentration increases.

Considering the scintillation anisotropy, the results presented here suggest that the stilbene network within the mixed material is responsible for the scintillation, but it does not behave the same as a pure stilbene network. Considering that the magnitude of the pulse shape anisotropy is roughly the same in the BB:Stil (50:50) and DPAC:Stil (80:20), it is possible that the stilbene network dictates the magnitude of the effect. The shape of the pulse shape anisotropy is not as definitive. In the BB:stil mixed sample, the shape of the pulse shape anisotropy was very close to that of the pure stilbene sample. In the DPAC:Stil

mixed sample, however, the shape of the pulse shape anisotropy is much closer to that of the pure DPAC sample. Thus, it does not appear that the scintillation anisotropy relies only on stilbene and is independent of the host material.

6.3.5 Further Analysis

These materials are very interesting, and further analysis should be done with them. Most importantly, a temperature characterization should be performed so that temperature effects may be corrected for. This is particularly important for the samples with dilute stilbene, whose directional dependence appears to be dominated by a temperature dependence. Correcting for that temperature dependence may unveil a scintillation anisotropy or provide experimental evidence that no scintillation anisotropy is observed. Also, further work should be done to improve the fitting of the DPAC and mixed DPAC:Stil light output spectra. If it is not possible to improve the fit function, perhaps a very long measurement would provide enough statistics to minimize uncertainty.

Chapter 7

Conclusions

The following sections summarize the work performed in this dissertation to characterize and understand the scintillation anisotropy in organic crystal scintillator detectors. Sec. 7.1 summarizes the measurements performed including a discussion of qualitative and quantitative observations. Sec. 7.2 discusses the interpretation of the experimental results in order to update the hypothesis of what physical mechanisms are responsible for the scintillation anisotropy effect. This work has raised many new questions, and much work remains to fully understand these materials. Sec. 7.3 presents several opportunities for future work.

7.1 Summary of Anisotropy Observations

This dissertation presented several studies that experimentally characterized the scintillation anisotropy in organic crystal scintillator detectors. In Chap. 4, the scintillation anisotropy in crystalline anthracene was measured for proton recoils produced by neutrons, electron recoils produced by gamma rays, and cosmic muons. The light output and pulse shape anisotropy was characterized for a full hemisphere of proton recoil directions at 14.1 MeV and 2.5 MeV, two energies that were previously not available in the literature. The directional light output and pulse shape parameter distributions each showed qualitative features that are expected for effects due to crystal structure: broad maximal, minimal, and saddle points regions roughly 90° apart with smooth contours between. These measurements confirmed previous statements that regions of highest light output corresponded to regions of lowest pulse shape parameter, and *visa versa*. The magnitude of change in the light output across all directions, calculated as the ratio between the maximum and minimum values, was found to be $A_L = 1.155 \pm 0.006$ for 14.1 MeV proton recoils and $A_L = 1.383 \pm 0.023$ for 2.5 MeV proton recoils. These values agree with previous measurements and the trend that the magnitude of change in the light output decreases as the proton recoil energy increases. The magnitude of change in the pulse shape anisotropy was calculated as $A_S = 1.798 \pm 0.006$ at 14.1 MeV and $A_S = 1.307 \pm 0.005$ at 2.5 MeV. While no metrics comparable to A_S were provided in the literature, these measurements agree with Brooks and Jones' findings that the pulse

shape anisotropy increases as the proton recoil energy increases [7].

Measurements of 478 keV electron recoils produced by gamma-ray interactions provided quantitative and qualitative evidence that no scintillation anisotropy is present for electron recoil events. This claim was made in previous literature, but no measurements were available to support it. The directional light output and pulse shape parameter distributions did not show the qualitative features that would be expected for an effect correlated to crystal structure. Instead, the directional response showed random variations consistent with statistical and other systematic effects. Since it remains possible that a directional dependence remains at a level smaller than can be measured by this system, these measurements set an upper limit on the magnitude of the anisotropy from 478 keV electron recoils. These measurements limit the anisotropy effect for 478 keV electron recoil events to less than one tenth of that for the 14.1 MeV and 2.5 MeV proton recoil interactions.

Lastly, Chap. 4 provided measurements of cosmic muon events in anthracene. This was done to test the hypothesis for why no scintillation anisotropy is present for electron recoil events. Previous authors hypothesized that the lack of anisotropy was due to the non-straight path of the electron recoil [7], but it was also possible that the low dE/dx of the electron recoil relative to that of the proton recoil was responsible. Muons, which deposit energy in a straight path with low dE/dx , provided a test of this hypothesis. Measurements were made of cosmic muons at two angles in anthracene that showed significantly different light output and pulse shape parameters for proton recoil events. No statistically significant difference was seen in the light output or pulse shape parameter measured for cosmic muon events, producing the conclusion that no scintillation anisotropy was observed for cosmic muon events. It remains possible that an anisotropy smaller than that measurable by this system exists, so these measurements can serve to set an upper boundary on the magnitude of the scintillation anisotropy for cosmic muon events at these two directions in anthracene. To $1-\sigma$, these measurements are inconsistent with a light output anisotropy A_L greater than 1.013 and a pulse shape anisotropy A_S greater than 1.030.

In Chap. 5, amorphous liquid and plastic scintillator materials were measured to confirm that no scintillation anisotropy was present in their response. Previous authors had stated this claim, but no measurements were published to support it. Additionally, numerous experts responded to the results from the anthracene measurements by stating that the scintillation anisotropy could be an external effect on the measurement system. The measurements of liquid and plastic scintillator materials both lacked qualitative and quantitative features consistent with a scintillation anisotropy. Since no directional variability correlated to detector orientation was observed in these amorphous materials, it was concluded that the directional dependence in crystalline materials is in fact due to an internal effect requiring an ordered molecular or crystal structure and not produced by the measurement system or external factors.

In Chap. 6, several studies were performed on various pure and mixed crystals. The first study was of four stilbene materials of different size, shape, and growth method. With the rise in popularity of solution-grown stilbene, it is important to understand how the directional dependence may vary across samples. The qualitative features on the directional light output

and pulse shape parameter distributions for all four materials were the same, with regions of highest light output corresponding to highest pulse shape parameter—opposite that of anthracene. Two of the solution-grown stilbene samples had known crystal axes directions, which allowed for the scintillation anisotropy to be correlated to the crystal axes directions, confirming previous statements that the maximum light output occurs for proton recoil events along the b -axis and minimum light output occurs for proton recoil events along the c' -axis. The magnitude of the light output and pulse shape anisotropy was comparable across all four samples for both 14.1 MeV and 2.5 MeV proton recoil events, indicating that the scintillation anisotropy is not strongly impacted by the crystal geometry, size, or growth method. This is contrary to many users' predictions that the scintillation anisotropy would be significantly different between solution-grown and melt-grown materials.

A comparison of the scintillation anisotropy across five pure materials was also presented in Chap. 6: anthracene, stilbene, p-terphenyl, diphenylacetylene (DPAC), and bibenzyl (BB). Each of these materials has different molecular and crystal structure, producing different scintillation properties. The first result of the varied scintillation properties was observed in the optimization of the timing windows for the pulse shape parameter calculation. The step sizes for defining the boundaries of the delayed timing window, Δ_1 and Δ_2 , varied greatly across materials. The shortest time window, for instance, ranged from $\Delta_1 = 3$ in DPAC to $\Delta_1 = 60$ in anthracene. The scintillation anisotropy varied both quantitatively and qualitatively across all materials. While the magnitude of the light output anisotropy for 14.1 MeV proton recoils spanned a narrow range from approximately 1.15-1.20, the magnitude of the pulse shape anisotropy varied greatly from the smallest in DPAC of $A_S \approx 1.03$ to the largest in anthracene of $A_S \approx 1.80$.

The qualitative features on the directional light output and pulse shape parameter distributions varied greatly between materials. The relationship between the light output and pulse shape as a function of proton recoil direction differed greatly. In anthracene and BB, the direction of maximal light output corresponded to the direction of minimal pulse shape parameter, and *visa versa*, while only the saddle point in the two distributions was aligned or “in sync”. In stilbene, however, the maximal, minimal, and saddle points features were all in sync between the two distributions. P-terphenyl proved different still with no features in sync. Unfortunately, the relationship between the light output and pulse shape anisotropies in DPAC remains unclear because the light output resolution in DPAC is very poor, making the light output anisotropy measurement challenging and in this case inconclusive.

The last set of measurements presented in Chap. 6 was a comparison of the scintillation anisotropy across a set of mixed BB:stilbene and DPAC:stilbene crystals with varying stilbene concentrations. These materials have been produced in the last decade, and their scintillation mechanism is not well understood. The measurements of the mixed BB:stilbene samples showed that the (50:50) BB:stilbene had the same relationship between the light output and pulse shape anisotropies as is present in pure stilbene in which the maximum, minimum, and saddle point features are in the same locations in the light output and pulse shape distributions. The mixed material was also similar to stilbene in that its light output anisotropy ($A_L \approx 1.19$) was closer to that in pure stilbene ($A_L \approx 1.19$) than in pure

BB ($A_L \approx 1.16$). The pulse shape anisotropy, however, ($A_S \approx 1.03$) was closer to that in BB ($A_S \approx 1.04$) than in stilbene ($A_S \approx 1.10$). This was first interpreted as meaning that the scintillation may be more strongly dependent on stilbene, especially for singlet excitations, with some influence from bibenzyl. Measurements of the (80:20) DPAC:stilbene mixed crystal were limited because the light output resolution was so poor that it was difficult to calculate the expected light output at each direction. This is similar to the pure DPAC material. The pulse shape resolution, on the other hand, was very good, allowing for a high quality measurement of the pulse shape parameter as a function of direction. The shape of the directional pulse shape distribution was closer to that of pure DPAC than pure stilbene, but the magnitude of change in the pulse shape parameter ($A_S \approx 1.04$) was much lower than that for the pure DPAC ($A_S \approx 1.07$) and pure stilbene ($A_S \approx 1.10$). Since the magnitude of the pulse shape anisotropy was approximately the same for the (50:50) BB:stilbene and the (80:20) DPAC:stilbene, a refined hypothesis is that the stilbene network within the mixed material is responsible for the scintillation, but it does not behave the same as a pure stilbene network because the density of stilbene molecules is less in the mixed material than in the pure stilbene.

7.2 Current State of Scintillation Anisotropy Hypothesis

Prior to this dissertation, the leading hypothesis for why there exists a scintillation anisotropy in organic crystal scintillators was that there are preferred directions of excitation transport. Depending on the initial distribution of excitations with respect to those preferred directions, the density of excitations will change over time, changing the likelihood of interactive kinetic processes that will change the light emission. Previously, no distinction was made between singlet and triplet transport. This remains the leading hypothesis, but this dissertation has updated it to provide more specific details about the effect.

One question that remained before this work was why there is no scintillation anisotropy for electron recoil events generated by gamma-ray interactions. Brooks and Jones hypothesized that it was because the electron recoil does not travel in a straight path as it deposits its energy, so the spatial distribution of excitations is approximately the same for all initial electron recoil directions [7]. Measurements of cosmic muon events in Chap. 4, however, showed that this is not the reason. Proton recoils, which exhibit a directional dependence, interact with a high dE/dx in a straight path. Electron recoils, which do not exhibit a directional dependence, interact with a low dE/dx in a non-straight path. Muons interact with low dE/dx in a straight path, and were measured in this work and showed no directional dependence. Thus, the lack of scintillation anisotropy in the electron recoil is not due to its non-straight path, but rather due to its low dE/dx . This contributes a new finding to the theory of the scintillation anisotropy that it is only produced by high dE/dx interactions, which fits into the hypothesis of preferred directions of excitation transport. For heavy

charged particles that interact with high dE/dx , the change in the excitation density due to preferred directions of excitation transport in different directions is significant compared to the overall density. For gamma-ray and muon interactions, the overall excitation density is low enough due to their low dE/dx that these changes are not significant enough to change the scintillation output on an observable level.

The comparison of the scintillation anisotropy in five pure materials in Chap. 6 demonstrated that the relationship between the light output and pulse shape anisotropy varies across materials. This suggests that the preferred directions of excitation transport for singlet and triplet excitations may not be the same, a concept that was not part of the hypothesis prior to this dissertation. In the case that the preferred directions are the same for singlets and triplets, the proton recoil direction that produced the highest excitation densities produced higher rates of singlet quenching and triplet-triplet annihilation, so a decrease in prompt light due to more singlet quenching was accompanied by an increase in delayed light due to more triplet-triplet annihilation. This appears to be the case in anthracene. If the directions of preferred transport for singlet and triplets are different, however, a lower singlet density may be accompanied instead by a higher triplet density, changing the relationship between the relative rates of singlet quenching and triplet-triplet annihilation. This presents the possibility for the maximum light output to correspond to the maximum pulse shape parameter, as is observed in stilbene. The relationship in p-terphenyl, in which the maxima, minima, and saddle points of each distribution are out of sync, can be accounted for by considering that there are three dimensions in the crystal axes. Rather than the directions of maximum and minimum transport for triplets and singlets either being the same or opposite, there could be the case in which the direction of maximum singlet transport is the direction of medium triplet transport. This introduces, for example, the possibility that the saddle point in the light output distribution corresponds to the maximum or minimum in the pulse shape distribution.

The scintillation anisotropy provides a unique method for learning about the scintillation mechanism of mixed crystals, which is largely unknown. Since stilbene's bandgap energy is less than that of BB or DPAC, it follows that excitations would transfer their energy to nearby stilbene molecules and stilbene would be the scintillating agent. At very low stilbene concentrations, where there is no delayed light observed and therefore the pulse shape of gamma-ray events is the same as for neutron events, Zeitseva *et al.* hypothesized that the stilbene molecules serve as traps to excitations because they are far enough apart to prevent excitation hopping to neighboring stilbene molecules [41]. This is consistent with the measurement made in Chap. 6 in which the materials with dilute stilbene components showed no scintillation anisotropy because there is no excitation transport at all due to the stilbene trapping. This is consistent, then, with the hypothesis that preferred directions of excitation transport are responsible for the scintillation anisotropy, and also updates the hypothesis such that the scintillation anisotropy requires a high density of mobile excitations with preferred directions of transport. When no transport is possible, no scintillation anisotropy is present.

The observations of the scintillation anisotropy in the mixed materials with higher stil-

bene concentrations are consistent with the claim that stilbene is the scintillating agent and forms a network within the mixed crystal [41]. The scintillation anisotropy measurements indicate that the network does not behave the same as a pure stilbene network, which is reasonable as the stilbene density in the mixed material is less than in pure stilbene. This supports the part of the hypothesis for the scintillation anisotropy that says it depends on the density of excitations. While there are many interesting observations that present new questions about the scintillation mechanism in the mixed materials, ultimately they are consistent with the current status of the hypothesis that states that the effect is due to preferred directions of excitation transport and is only present for high dE/dx materials with fixed repeating structure.

7.3 Future Work

There are several additional analyses that could be performed on the data already available from this dissertation. The scintillation anisotropy was analyzed in the context of total light output L and pulse shape parameter S for each event. Another way to analyze the data would be in terms of the total prompt and delayed components of the light output. While the light output L is the sum of these, and the pulse shape parameter S is a mathematical operation of these, the trends in the prompt and delayed light are not adequately represented by studying L and S alone. For instance, it is assumed that the light output L is dominated by the prompt light component, which is primarily due to singlet excitation prompt fluorescence. This dissertation assumes, then, that the light output anisotropy is dominated by the anisotropy in singlet prompt fluorescence, but looking at the anisotropy in the prompt and delayed components separately could identify cases when the assumption does not hold true. The light output anisotropy is a sum of the scintillation anisotropies from the prompt and delayed components, which are approximately due to light emission from singlet and triplet excitations, respectively. Even though the singlet light emission dominates the total light output, the light output anisotropy depends on the absolute change in the singlet and triplet light emission. It is possible that the singlet light emission does not change as much as the triplet light emission. Studying the prompt and delayed light emission components would identify that.

Another study that could be performed on the presently available data would be to apply a temperature correction to the data. For most materials, the temperature dependence was not measured because no climate controlled facility was available, but if the relationship between light output L and pulse shape S vs. temperature were measured, the temperature dependence could be removed from the directional measurements for more precise results. Also, the measurements of the dilute stilbene mixed crystals exhibited heavy temperature dependence, so it was concluded that no scintillation anisotropy was observed, but it is possible that a much smaller scintillation anisotropy exists that could be observed if the temperature effects were corrected for.

The measurements performed in this work serve as a resource to groups who aim to

account for the scintillation anisotropy or employ it as a directional detection modality. As stilbene grows in popularity, it is important for users to understand how the scintillation anisotropy affects their measurements. For static measurements in which the source and detector are in known locations, users may orient the detector with respect to the source in order to achieve optimal light output and PSD. For users who wish to design a directional detection system, the scintillation anisotropy measurements provided in this dissertation will assist them in choosing the best crystalline material and predicting the performance of their system.

The comparison of the scintillation anisotropy across four stilbene materials with different size, geometry, and growth method in Sec. 6.1 raises the question of how the effect depends on impurities and other crystal imperfections. For materials groups who aim to modify the effect for a given application, it may be possible to achieve desired characteristics by introducing changes in the material quality. The measurements of the mixed crystals showed that the scintillation anisotropy differs when the scintillating agent, presumed to be stilbene, exists in a different physical structure with a lower density. This implies that it is possible to manipulate the scintillation anisotropy by changing the crystal structure or physical arrangement of scintillating molecules.

The next level of analysis on this effect lies in understanding what physical properties dictate the magnitude and behavior of the scintillation anisotropy in a given material. For example, what is different about anthracene that causes it to have such a greater pulse shape anisotropy than the rest of the materials? These questions indicate the need for collaboration with experts in physical chemistry and excitonics. Is it possible to determine what the preferred directions of singlet and triplet excitation transport are in different materials? It is likely not as simple as just looking at the molecular or crystal structure, but experimental or quantitative methods may exist. For singlet excitations, their interactive processes are longer range than triplet interactive processes, so the preferred directions of transport depend on bulk properties. It may be possible to determine the preferred direction of singlet transport by measuring the photoconductivity across a bulk material in different directions. Triplet interactive processes are shorter range, so the transport is more related to local crystal and electronic structure of a molecule. Optical measurement techniques such as time-resolved microscopy may be used to image triplet transport as a function of direction, as was performed on tetracene by Akselrod *et al.* [31]. These techniques are very challenging, so collaborating with experts who can assist in performing those techniques would be ideal. Computational methods such as kinetic Monte Carlo may be useful for modeling the dynamics of excitations produced by a radiation interaction, and the measurements produced in this dissertation may be used to validate such a model.

Studying the scintillation anisotropy offers potential new findings on broader characteristics of organic scintillators. The scintillation anisotropy is a signature of the internal energy transfer processes in these organic crystal scintillator materials, and further studies may help develop an underlying model or theory that can describe and predict observations.

Appendix A

MCNP5 Simulation of ^{137}Cs on Anthracene

A.1 Calculating Energy Deposited with MCNP5

In order to build a fit function for locating L_{478} in a light output spectrum measured from ^{137}Cs interactions on anthracene, MCNP5 was used to produce a simulated detector response.

A simple simulation was built consisting of a ^{137}Cs source directed toward a cylindrical anthracene detector of height 1.5 cm and radius 1.25 cm. The source was placed 100 cm away from the anthracene detector, and a wooden plank and aluminum shelf were added above and below the space between the source and detector to provide some environmental scattering materials to better capture laboratory conditions. The code for the MCNP5 simulation is provided below.

```

Experimental setup Patricia Schuster , 2014.06.25
c CELL CARDS ccccccccccccccccccccccccccccccccccccccccccccccccccccccc
c
c Detector cell: anthracene
1005 2 -1.23 -105 imp:P=1
c Wooden table , top tier
2001 3 -0.64 -201 imp:P=1
c Aluminum shelf above
2002 4 -2.73 -202 imp:P=1
c Solution space giant box
9998 0 -999 105 201 202 imp:P=1
c Outside of everything cell
9999 0 999 imp:P=0
c END CELL CARDS - BLANK LINE FOLLOWS ccccccccccccccccccccccccccccccc

c SURFACE CARDS ccccccccccccccccccccccccccccccccccccccccccccccccccccc
c Detector cylinder
105 RCC 100 0 0 1.5 0 0 1.25
c Wooden table , top tier
201 RPP 0 100 -10 10 -33 -30
c Aluminum shelf above
202 RPP 0 100 -10 10 30 33
c Giant box outside of everything
999 BOX -100 -100 -100 300 0 0 0 200 0 0 0 200
c END SURFACE CARDS - BLANK LINE FOLLOWS ccccccccccccccccccccccccccccccc

```

```

c DATA CARDS ccccccccccccccccccccccccccccccccccccccccccccccccccccccccc
mode p e
nps 1.0E11
c ccccccccccccccccccccccccccccccccccccccccccccccccccccccccccccccccc
c
c SOURCE SPECIFICATION cccccccccccccccccccccccccccccccccccccccccccccccc
c Cs-137 source, isotropic from behind the collimator
sdef POS=0 0 0 ERG=0.662 PAR=P VEC=1 0 0 DIR=D1
sil -1 0.9806 1
sp1 0 0.9903 0.0097
sb1 0 0 1
c ccccccccccccccccccccccccccccccccccccccccccccccccccccccccccccccccc
c
PRINT 110
c
c MATERIAL SPECIFICATION cccccccccccccccccccccccccccccccccccccccccccccccc
c Anthracene
m2 PLIB=04p
    1000 0.416667
    6000 0.583333
c Wood benches
m3 PLIB=04p
    1001 0.462423
    6000 0.323389
    7014 0.002773
    8016 0.208779
    12000 0.000639
    16000 0.001211
    19000 0.000397
    20000 0.000388
c Aluminum shelf above
m4 PLIB=04p
    13000 0.987924
    14000 0.003220
    25000 0.006198
    26000 0.001893
    29000 0.000536
    30000 0.000229
c ccccccccccccccccccccccccccccccccccccccccccccccccccccccccccccccccc
c
c TALLY SPECIFICATION cccccccccccccccccccccccccccccccccccccccccccccccc
c Energy deposited in the detector
F106:P 1005
E106 0.01 98i 1.0
c Pulse height tally
F108:P 1005
E108 0.01 98i 1.0
c ccccccccccccccccccccccccccccccccccccccccccccccccccccccccccccccccc
c END OF FILE

```

This simulation is simple and neglects numerous other materials present in the measurement such as the photomultiplier tube, rotational stage, electronics rack, air, and many other things. Since additional scatter from these other materials would contribute lower energy gamma rays and the goal of this simulation is to locate the position of the Compton edge, this was considered an acceptable approximation. Figure A.1 shows a visualization of the simulation in VisEd.

An F8 tally, shown in Fig. A.2, was used to produce a discrete pulse height distribution with 10 keV bins in the anthracene cell. This distribution shows that there is a distinct drop

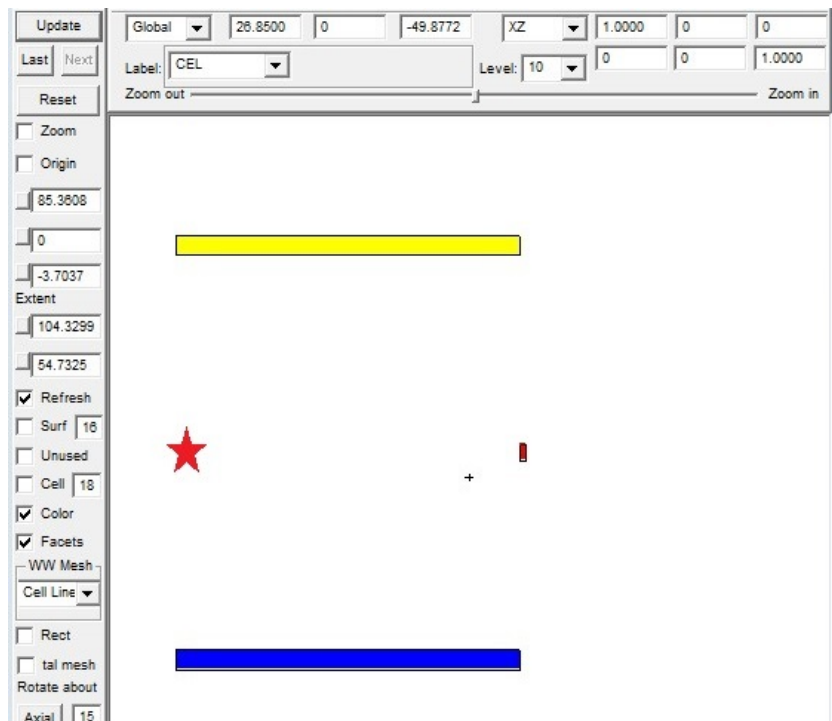


Figure A.1: Visualization of MCNP5 simulation in VisEd. The yellow box is the aluminum shelf, the blue box is the wooden shelf, the right square on the right is the anthracene detector, and the red star indicates the location of the ^{137}Cs source.

off at the Compton edge, but events do occur above E_{CE} . Since a single scatter interaction can only deposit energy up to E_{CE} , as described in Sec. 2.1.2, any event that produces a pulse height above E_{CE} is a multiple scatter event in which a gamma ray interacts two or more times in the anthracene material and the energies deposited sum to be greater than E_{CE} .

A.2 Incorporating Detector Resolution

In order to estimate a realistic detector response from this F8 tally, the distribution is smeared by a Gaussian resolution term as a first-order approximation to the detector response. When a detector measures a monoenergetic source, its response may fluctuate from event to event even though the same amount of energy was deposited in each event. There are numerous sources of fluctuation in the measured energy including statistical fluctuations and electronic noise. Generally, the distribution of measured energies, known as the detector's *response function*, will tend toward a Gaussian shape described by the function,

$$G(E) = \frac{1}{\sigma\sqrt{2\pi}} \exp\left(-\frac{(E - E_0)^2}{2\sigma^2}\right), \quad (\text{A.1})$$

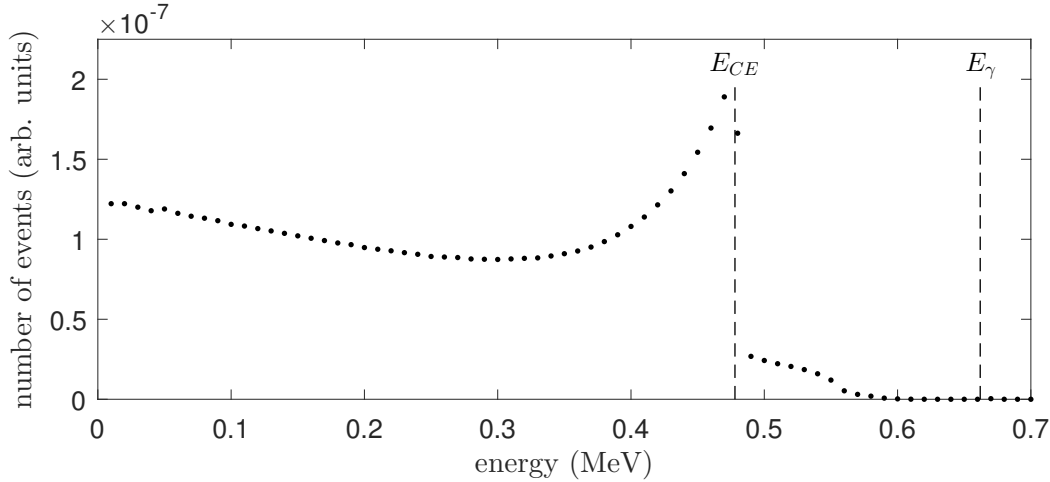


Figure A.2: F8 tally with 10 keV bins from MCNP5 simulation of ^{137}Cs incident on anthracene. Vertical dashed lines indicate the incident gamma-ray energy, $E_\gamma = 662$ keV, and the Compton edge energy, $E_{CE} = 478$ keV. The statistical errors produced by the simulation are smaller than the marker size in the plot.

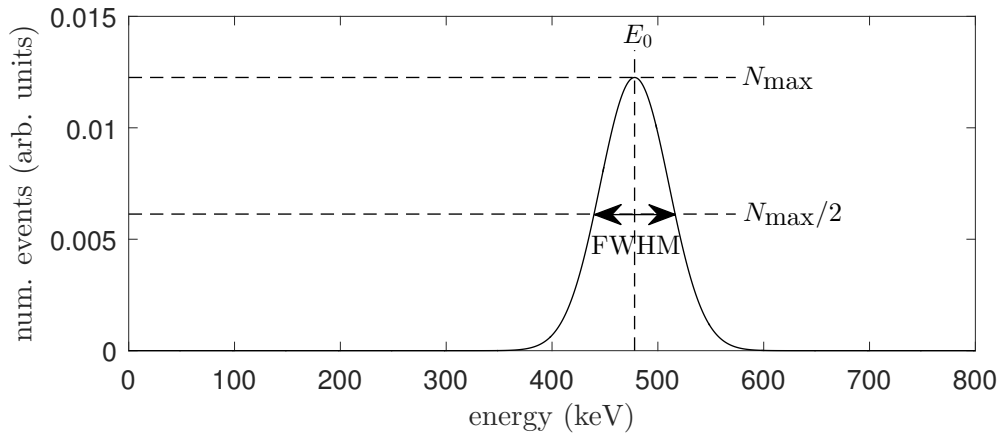


Figure A.3: Gaussian shape indicating full width at half maximum, FWHM, and peak centroid energy, E_0 . This plot corresponds to the detector response for a measurement of a monoenergetic source that deposits $E_0 = 478$ keV in a detector with resolution $R = \text{FWHM}/E_0 = 0.16 = 16\%$. Adapted from [2, ch. 4].

where E_0 is the peak centroid energy and σ is a width parameter. The resolution is often described by the full width at half maximum, FWHM, defined as the width of the distribution at a height equal to half of the peak height. The resolution, R , of a detector is defined as $R = \text{FWHM}/E_0$, often expressed as a percentage. Figure A.3 shows a detector response for a detector with resolution $R = 16\%$ measuring a source that deposits 478 keV per event.

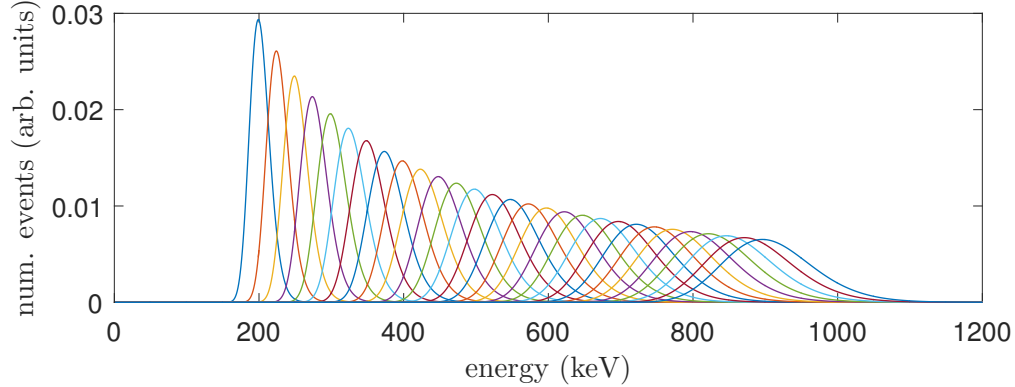


Figure A.4: Gaussian resolution function $G(E)$ for centroid energies E_0 from 200 keV to 900 keV deposited in a detector with resolution $R = 16\%$.

Similarly, the FWHM and width parameter σ will vary as a function of centroid energy E_0 . Although there are several terms that impact the resolution, a simple model that neglects several terms and assumes a fixed fractional resolution is as follows:

$$\begin{aligned} \text{FWHM}(E) &= R \cdot E \\ \sigma(E) &= \frac{\text{FWHM}}{2\sqrt{2 \ln 2}} = \frac{R \cdot E}{2\sqrt{2 \ln 2}} \end{aligned} \quad (\text{A.2})$$

Combining Eq. (A.1) and Eq. (A.2), the Gaussian smearing curve as a function of energy may be expressed as:

$$\begin{aligned} G(E) &= \frac{1}{\sigma(E)\sqrt{2\pi}} \exp\left(-\frac{(E - E_0)^2}{2\sigma(E)^2}\right) \\ G(E) &= \frac{1}{\left(\frac{R \cdot E}{2\sqrt{2 \ln 2}}\right)\sqrt{2\pi}} \exp\left(-\frac{(E - E_0)^2}{2\left(\frac{R \cdot E}{2\sqrt{2 \ln 2}}\right)^2}\right) \\ G(E) &= \frac{2\sqrt{\ln 2}}{(R \cdot E)\sqrt{\pi}} \exp\left(-\frac{4 \cdot 2 \ln 2 (E - E_0)^2}{2(R \cdot E)^2}\right) \\ G(E) &= \frac{2\sqrt{\ln 2}}{(R \cdot E)\sqrt{\pi}} \exp\left(-\frac{4 \ln 2 (E - E_0)^2}{(R \cdot E)^2}\right) \end{aligned} \quad (\text{A.3})$$

To illustrate this, the response functions for a detector with resolution $R = 16\%$ at different centroid energies E_0 from 200 keV to 900 keV are shown in Fig. A.4.

Since the width of the detector response depends on the energy of the interacting gamma ray, the Gaussian function used in the smearing must vary in its width as a function of energy as given in Eq. (A.3). The following MATLAB function will produce a smeared spectrum from the MCNP5 F8 tally and a resolution value R .

```

function smeared = GaussianESmear(E,tally ,R)
% Convolve a Gaussian resolution function with a detector response from MCNP
% The Gaussian width is proportional to the energy

% Inputs:
% tally vs. energy (MeV) straight from MCNP output
% R is detector resolution in %. R(%) = FWHM / E0

% Check that energy and tally are the same size
if size(E) ~= size(tally)
    error('Energy and tally must be same size vectors')
end;

smeared = zeros(size(tally));
for i = 1:length(E)
    E0 = E(i);
    G = 2*sqrt(log(2))./(R*E*sqrt(pi)).*exp(-4*log(2)*(E-E0).^2./((R*E).^2));
    smeared = smeared + tally(i)*G;
end
end

```

A.3 Aligning Simulated and Measured Light Output Distributions

Figure A.5 shows the measured light output distribution from ^{137}Cs interactions on anthracene and the smeared pulse shape distribution as calculated from the MCNP5 simulation. With $R = 16\%$, the shapes of the Compton edges match between the two distributions. The two distributions do not agree at lower energies because the simulation does not include numerous sources of environmental scatter that exist in the laboratory and contribute lower energy gamma rays, as described earlier. Also, the fixed fractional resolution is a simplification that neglects several terms that determine the resolution at a given energy. Since the MCNP5 results are in units of energy, one can determine the position of the feature that corresponds to 478 keV in the simulated distribution relative to the peak feature. This feature lands at a count amplitude relative to the peak of $N_{478}/N_{\text{peak}} = 0.74$. This relationship can be used to calibrate measured distributions by locating the light output L_{478} in ICPU units at $N_{478} = 0.74N_{\text{peak}}$ counts and calculating C from Eq. (3.4).

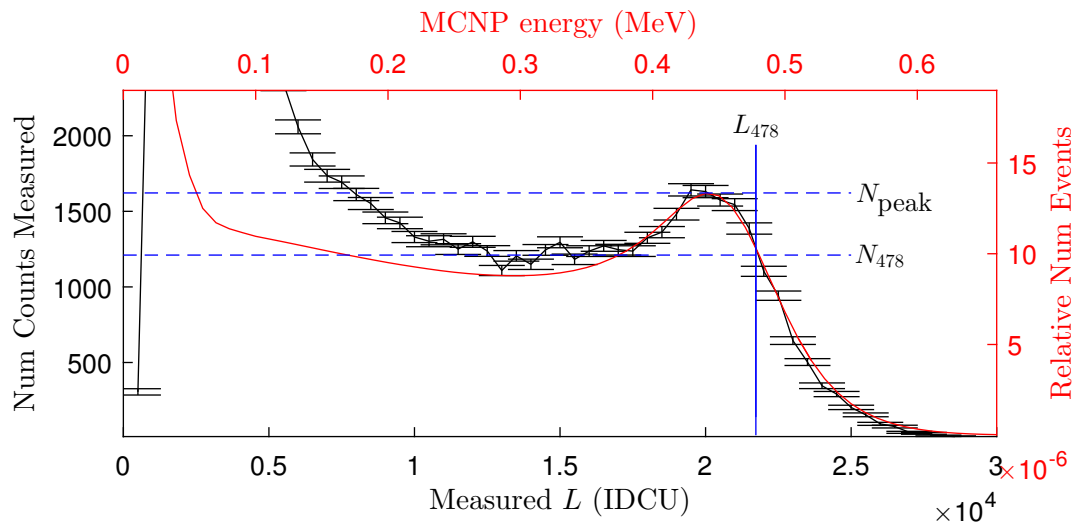


Figure A.5: Light output spectrum for ^{137}Cs gamma-ray events incident on anthracene. The solid curve, upper and right axes correspond to an MCNP5 simulation. The data points, lower and left axes correspond to a background-subtracted measurement. Lines indicate the positions of N_{peak} , N_{478} and L_{478} .

Bibliography

- [1] Natalia Zaitseva et al. “Plastic scintillators with efficient neutron/gamma pulse shape discrimination”. In: *Nuclear Instruments and Methods in Physics Research Section A: Accelerators, Spectrometers, Detectors and Associated Equipment* 668 (Mar. 2012), pp. 88–93. ISSN: 01689002. DOI: 10.1016/j.nima.2011.11.071. URL: <http://www.sciencedirect.com/science/article/pii/S0168900211021395>.
- [2] Glenn F. Knoll. *Radiation Detection and Measurement, Third Edition*. Wiley, 2000, p. 816. ISBN: 0471073385. URL: https://books.google.com/books/about/Radiation%7B%5C_%7DDetection%7B%5C_%7Dand%7B%5C_%7DMeasurement.html?id=HKBVAAAAMAAJ%7B%5C&%7Dpgis=1.
- [3] Leslie Carman et al. “The effect of material purity on the optical and scintillation properties of solution-grown trans-stilbene crystals”. In: *Journal of Crystal Growth* 368 (Apr. 2013), pp. 56–61. ISSN: 00220248. DOI: 10.1016/j.jcrysgr.2013.01.019. URL: <http://www.sciencedirect.com/science/article/pii/S0022024813000584>.
- [4] Natalia Zaitseva et al. “Scintillation properties of solution-grown trans-stilbene single crystals”. In: *Nuclear Instruments and Methods in Physics Research, Section A: Accelerators, Spectrometers, Detectors and Associated Equipment* 789 (2015), pp. 8–15. ISSN: 01689002. DOI: 10.1016/j.nima.2015.03.090.
- [5] M.M. Bourne et al. “Neutron detection in a high-gamma field using solution-grown stilbene”. In: *Nuclear Instruments and Methods in Physics Research Section A: Accelerators, Spectrometers, Detectors and Associated Equipment* 806 (Jan. 2016), pp. 348–355. ISSN: 01689002. DOI: 10.1016/j.nima.2015.10.025. URL: <http://www.sciencedirect.com/science/article/pii/S0168900215012322>.
- [6] Paul Henrich Heckmann. “Richtungsabhaengigkeit der Szintillations-Lichtausbeute von Anthracenkristallen beim Beschuss mit alpha-Strahlen”. In: *Zeitschrift fuer Physik* 157.2 (1959), pp. 139–148. ISSN: 0044-3328. DOI: 10.1007/BF02055746. URL: <http://link.springer.com/10.1007/BF00632300>.
- [7] F.D. Brooks and D.T.L. Jones. “Directional anisotropy in organic scintillation crystals”. In: *Nuclear Instruments and Methods* 121.1 (Oct. 1974), pp. 69–76. ISSN: 0029554X. DOI: 10.1016/0029-554X(74)90141-4. URL: <http://www.sciencedirect.com/science/article/pii/0029554X74901414>.

- [8] D. B. Oliver and G. F. Knoll. “Anisotropy of Scintillation Response of Anthracene to Neutron Generated Recoil Protons and Carbon Ions”. In: *IEEE Transactions on Nuclear Science* 15.3 (1968), pp. 122–126. ISSN: 0018-9499. DOI: 10.1109/TNS.1968.4324926. URL: <http://ieeexplore.ieee.org/lpdocs/epic03/wrapper.htm?arnumber=4324926>.
- [9] Kineo Tsukada and Shiroh Kikuchi. “Directional anisotropy in the characteristics of the organic-crystal scintillators”. In: *Nuclear Instruments and Methods* 17.3 (Dec. 1962), pp. 286–288. ISSN: 0029554X. DOI: 10.1016/0029-554X(62)90007-1. URL: <http://www.sciencedirect.com/science/article/pii/0029554X62900071>.
- [10] K. Tsukada, S. Kikuchi, and Y. Miyagawa. “Directional anisotropy in the characteristics of the organic-crystal scintillators, II”. In: *Nuclear Instruments and Methods* 37 (Nov. 1965), pp. 69–76. ISSN: 0029554X. DOI: 10.1016/0029-554X(65)90339-3. URL: <http://www.sciencedirect.com/science/article/pii/0029554X65903393>.
- [11] Paul Henrich Heckmann. “Richtungsabhaengigkeit der Szintillations-Lichtausbeute von Anthracenkristallen beim Beschuss mit alpha-Strahlen”. In: *Die Naturwissenschaften* 46.8 (1959), pp. 259–260. ISSN: 0028-1042. DOI: 10.1007/BF00632300. URL: <http://link.springer.com/10.1007/BF00632300>.
- [12] P. H. Heckmann, H. Hansen, and A. Flammersfeld. “Die Richtungsabhaengigkeit der Szintillations-Lichtausbeute von duennen Anthrazen- und Stilben-Kristallen beim Beschuss mit alpha-Strahlen”. In: *Zeitschrift fuer Physik* 162.1 (Feb. 1961), pp. 84–92. ISSN: 1434-6001. DOI: 10.1007/BF01342470. URL: <http://link.springer.com/10.1007/BF01342470>.
- [13] W. F. Kienzle and A. Flammersfeld. “Die Anisotropie der Szintillationslichtausbeute organischer Moleküleinkristalle für α -Strahlen”. In: *Zeitschrift fuer Physik* 165.1 (1961), pp. 1–11. DOI: 10.1007/BF01378080.
- [14] P. H. Heckmann, W. Sander, and A. Flammersfeld. “Die Szintillations-Anisotropie von Anthrazen bei tiefen Temperaturen”. In: *Zeitschrift fuer Physik* 165.1 (Feb. 1961), pp. 12–16. ISSN: 1434-6001. DOI: 10.1007/BF01378081. URL: <http://link.springer.com/10.1007/BF01378081>.
- [15] Erik Brubaker and John Steele. “Neutron imaging using the anisotropic response of crystalline organic scintillators”. In: *IEEE Nuclear Science Symposium Conference Record* (2010), pp. 1647–1652. ISSN: 10957863. DOI: 10.1109/NSSMIC.2010.5874055.
- [16] J B Birks. “Scintillations from Organic Crystals: Specific Fluorescence and Relative Response to Different Radiations”. In: *Proceedings of the Physical Society. Section A* 64 (1951), pp. 874–877. ISSN: 0370-1298. DOI: 10.1088/0370-1298/64/10/303.
- [17] Franz -Josef Kratochwill. “Szintillationsanisotropie von Anthrazenkristallen bei Beschuss mit alpha-Teilchen im Energiebereich 1-3 MeV”. In: *Zeitschrift fuer Physik* 234.1 (Feb. 1970), pp. 74–81. ISSN: 1434-6001. DOI: 10.1007/BF01392499. URL: <http://link.springer.com/10.1007/BF01392499>.

- [18] J.B. Birks. *The Theory and Practice of Scintillation Counting*. Oxford: Pergamon Press, 1964, pp. 39–67, 261. ISBN: 9780080104720. DOI: 10.1016/B978-0-08-010472-0.50001-X. URL: <http://www.sciencedirect.com/science/article/pii/B978008010472050001X>.
- [19] D.T.L. Jones and F.D. Brooks. “Polarization in neutron-proton scattering at 16.4 and 21.6 MeV”. In: *Nuclear Physics A* 222.1 (Apr. 1974), pp. 79–92. ISSN: 03759474. DOI: 10.1016/0375-9474(74)90585-5. URL: <http://www.sciencedirect.com/science/article/pii/0375947474905855>.
- [20] *IAEA Safeguards Glossary*. [Online] Available: https://www.iaea.org/sites/default/files/iaea_safeguards_glossary.pdf [2016, July 19]. International Nuclear Verification Series No. 3. 2001.
- [21] David N. Spergel. “Motion of the Earth and the detection of weakly interacting massive particles”. In: *Physical Review D* 37.6 (Mar. 1988), pp. 1353–1355. ISSN: 0556-2821. DOI: 10.1103/PhysRevD.37.1353. URL: <http://journals.aps.org/prd/abstract/10.1103/PhysRevD.37.1353>.
- [22] Hiroyuki Sekiya et al. “Measurements of anisotropic scintillation efficiency for carbon recoils in a stilbene crystal for dark matter detection”. In: *Physics Letters, Section B: Nuclear, Elementary Particle and High-Energy Physics* 571.3-4 (2003), pp. 132–138. ISSN: 03702693. DOI: 10.1016/j.physletb.2003.07.077. arXiv: 0307384 [astro-ph]. URL: <http://dx.doi.org/10.1016/j.physletb.2003.07.077>.
- [23] P. Belli et al. “Identifying a “dark matter” signal by nonisotropic scintillation detector”. In: *Il Nuovo Cimento C* 15.4 (July 1992), pp. 473–479. ISSN: 0390-5551. DOI: 10.1007/BF02511747. URL: <http://link.springer.com/10.1007/BF02511747>.
- [24] R Bernabei et al. “Anisotropic scintillators for WIMP direct detection: revisited”. In: *The European Physical Journal C* 28.2 (2003), pp. 203–209.
- [25] Y Shimizu et al. “Directional scintillation detector for the detection of the wind of WIMPs”. In: *Nuclear Instruments and Methods in Physics Research, Section A: Accelerators, Spectrometers, Detectors and Associated Equipment* 496.2-3 (2003), pp. 347–352. ISSN: 01689002. DOI: 10.1016/S0168-9002(02)01661-3. arXiv: 0207529 [astro-ph].
- [26] S.G. Prussin. *Nuclear physics for applications. A model approach*. English. Wiley-VCH, 2007. ISBN: 9783527407002. URL: http://inis.iaea.org/Search/search.aspx?orig%7B%5C_%7Dq=RN:38102957.
- [27] *Muons*. [Online] Available: http://cosmic.lbl.gov/SKliewer/Cosmic_Rays/Muons.htm [2016, May 4]. The Cosmic Ray Experiment, Lawrence Berkeley National Laboratory, Berkeley, CA.
- [28] J.B. Birks. *Photophysics of Aromatic Molecules*. London: John Wiley & Sons Ltd., 1970. ISBN: 0471074209.

- [29] Dwaine O. Cowan and Ronald L. Drisko. *Elements of Organic Photochemistry*. New York: Plenum Press, 1976. ISBN: 0306308215.
- [30] Tohru Azumi and Sean P. McGlynn. “Delayed Fluorescence of Solid Solutions of Polyacenes. II. Kinetic Considerations”. In: *The Journal of Chemical Physics* 39.5 (1963), p. 1186. ISSN: 00219606. DOI: 10.1063/1.1734411. URL: <http://scitation.aip.org/content/aip/journal/jcp/39/5/10.1063/1.1734411>.
- [31] Gleb M Akselrod et al. “Visualization of exciton transport in ordered and disordered molecular solids.” In: *Nature communications* 5 (2014), p. 3646. ISSN: 2041-1723. DOI: 10.1038/ncomms4646. URL: <http://www.ncbi.nlm.nih.gov/pubmed/24736470>.
- [32] K.A.A. Gamage, M.J. Joyce, and N.P. Hawkes. “A comparison of four different digital algorithms for pulse-shape discrimination in fast scintillators”. In: *Nuclear Instruments and Methods in Physics Research Section A: Accelerators, Spectrometers, Detectors and Associated Equipment* 642.1 (June 2011), pp. 78–83. ISSN: 01689002. DOI: 10.1016/j.nima.2011.03.065. URL: <http://www.sciencedirect.com/science/article/pii/S0168900211007078>.
- [33] *Thermo Scientific MP 320 Product Specifications*. [Online] Available: <http://www.thermoscientific.com/content/tfs/en/product/mp-320-neutron-generators.html> [2016, Jan 11]. Thermo Fisher Scientific Inc.
- [34] *Atomic and Nuclear Properties of Materials: Anthracene*. [Online] Available: <http://pdg.lbl.gov/2015/AtomicNuclearProperties/> [2015, Aug. 8]. Lawrence Berkeley National Laboratory, Berkeley, CA.
- [35] M.J. Berger et al. *ESTAR, PSTAR, and ASTAR: Computer Programs for Calculating Stopping-Power and Range Tables for Electrons, Protons, and Helium Ions (version 1.2.3)*. [Online] Available: <http://physics.nist.gov/Star> [2015, Aug 8]. National Institute of Standards and Technology, Gaithersburg, MD. 2005.
- [36] Patricia Schuster and Erik Brubaker. “Investigating the Anisotropic Scintillation Response in Anthracene through Neutron, Gamma-Ray, and Muon Measurements”. In: *IEEE Transactions on Nuclear Science* 63.3 (2016), pp. 1942–1954. ISSN: 0018-9499. DOI: 10.1109/TNS.2016.2542589. URL: <http://ieeexplore.ieee.org/lpdocs/epic03/wrapper.htm?arnumber=7465791>.
- [37] S.A. Pozzi, M.M. Bourne, and S.D. Clarke. “Pulse shape discrimination in the plastic scintillator EJ-299-33”. In: *Nuclear Instruments and Methods in Physics Research Section A: Accelerators, Spectrometers, Detectors and Associated Equipment* 723 (Sept. 2013), pp. 19–23. ISSN: 01689002. DOI: 10.1016/j.nima.2013.04.085. URL: <http://www.sciencedirect.com/science/article/pii/S016890021300524X>.

- [38] D. Cester et al. “Experimental tests of the new plastic scintillator with pulse shape discrimination capabilities EJ-299-33”. In: *Nuclear Instruments and Methods in Physics Research Section A: Accelerators, Spectrometers, Detectors and Associated Equipment* 735 (Jan. 2014), pp. 202–206. ISSN: 01689002. DOI: 10.1016/j.nima.2013.09.031. URL: <http://www.sciencedirect.com/science/article/pii/S0168900213012655>.
- [39] M. M. Bourne et al. “Scalability of Stilbene for Use in Nuclear Nonproliferation Applications”. In: *Institute of Nuclear Materials Management Annual Meeting Proceedings*. Indian Wells, CA, 2015.
- [40] *Mercury*. [Online] Available: <http://www.ccdc.cam.ac.uk/solutions/csd-system/components/mercury/> [2016, July 12]. Crystal Structure Visualisation, Exploration and Analysis Made Easy.
- [41] Natalia Zaitseva et al. “Pulse shape discrimination in impure and mixed single-crystal organic scintillators”. In: *IEEE Transactions on Nuclear Science* 58.6 PART 2 (2011), pp. 3411–3420. ISSN: 00189499. DOI: 10.1109/TNS.2011.2171363.